CONTINUOUS PRODUCTION OF SUPPORTED AND SHAPED METAL NANOCATALYSTS USING CONVEYOR TRANSPORT SYSTEM

BY

KAI-CHIEH TSAO

DISSERTATION

Submitted in partial fulfillment of the requirements
for the degree of Doctor of Philosophy in Chemical Engineering
in the Graduate College of the
University of Illinois at Urbana-Champaign, 2017

Urbana, Illinois

Doctoral Committee:

Professor Hong Yang, Chair
Professor Edmund G. Seebauer
Assistant Professor Damien S. Guironnet
Professor Yuanhui Zhang

Abstract

One of the major challenges in nanotechnology is to generate nanoparticles with controlled size, shape and composition and at the same time meet the commercial standards of mass manufacturing. The conventional colloidal synthetic approach, though has the ability to produce well-defined nanocrystals, often needs careful tuning of the reaction parameters to result in site-selective monomer attachment. Unfortunately, these methods cannot be easily scaled up by simply increasing the reaction volume, which inevitably bring about undesired perturbation in the system and thus cause nonuniformity in final products.

In this dissertation, conveyor transport system was developed as a new technique to produce continuously a family of supported and shaped metal nanocatalysts in a single-step process. With carbon monoxide (CO) as a major species to mediate the surface structures of metals, highly uniform cubic Pt/C with narrow size distribution could be synthesized in a continuous fashion; shaped carbon-supported Pt-M (M=Ni, Co, Fe) alloys were also generated using the same technique, demonstrating the capability of this system for generating bimetallic or potentially ternary alloys with controlled size and shape. This system was further applied to core-shell nanoparticles, and the morphology and composition of the cores as well as the shell thickness could be finely tailored to further enhance the activity and stabiltiy of the as-made electrocatalysts towards oxygen reduction reaction.

In the near future, we will focus on the continuous production of different structured noble/non-noble metal nanomaterials as well as the coupling of this system to annealing process and/or MEA manufacturing stage, movin towards production of the industrial application of these classes catalysts.

Acknowledgments

First of all, I would like to thank my research advisor, Professor Hong Yang, for his wholehearted support and patient guidance during my Ph.D. study. I remember during the first half of my PhD career, I was still exploring my interest in different research areas and didn't really focus on in-depth investigation in any one of them. But Prof. Yang never gave up on me, instead, he helped me go through all these obstacles, believing one day I would find something I was really passionate about and willing to dedicate my time into. Prof. Yang is not only my academic adviser, but also given me the warmth of a family with his considering attention to my physical and mental well-being, as well as ensuring my success in the future. Without his help, I will not be able to come to this stage. All I can express to him is my deepest gratitude.

I would like to thank my committee members, Prof. Edmund Seebauer, Prof. Damien S. Guironnet, and Prof. Yuanhui Zhang, for their dedicated service, great suggestions, and generosity with their precious time.

I spent a wonderful time in Prof. Yang's group with a team of excellent, intelligent, passionate people. I would like to thank my lab mates, Dr. Jianbo Wu, Dr. Xi Yin, Dr. Jaemin Kim, Dr. Na Zhang, Dr. Yung-Tin Pan, Steven Warren, Yuqi Yan, Thao Ngo, Pei-Chieh Shih, Dr. Yao Qin, Dr. Qiang Wang, Dr. Shaohua Fang, Dr. Baoliang Lyu, Dr. Wei Zhou, Dr. Tao Yang, Talha Al-Zoubi, Andrew Kuhn, and Xiaofei Lu, for their great help and friendship.

I am grateful to our staff at the School of Chemical Sciences and the Materials Research Laboratory for their assistance during my PhD research. Furthermore, I want to thank Mr. Tom Wilson, Mr. Mike Harland, and Dr. Mike Thompson for their constructive suggestions in the design of the continuously-operated conveyor transport system.

I also want to thank the wonderful people I met at UIUC, especially the members in Champaign Grilled Chicken Club—Yung-Tin Pan, Pei-Chieh Shih, Hua-Wei Ko, Cheng-Min Yang, Yi-Zong Ou, Kuo-Kang Hung, Johhny, Jon, David, Tony, and William. I really enjoyed the time we hang out together, and you guys make my life in UIUC much more colorful. Besides, I also want to thank my friends, Bo-Yu Jang, Ming Li, Yoshi Hsu, Alex Chen, and Allen Wang. No matter where we are and no matter where we go, our friendship never fades. Whenever we meet, we have endless things to talk about and share with each other. They also give me tremendous help when I need it most. They are the best examples of how friendship becomes stronger as one grows older.

Finally, I would like to express my heartfelt gratitude to my parents for their unconditional love and support in my life. When I encounter setback and adversity, they are always willing to listen to me carefully and chat with me for a long time to relieve my stress. I wouldn't have made it this far without their warm hearted encouragements.

Table of Contents

Chapter 1: Introduction to Continuous and Scalable Production of Well-Defined Metal Nanocatalysts 1

Chapter 2: Design of Conveyor Transport System 12

Chapter 3: Synthesis of Supported and Shaped Monometallic Nanocatalysts Using Conveyor Transport System 31

Chapter 4: Synthesis of Supported and Shaped Bimetallic Alloy Nanocatalysts Using Conveyor Transport System 60

Chapter 5: Synthesis of Supported and Shaped Bimetallic Core-Sell Nanocatalysts Using Conveyor Transport System 93

Chapter 6: Supported and Shaped Nanocatalysts as Electrode Material for Enhanced Electrocatalytic Performance 123

Chapter 7: Conclusion and Future Work 135

Appendix: Measurement of Particle Size 138

Chapter 1:

Introduction to Continuous and Scalable Production of Well-Defined Metal Nanocatalysts

1.1 Introduction

Nanotechnology has expanded into many areas of science and engineering in the last few decades due to its large potentials. Recently the synthesis of nanocrystals with well-defined shape has attracted considerable attention because of the improved activity and selectivity towards the targeted reaction. The commonly adopted synthesis routes include colloidal synthesis, electrochemical method and hydrothermal method.

Colloidal synthesis is one of the most common methods for preparing metallic nanocrystals with high level control over size, shape and composition. In this approach, surfactants are introduced in the flask to stabilize the colloidal suspension, and these long-chain ligands can adsorb preferentially onto specific metal surfaces, leading to different growth rates along various crystallographic directions. Eventually, the plane with the slowest growth rate becomes the dominating surface for the final particles (**Figure 1.1a**).[1-4]

These ligands, however, do not have high enough selectivity in surface binding and cannot be removed easily from nanocrystal surfaces either. Strong van der Waals interaction results in

the formation of close-packed organic shells, which prevent the reactants from accessing the active sites. Recently inorganic gas adsorbates were found capable of not only tailoring the nanostructures but also having reduced detrimental impact on electrocatalysis.[5] CO gas has become one of the excellent candidates for nanoparticle synthesis since it acts as both a reducing agent and facet-directing agent for Pt and other metals.[6-16]

CO gas generated by formic acid dehydration was first used to prepare Pt nanocubes, among others.[14] CO gas was then used directly to generate uniform cubic Pt nanocrystals, and IR spectra show the existence of CO on metal surfaces.[10] Based on this concept, gas-reducing-agent-in-liquid-solution (GRAILS) method was developed to successfully prepare a range of cubic and octahedral Pt-based nanocrystals with defined facets and specific compositions.[8] GRAILS approach can also be used to synthesize Pt and Pt-M (M = Au, Ni, Pd) icosahedra as well as complex heterostructures of Pt-Ni@Pt-Pd and Pt-Co@Pt-Pd core-shell nanoparticles.[6-7, 15]

In addition to traditional colloidal method, electrochemical deposition and replacement are used to synthesize shape-specific nanoparticles. Under potential deposition (UPD) and galvanic replacement are the two common methods (**Figure 1.1b**).

Under potential deposition (UPD) refers to the electrodeposition of a metal monolayer onto another metal substrate at a potential lower than the equilibrium reduction potential of the

depositing metal. This approach allows for precise control of the surface down to single atomic layer coverage, because the subsequent deposition is energetically unfavorable.[17-19]

For ORR catalysts, the monolayer shell is typically made of Pt atom. Sometimes UPD cannot be applied to deposit Pt monolayer on certain metals directly due to the mismatch of their redox potentials. In this case, a sacrificial metal layer, such as Cu, is formed first, followed by an irreversible redox reaction, known as galvanic replacement, between a pre-deposited metal and Pt ions. The metal is oxidized by Pt cations and dissolves, while Pt metal is formed and deposits onto the substrate.[20]

The hydrothermal method, or solvothermal method, is another approach for generating monodispersed catalyst particles with controlled size and shape. The reaction is carried out in an autoclave, where a precursor solution is filled in a vessel with PTFE-liner. (**Figure 1.1c**).

N,N-dimethylformamide (DMF) has been used as a solvent and reductant to produce shaped Pt and Pt alloy nanocrystals that show high ORR activity.[21] A surfactant-free hydrothermal method is further developed to synthesize shape- and size-controlled octahedral Pt−Ni nanoparticles with further improved ORR performance.[13, 22-25] Hydrothermal method is also used to generate a family of shaped Pt-M (M=Ni, Co, Fe) nanocrystals with ultrathin Pt-enriched shells, exhibiting excellent activity and durability in long-term ORR tests.[26]

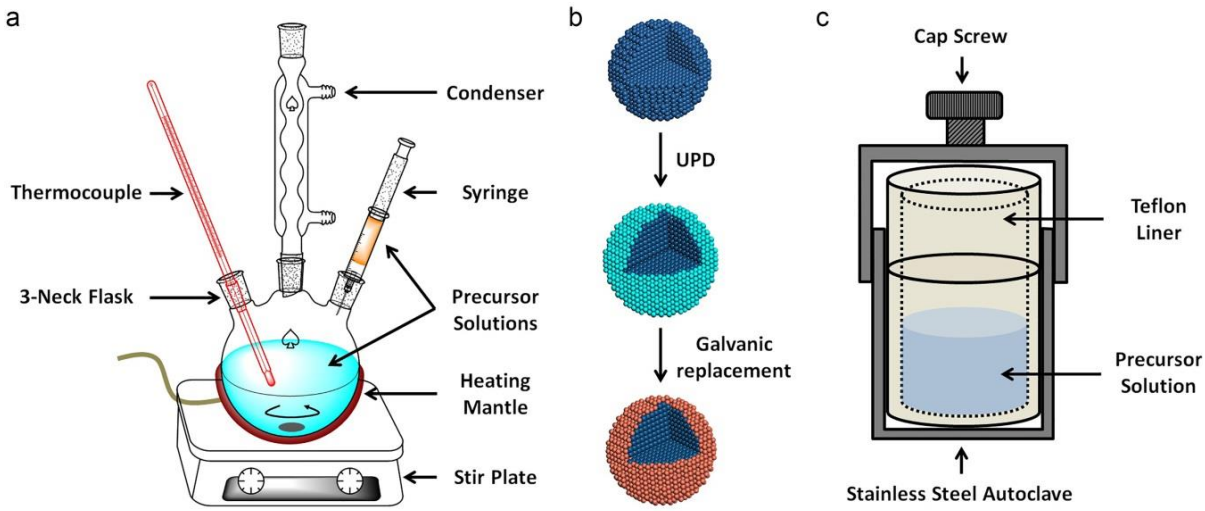

Figure 1.1 Major techniques for the synthesis of shape-controlled catalysts: (a) colloidal, (b) electrochemical and (c) hydrothermal methods.

These approaches, however, cannot be easily scaled up by simply increasing the reaction volume due to undesired perturbation in the system, leading to non-uniformity in the final nanostructures. Thus, the generation of well-defined faceted nanocrystals at commercial standards of mass manufacturing remains a big challenge.

1.2 Major Challenges towards Industrial Applications and Potential Solutions

Spray drying method has been widely applied in industry to generate unsupported and supported nano- or micron-sized materials because of its simple operation, low cost and high production rate characteristics.[27-29] Jang et al. further developed aerosol assisted co-assembly (AACA) route to synthesize titania- and graphene-supported Pt catalyst in a single-step process.[30-31] Although these techniques generate metal nanoparticles with good dispersion on the support surface, they fail to produce crystalline nanoparticles with well-controlled morphology, leading to low catalytic activities and performances.

A microfluidic reactor is a common device used to increase the production yield of high-quality crystalline nanomaterials. Ismagilov's group first developed the droplet-based microfluidic reactors wherein the chaotic advection can help mix the reagents in the droplets to enhance the homogeneity.[32-33] Xia and his co-workers further showed that highly uniform shaped nanocrystals can be formed after slight modifications.[34-37] This approach, on the other hand, requires tedious post-treatment to remove large amounts of surfactant and solvent, followed by loaded onto the support before being used as the catalyst.

To simplify the conventional two-step preparation methods, researchers are seeking a surfactant-free one-pot approach that can generate supported nanocatalysts with defined

morphology in a more efficient way. In addition to the synthesis of Pt nanocubes and nanoflowers deposited on reduced graphene oxide,[38-40] carbon-supported octahedral Pt3Ni nanocrystals and transition metal-doped ones can also be obtained in the absence of any bulky surface ligand. This technique leads to enhanced electrocatalytic activities in comparison to commercial catalysts owing to defined structure and cleaner surfaces.[41-42] Nonetheless, the aforementioned strategies are performed on a batch basis and will inevitably suffer from batch-to-batch variation; furthermore, the required reaction time in this process is much longer than that in traditional wet chemistry, showing sluggish kinetics. To date, there is no follow-up works demonstrating that these approaches can truly be scaled up for mass manufacturing.

1.3 Aim and Overview of Thesis

To bridge the gap between laboratory work and industrial application, developing a new protocol for continuous production of supported and shaped nanocrystals is an important task and the motivation of my thesis. In this thesis, I will first discuss the set-up and concept of the conveyor transport system, and how we can use this new approach to generate vast majority of morphologically pure nanocrystals dispersed on carbon black support in one step. I will then explore the possibility of utilizing this system to synthesize a series of crystalline nanoparticles that cannot be easily obtained in traditional solution-phase method. Finally, I will carry out several structure-sensitive reactions over as-prepared catalysts and demonstrate that this protocol can truly be commercialized for practical applications. The ultimate goal of this work is to realize the industrial potentials of the existing experimental work in colloidal synthesis.

1.4 References

1. You, H. J.; Yang, S. C.; Ding, B. J.; Yang, H. *Chem. Soc. Rev.* **2013**, *42*, 2880-2904.

2. Gu, J.; Zhang, Y. W.; Tao, F. *Chem. Soc. Rev.* **2012**, *41*, 8050-8065.

3. Peng, Z. M.; Yang, H. *Nano Today* **2009**, *4*, 143-164.

4. Tao, A. R.; Habas, S.; Yang, P. D. *Small* **2008**, *4*, 310-325.

5. Chen, M.; Wu, B. H.; Yang, J.; Zheng, N. F. *Adv. Mater.* **2012**, *24*, 862-879.

6. Wu, J. B.; Shi, M.; Yin, X.; Yang, H. *ChemSusChem* **2013**, *6*, 1888-1892.

7. Wu, J. B.; Qi, L.; You, H. J.; Gross, A.; Li, J.; Yang, H. *J. Am. Chem. Soc.* **2012**, *134*, 11880-11883.

8. Wu, J. B.; Gross, A.; Yang, H. *Nano Lett.* **2011**, *11*, 798-802.

9. Huang, X. Q.; Tang, S. H.; Mu, X. L.; Dai, Y.; Chen, G. X.; Zhou, Z. Y.; Ruan, F. X.; Yang, Z. L.; Zheng, N. F. *Nat. Nanotechnol.* **2011**, *6*, 28-32.

10. Wu, B. H.; Zheng, N. F.; Fu, G. *Chem. Commun.* **2011**, *47*, 1039-1041.

11. Yu, Y.; Luo, Z. T.; Yu, Y.; Lee, J. Y.; Xie, J. P. *ACS Nano* **2012**, *6*, 7920-7927.

12. Chen, G. X.; Tan, Y. M.; Wu, B. H.; Fu, G.; Zheng, N. F. *Chem. Commun.* **2012**, *48*, 2758-2760.

13. Dai, Y.; Mu, X. L.; Tan, Y. M.; Lin, K. Q.; Yang, Z. L.; Zheng, N. F.; Fu, G. *J. Am. Chem. Soc.* **2012**, *134*, 7073-7080.

14. Kang, Y. J.; Ye, X. C.; Murray, C. B. *Angew. Chem.-Int. Edit.* **2010**, *49*, 6156-6159.

15. Zhou, W.; Wu, J. B.; Yang, H. *Nano Lett.* **2013**, *13*, 2870-2874.

16. Cui, C. H.; Gan, L.; Neumann, M.; Heggen, M.; Cuenya, B. R.; Strasser, P. *J. Am. Chem. Soc.* **2014**, *136*, 4813-4816.

17. Herrero, E.; Buller, L. J.; Abruna, H. D. *Chem. Rev.* **2001**, *101*, 1897-1930.

18. Kolb, D. M.; Przasnyski, M.; Gerischer, H. *J. Electroanal. Chem.* **1974**, *54*, 25-38.

19. Leiva, E. *Electrochim. Acta* **1996**, *41*, 2185-2206.

20. Zhang, J.; Lima, F. H. B.; Shao, M. H.; Sasaki, K.; Wang, J. X.; Hanson, J.; Adzic, R. R. *J. Phys. Chem. B* **2005**, *109*, 22701-22704.

21. Carpenter, M. K.; Moylan, T. E.; Kukreja, R. S.; Atwan, M. H.; Tessema, M. M. *J. Am. Chem. Soc.* **2012**, *134*, 8535-8542.

22. Cui, C. H.; Gan, L.; Heggen, M.; Rudi, S.; Strasser, P. *Nat. Mater.* **2013**, *12*, 765-771.

23. Cui, C. H.; Gan, L.; Li, H. H.; Yu, S. H.; Heggen, M.; Strasser, P. *Nano Lett.* **2012**, *12*, 5885-5889.

24. Gan, L.; Cui, C. H.; Heggen, M.; Dionigi, F.; Rudi, S.; Strasser, P. *Science* **2014**, *346*, 1502-1506.

25. Cui, C.; Ahmadi, M.; Behafarid, F.; Gan, L.; Neumann, M.; Heggen, M.; Cuenya, B. R.; Strasser, P. *Faraday Discuss.* **2013**, *162*, 91-112.

26. Gu, J.; Lan, G. X.; Jiang, Y. Y.; Xu, Y. S.; Zhu, W.; Jin, C. H.; Zhang, Y. W. *Nano Res.* **2015**, *8*, 1480-1496.

27. Okuyama, K.; Lenggoro, I. W. *Chem. Eng. Prog.* **2003**, *58*, 537-547.

28. Iskandar, F.; Gradon, L.; Okuyama, K. *J. Colloid Interface Sci.* **2003**, *265*, 296-303.

29. Nandiyanto, A. B. D.; Okuyama, K. *Adv. Powder Technol.* **2011**, *22*, 1-19.

30. Jang, H. D.; Kim, S. K.; Chang, H.; Choi, J.-W.; Luo, J.; Huang, J. *Aerosol. Sci. Tech.* **2013**, *47*, 93-98.

31. Jang, H. D.; Chang, H.; Cho, K.; Kim, F.; Sohn, K.; Huang, J. *Aerosol. Sci. Tech.* **2010**, *44*, 1140-1145.

32. Song, H.; Tice, J. D.; Ismagilov, R. F. *Angew. Chem. Int. Ed.* **2003**, *42*, 768-772.

33. Shestopalov, I.; Tice, J. D.; Ismagilov, R. F. *Lab Chip* **2004**, *4*, 316-321.

34. Zhang, L.; Wang, Y.; Tong, L. M.; Xia, Y. N. *Langmuir* **2013**, *29*, 15719-15725.

35. Zhang, L.; Wang, Y.; Tong, L.; Xia, Y. *Nano Lett.* **2014**, *14*, 4189-4194.

36. Kim, Y. H.; Zhang, L.; Yu, T.; Jin, M. S.; Qin, D.; Xia, Y. N. *Small* **2013**, *9*, 3462-3467.

37. Zhang, L.; Xia, Y. N. *Adv. Mater.* **2014**, *26*, 2600-2606.

38. Li, F. M.; Gao, X. Q.; Xue, Q.; Li, S. N.; Chen, Y.; Lee, J. M. *Nanotechnology* **2015**, *26*.

39. Yu, X.; Wang, H.; Guo, L.; Wang, L. *Chem. Asian J.* **2014**, *9*, 3221-3227.

40. Xia, B. Y.; Wu, H. B.; Yan, Y.; Wang, H. B.; Wang, X. *Small* **2014**, *10*, 2336-2339.

41. Huang, X.; Zhao, Z.; Cao, L.; Chen, Y.; Zhu, E.; Lin, Z.; Li, M.; Yan, A.; Zettl, A.; Wang, Y. M.; Duan, X.; Mueller, T.; Huang, Y. *Science* **2015**, *348*, 1230-1234.

42. Huang, X.; Zhao, Z.; Chen, Y.; Zhu, E.; Li, M.; Duan, X.; Huang, Y. *Energ. Environ. Sci.* **2014**, *7*, 2957-2962.

Chapter 2:

Design of Conveyor Transport System[1]

2.1 Concept and the Set-Up of the System

For conveyor ovens, all the ingredients are put on one end, after being transported to the oven for cooking, a meal is prepared on the other end. Inspired by this design, A "conveyor transport system" can be designed such to provide the conditions for nanoparticle synthesis. Due to its previously-mentioned shape-directing capabilities, CO gas flows continuously through the heated reactor to mediate particle growth. The precursors were deposited on the belt and transferred through the CO-filled reactor. Supported and shaped nanocatalsyts were continuously generated on the other side of the reactor (**Figure 2.1**).

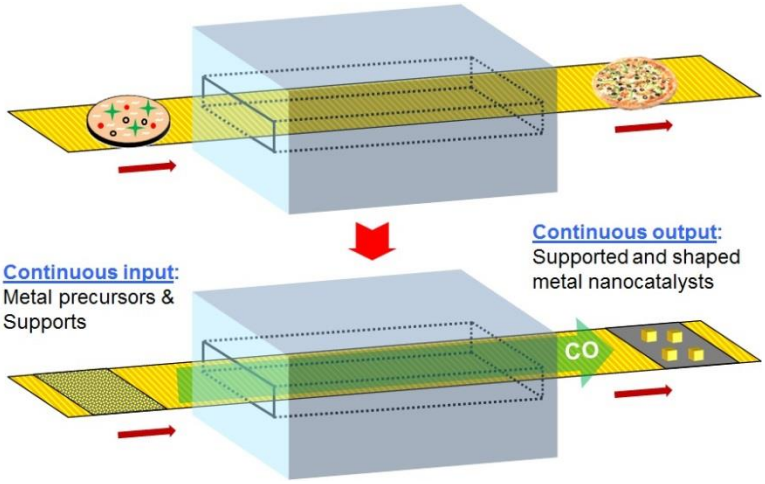

Figure 2.1 Schematic illustration of continuously-operated system.

[1] Modified with permission, from Tsao, K.-C.; Yang, H. *Small* **2016**, *12*, 4808-4814.

The conveyor transport system, **Figure 2.2**, consists of five parts: air brush, hot plate, reactor, conveyor belt and speed controller (**Figure 2.3**). The airbrush is commercially available (BD-130B, Image) and has a nozzle diameter of 300 μm and a spray patter of solid cone. The hot plate is composed of an aluminum plate and two aluminum housed wire-wound resistors (UAL-25, 750 Ohms, 25W, Digi-Key), and the potential is provided by a Variac transformer to adjust the temperature of the hot plate. A washer thermocouple (WT, type K, Digi-Key) is attached to the hot plate to monitor the temperature; its dependence on potential is shown in **Figure 2.4a**. A quartz tube wrapped with fiberglass heater tape (Standard, OMEGA Engineering) is used as the reactor. There is a thin slit on each Teflon stopper, a 1/8" diameter hole was drilled on one Teflon stopper for CO purging. A Variac transformer is again used to control the temperature of the heater tape; their relationship can be found on **Figure 2.4b**. Teflon- or silicone-coated fiberglass fabric is used as the conveyor belt, depending on the precursor solution. Hydrophobic solvents such as chloroform use Teflon material; whereas hydrophilic solvents such as ethanol use silicone material. A resistance substitution box (RS-500, Elenco Electronics) is used to control the rotation speed of the motor (collected from abandoned equipment). A speed reducer consists of two gears (1 to 36 in their diameters) is attached to the motor to further slow down its speed. The whole set is then combined with a plastic roller in order move the conveyor belt.

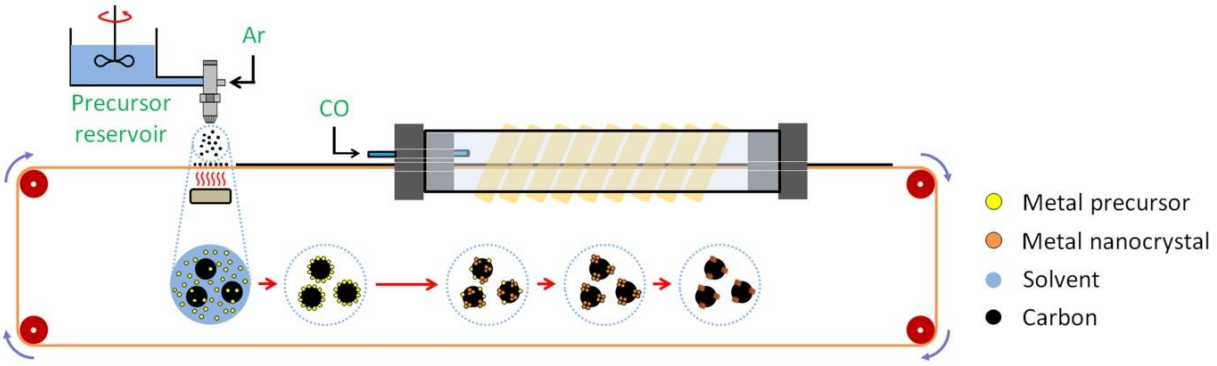

Figure 2.2 Schematic illustration of the reactor and stages of the synthesis of carbon-supported shape and composition controlled metal catalysts.

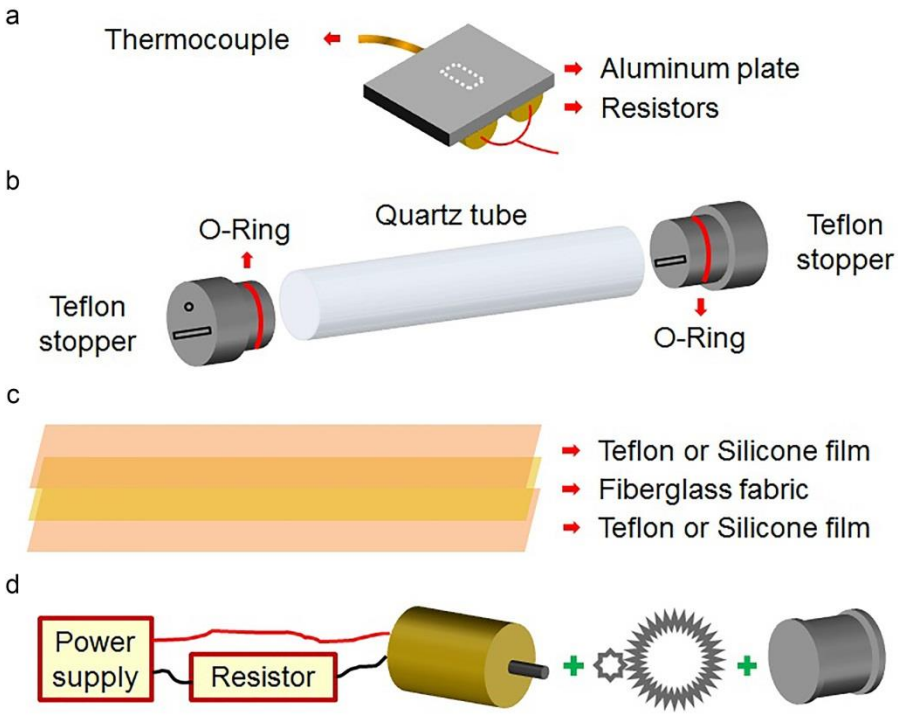

Figure 2.3 Components of conveyor transport system: (a) hot plate, (b) reactor, (c) conveyor belt and (d) speed controller.

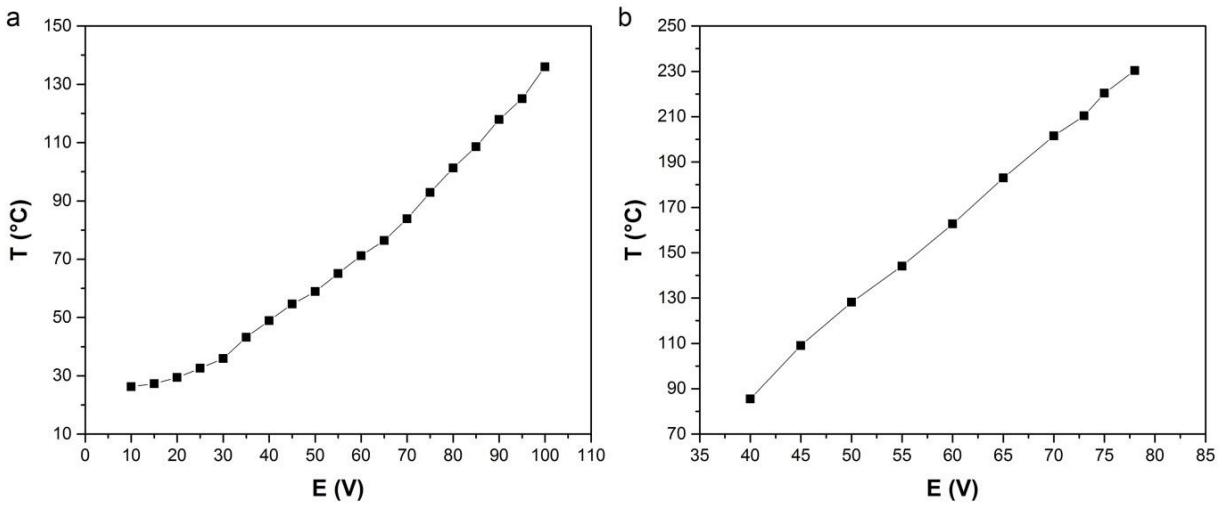

Figure 2.4 Relationship between the potential applied by the transformer and (a) the temperature of hot plate; (b) the wall temperature of reactor.

During the deposition, precursor solution was atomized into small droplets through airbrush with Ar as the carrier gas. The atomized droplets were spray deposited onto the belt. Temperature for depositing the precursors was above the solvent boiling temperature but below the thermal decomposition of the precursors. The distance between airbrush and the belt was optimized so that the solvent evaporated quickly. This optimization was to eliminate flooding of precursors on the belt. The belt deposited with the precursor was transported to the reactor and underwent the thermal decomposition reaction to form metal nanoparticles on support in the reactor unit under hot CO atmosphere. The products were collected by scratching with spatula or rinsing catalyst-loaded belt with either chloroform or ethanol.

2.2 Optimization of Operation Parameters in Deposition Stage

When precursor solution was sprayed onto the preheated conveyor belt, several operational parameters have an impact on the uniformity of precursor deposition and can further affect the final nanostructures (**Figure 2.5**). The purging rate of carrier gas, concentration of precursor solution, distance between airbrush and hot plate, and the temperature of hot plate all had an effect. Therefore, it is very important to optimize theses variables in order to achieve highest catalytic performance and desirable production yield.

In addition, the purging pattern for atomization process can also have an influence on the precursor deposition. Because of the hot plate's limited size and heating capabilities, "quiet time" is needed to ensure dryness of the deposit. Additionally, continuous spraying will cause serious flooding. Preliminary results showed that two seconds spraying followed by two seconds of quiet time can achieve satisfactory precursor deposition (**Figure 2.6**).

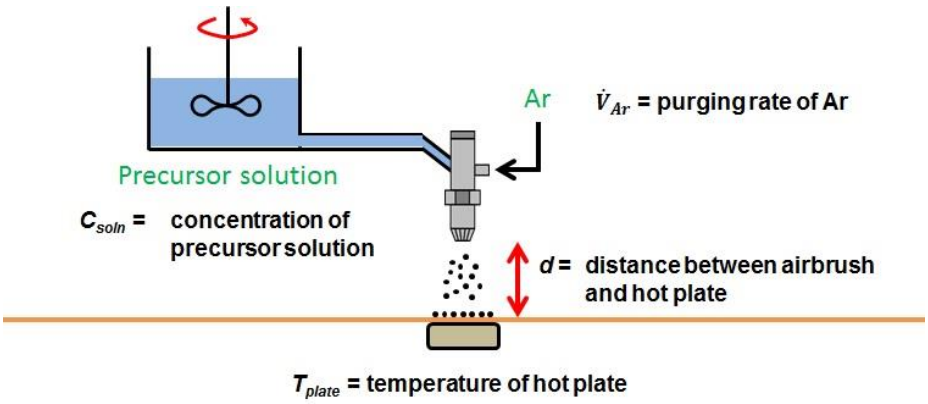

Figure 2.5 Control variables in deposition stage.

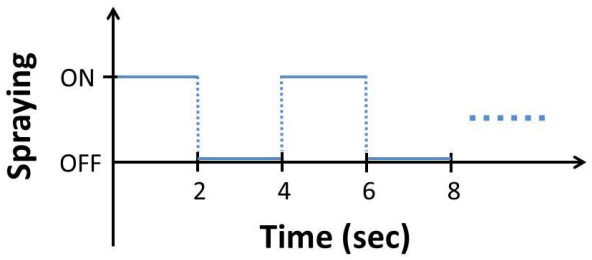

Figure 2.6 Purging pattern of airbrush adopted in the deposition stage.

To simplify the optimization process, the purging rate of Ar was set at 2 L min^{-1} and prepared a standard precursor solution that was well-mixed prior to loading. This solution contained 8 mg of platinum acetylacetonate ($Pt(acac)_2$, Strem Chemicals, 98%), 16 mg of carbon black (Vulcan XC-72, Cabot), 50 μL of oleylamine (OAm, Sigma-Aldrich, 70%) and 5 mL of chloroform (Fisher Chemical, >99%). The distance between airbrush and hot plate, d, and the temperature of hot plate, T_{plate}, was changed for each trial. A photo was taken for each precursor deposit to examine the uniformity of the deposition. After thermal deposition under hot carbon monoxide environment (CO, research grade, Airgas), the product was collected and weighed. A small amount of product was dispersed in chloroform for later transmission electron microscopy (TEM) characterization. The size distribution analysis of each sample was also carried out based on the corresponding TEM micrographs by using ImageJ software (Refer to the next chapter for more details about the formation of Pt nanocubes).

The images of deposited precursors based on different hot plate temperature and spray distance were summarized in **Figure 2.7**. At low T_{plate} and d, too much precursor solution reached the belt, evaporation of the solvent was poor, and serious flooding occurred (**Figure 2.7a and e**). Slightly increase T_{plate} and d can avoid severe wetness, though some ring patterns were observed, indicating a non-uniform precursor deposition (**Figure 2.7b, f, I, j, and m**). T_{plate} and d need to be increase to 140 °C and 10 cm, respectively, in order to achieve uniform depostion (**Figure 2.7c, d, g, h, k, l, n, o and p**). The color became darker with increasing T_{plate} and decreasing d, indicating larger amound of precusor were deposited under these conditions.

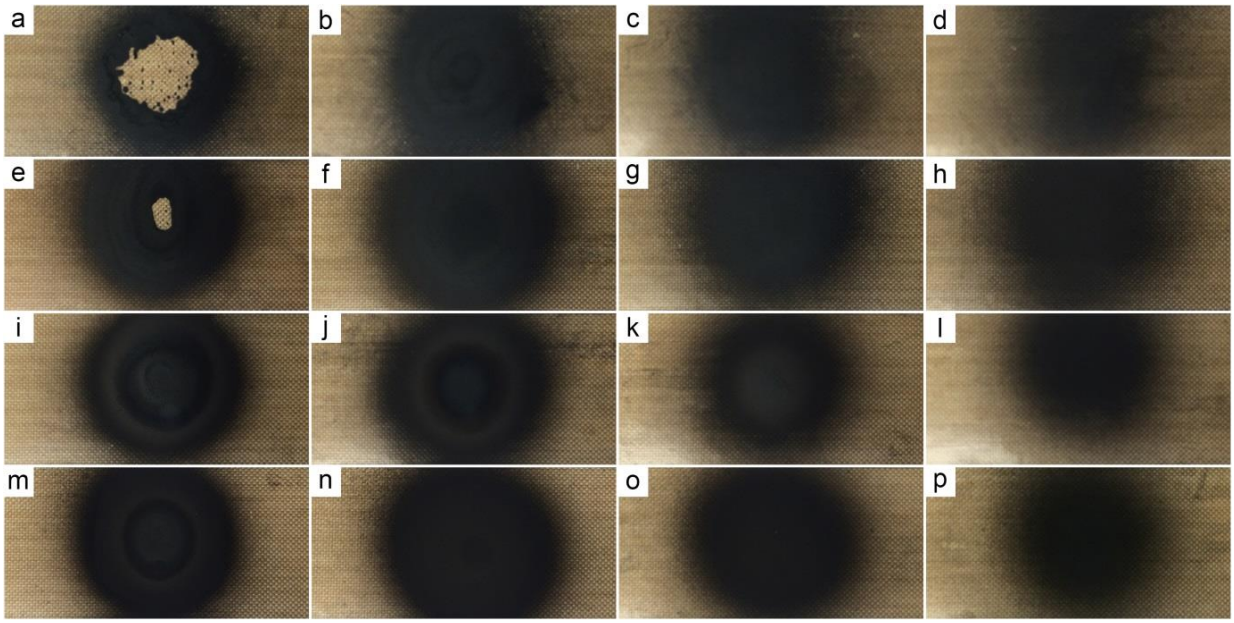

Figure 2.7 Images of deposited precursors on the belt. Operation parameters: T_{plate} = (a-d) 80 °C, (e-h) 100 °C, (i-l) 120 °C and (m-p) 140 °C; d = (a, e, i, m) 5 cm, (b, f, j, n) 7.5 cm, (c, g, k, o) 10 cm and (d, h, l, p) 12.5 cm.

The TEM micrographs and the size distribution of as-made Pt/C catalysts under these 16 conditions were also provided below (**Figure 2.8** to **Figure 2.11**). For better comparison, they were summarized into a single plot (**Figure 2.12**). Specifically, for Pt/C synthesized under $T_{plate} \geq 100$ °C and $d \geq 10$ cm, the particle size were within 3.3 nm and 3.5 nm with standard deviation of 0.5 nm. On the other hand, the least uniform sample has particle size of 5.2 ± 1.2 nm. If the solvent evaporated very fast when the precursor solution droplet reached the belt, $Pt(acac)_2$ would stick on and disperse evenly on the carbon support, leading to monodisperse Pt/C. However, if the evaporation rate was too slow, $Pt(acac)_2$ could move freely during the drying process and may end up on non-porous Teflon film, leading to much larger particle size and broader size distribution after reaction.

The collection efficiency was also calculated. When the distance, d, was large, precursors were sprayed in wide regions, thus the production yield decreased, because only a small portion of precursors could deposit onto the belt. Lower T_{plate} resulted in fewer precursors on the belt since serious flooding cause some of them flow out of the belt. When T_{plate} was too high, however, rapid evaporation would carry away a small amount of precursor out of the system and thus lower yield. Therefore, there existed an optimal temperature that can achieve highest production yield, in this case, 100 °C (**Figure 2.13**).

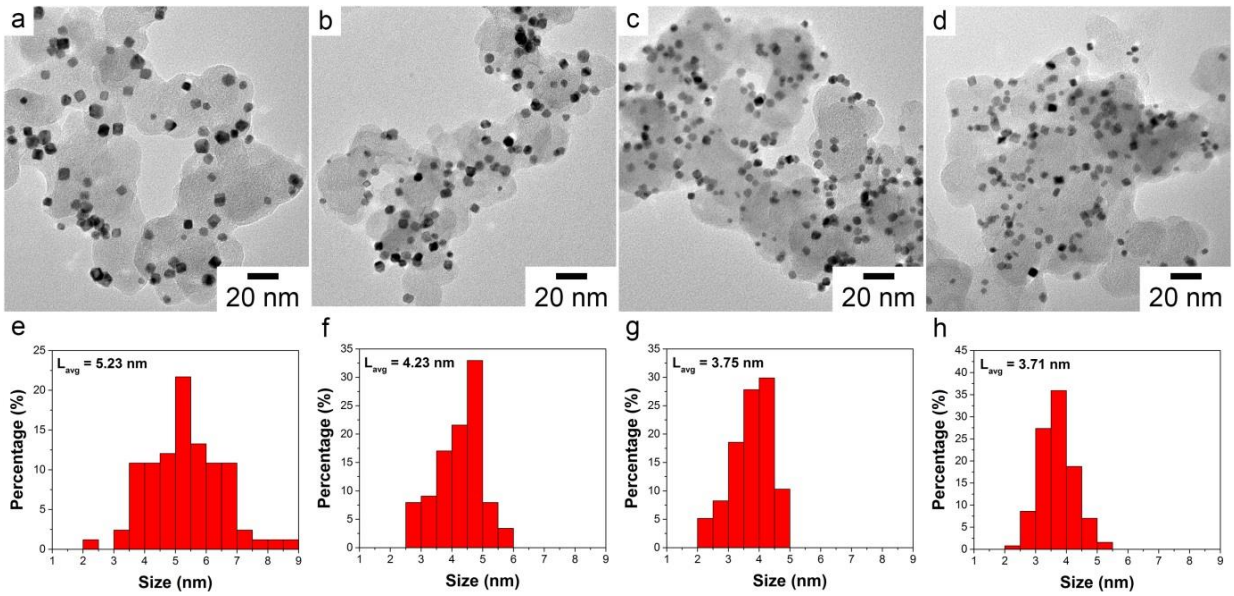

Figure 2.8 (a-d) TEM micrographs and (e-h) size distribution of as-made Pt/C. Operation parameters: T_{plate}= 80 °C; d = (a,e) 5 cm, (b,f) 7.5 cm, (c,g) 10 cm and (d,h) 12.5 cm.

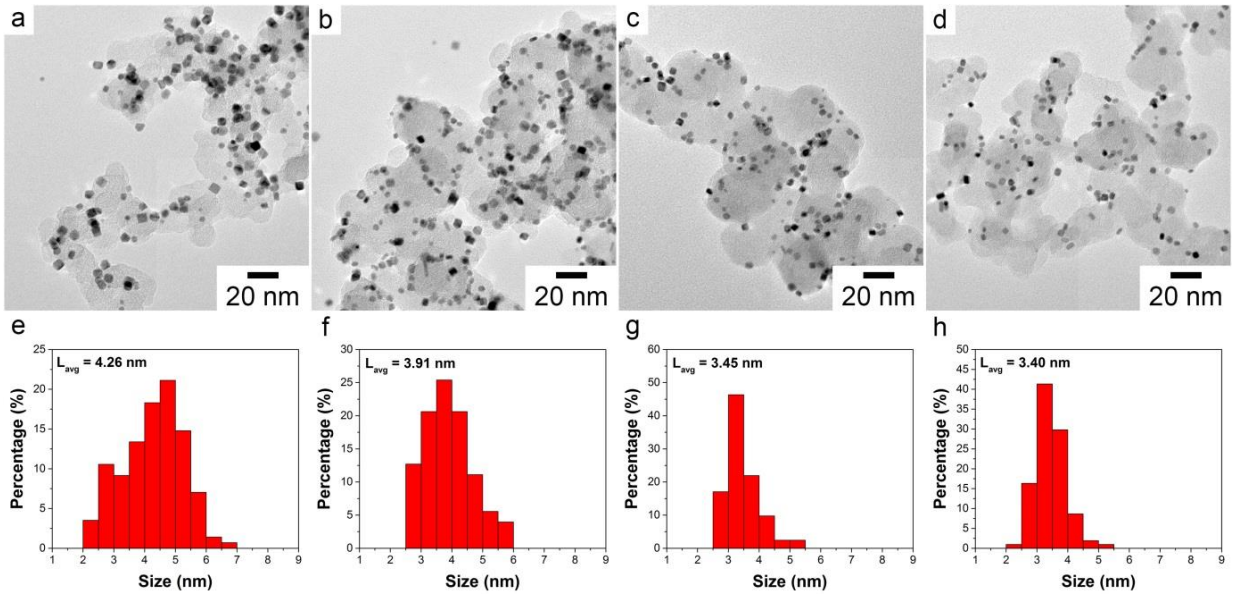

Figure 2.9 (a-d) TEM micrographs and (e-h) size distribution of as-made Pt/C. Operation parameters: T_{plate}= 100 °C; d = (a,e) 5 cm, (b,f) 7.5 cm, (c,g) 10 cm and (d,h) 12.5 cm.

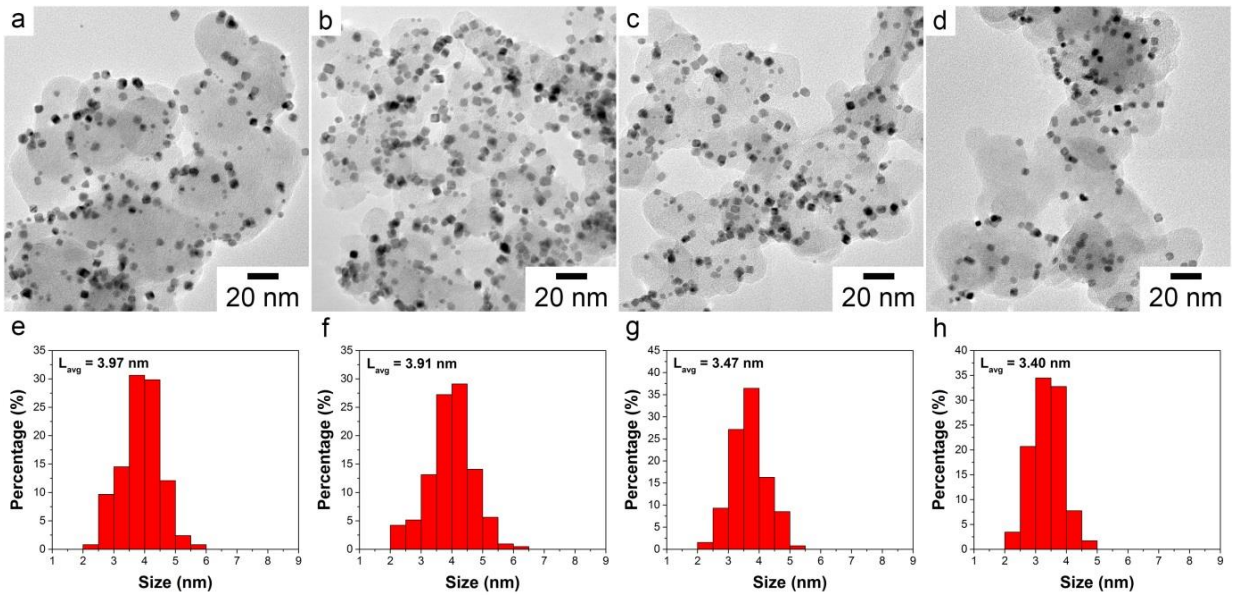

Figure 2.10 (a-d) TEM micrographs and (e-h) size distribution of as-made Pt/C. Operation parameters: T_{plate}= 120 °C; d = (a,e) 5 cm, (b,f) 7.5 cm, (c,g) 10 cm and (d,h) 12.5 cm.

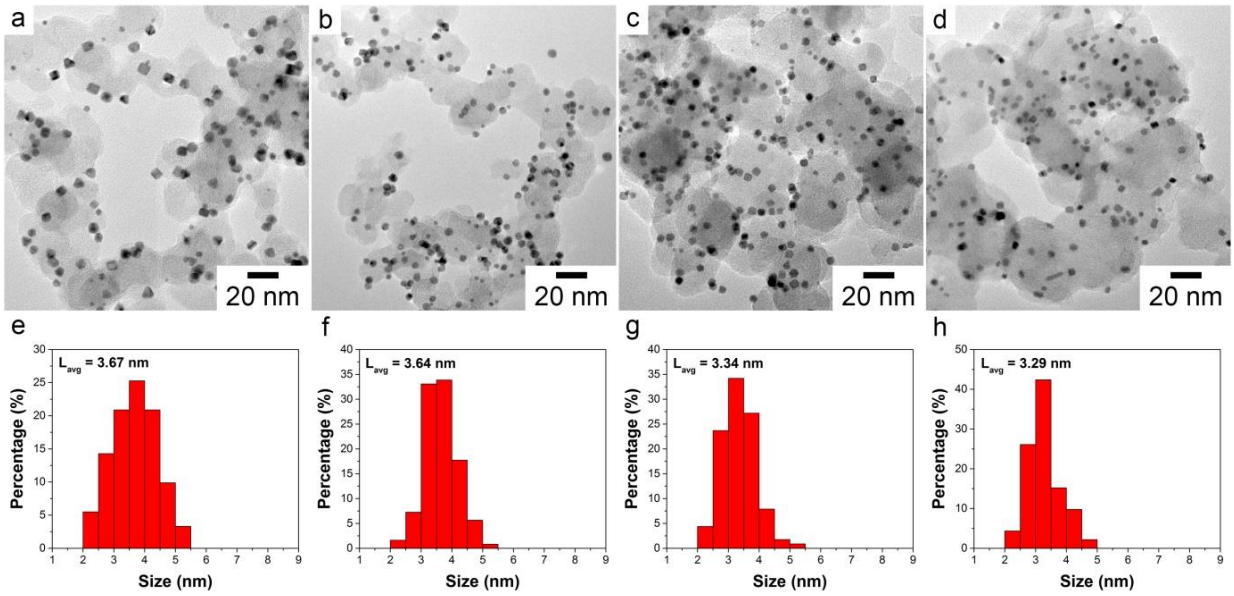

Figure 2.11 (a-d) TEM micrographs and (e-h) size distribution of as-made Pt/C. Operation parameters: T_{plate}= 140 °C; d = (a,e) 5 cm, (b,f) 7.5 cm, (c,g) 10 cm and (d,h) 12.5 cm.

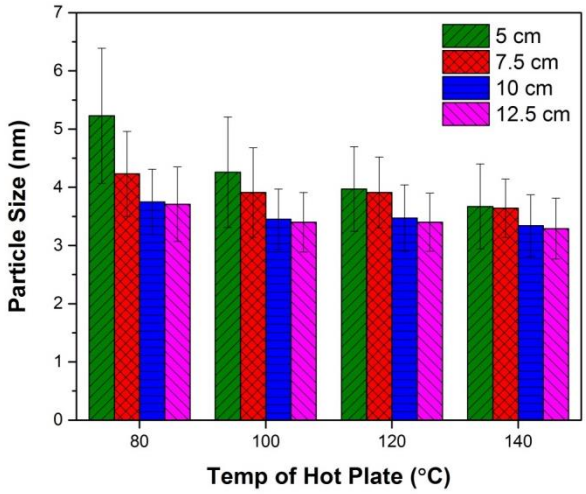

Figure 2.12 Summary of particle size of Pt/C synthesized under different conditions.

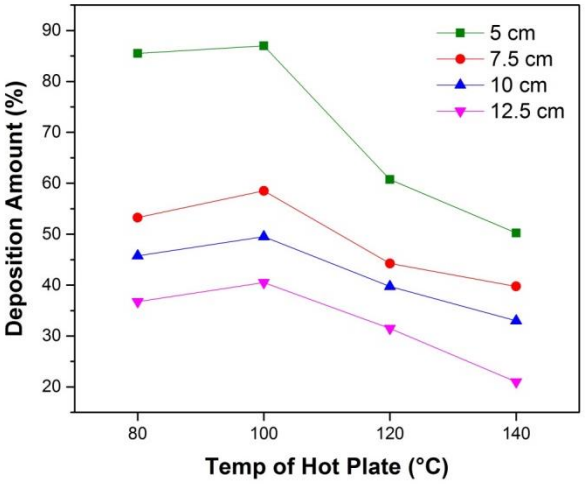

Figure 2.13 Summary of deposition amount of Pt/C synthesized under different conditions.

Though the collection efficiency decreases with incresing spray distance, this can be easily solved by increasing the width of conveyor belts. Since the production rate of catalyst is directly

related to the deposition rate of precursor, we can thus estimate the throughput of the conveyor transport system. When the Ar purging rate is set to 2 L min^{-1}, a 5 mL-precursor solution can be completely consumed in around 2 min. If we consider 100% of precursor conversion and collection efficiency for the generation of 20 wt% carbon-supported Pt nanocubes catalyst, the throguhput rate, *F*, is calculated as

$$F = \frac{total\ production\ amount}{total\ purging\ time} = \frac{16\ mg\ Carbon + 4\ mg\ Pt}{2\ min} = 10\ mg\ min^{-1} \qquad (1)$$

For conventional colloidal synthesis, it takes about 30 min to generate 10 mg of Pt metal, followed by overnight-stirring in order to obtain supported catalyst.[1-3] Therefore, we are able to generate supported and shaped catalysts in a more efficient way using the newly developed conveyor transport system when compared to colloidal synthetic route.

In the future, nozzle needs to be re-designed in order to further enhance the collection efficiency. For instance, by slightly reducing the nozzle size, both spray angle and droplet size can be decreased, thus avoiding precursor deposition on the hot plate region and facilitating the dryness of the precursor deposition, respectively.[4-6]

2.3 Heat Transfer Analysis inside the Reactor

The temperature profile inside the tubular reactor was examined by performing the overall energy balance. The flow in the tubular reactor was considered as an internal forced convection if the effect of the two stoppers at ends and the conveyor belt could be neglected once the reactor environment reached the steady state (**Figure 2.14**).

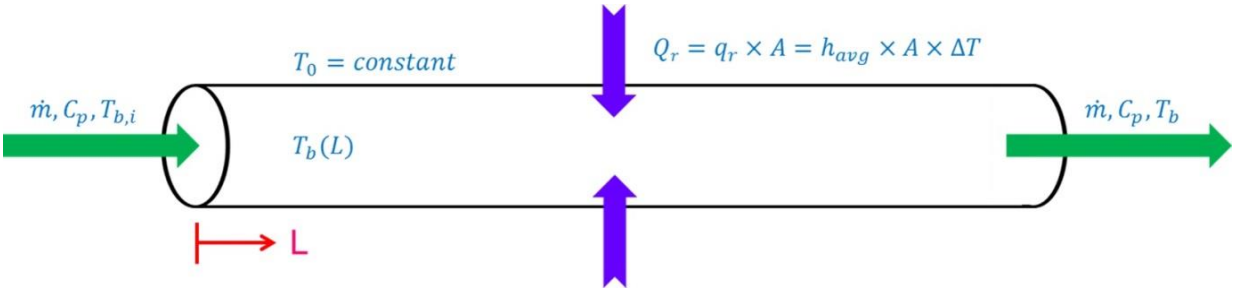

Figure 2.14 Internal forced convection in a tubular reactor.

When a gas entering at one end was heated and left at the other end, the temperature at a given position along the tubular reactor could be expressed as the following equation:

$$\rho \times \dot{V} \times C_p \times (T_b - T_{b,i}) = \beta \times h \times A \quad (2)$$

where A is the total external surface area of the tube wrapped with heating tape that provided heat to the reactor:

$$A = \pi \times D \times L \quad (3)$$

Plug Eq. (2) into Eq. (1) and rearrange it, we can get

$$\frac{T_b - T_{b,i}}{T_w - T_b} = \frac{\beta \times \pi \times D \times h \times L}{\rho \times \dot{V} \times C_p} \tag{4}$$

where T_b is the average temperature along the radial direction and the subscript i refers to the temperature at the beginning of heating zone; T_w is the wall temperature of the tube, which was set at 230 °C during the reaction; ρ, $\dot{V}$, and C_p are density, volumetric flow rate, and specific heat capacity of the purging gas, respectively; D and L are the inner diameter and length of the tubular reactor, respectively; β is defined as the turbulence factor which is equal to one for laminar flow and larger than one when the fluid becomes more turbulent; h is the heat transfer coefficient that can be expressed in terms of Nusselt number, Nu[7]

$$h = \frac{k \times Nu}{D} \tag{5}$$

where k is the thermal conductivity of the flowing fluid. Nusselt number has different expressions based on the flow pattern and is usually a function of Reynolds number, Re[7]

$$Re = \frac{\rho \times u \times D}{\mu} \tag{6}$$

where the average fluid velocity, u, can be expressed as

$$u = \frac{4\dot{V}}{\pi \times D^2} \tag{7}$$

The average fluid velocity and the corresponding Reynolds number based on different purging gas and volumetric flow rate are summarized in **Table 2.1**. In each case, Reynolds number was much smaller than 2100, implying flow should be laminar, and the effect of the purging gas on the flow pattern is almost negligible. In such case, the Nusselt number can be calculated based on the following equation[8]

$$Nu = 3.66 + \frac{0.065\, Pe\, \frac{D}{L}}{1 + 0.04\left(Pe\, \frac{D}{L}\right)^{2/3}} \tag{8}$$

where the Peclet number, Pe, is given by[7]

$$Pe = \frac{u \times D}{\alpha} \tag{9}$$

where α is the thermal diffusivity of the entering gas fluid.

Table 2.1 Volumetric flow rate, average flow rate, and Re of different fluids in the reactor.

Type of gas	$\dot{V}$ (mL min^{-1})	u m s^{-1}	Re (-)
CO	500	0.0079	23
CO	750	0.0118	35
CO	1000	0.0157	46
Ar	500	0.0079	26
Ar	750	0.0118	39
Ar	1000	0.0157	52

Figure 2.15 shows the measured (solid black squares) and calculated (solid and dashed lines) temperature profiles inside the tubular reactor at a CO volumetric flow rate of 500 mL min^{-1} with the wall temperature of 230 °C. The temperature of gas fluid increased rapidly and reached 180 °C at ≈ 3.5 cm after entering the heating zone and eventually reached 220 °C. The observed temperature profile shows a typical internal forced convection pattern. At the very beginning, the measured temperature values matched well to those for laminar flow and became higher than expected along the tube, suggesting the fluid inside is turbulent like. Such turbulent flow is preferred for better energy transfer across the flow at a given axial position than the laminar flow. This flow pattern was mainly the result of using stopper in the tubular reactor, which caused the back flow of the gas and made the flow pattern more chaotic (**Figure 2.16**). As a result, Nu number and heat transfer coefficient h should increase, thus β was introduced as a correction factor to account for the actual enhanced heat transfer.[8-9] The value of β changed from one (i.e., ideal laminar flow) to three along the heating zone. With this treatment, the experimental measurement matches well with the simulation data for the temperature profile inside the reactor, indicating the gas flow became turbulent in the later part of the tubular reactor. Temperature reached the maximum in the middle section and began to decrease to about 200 °C at the end of the heating zone (**Figure 2.17**). This temperature profile was expected since no heat flux was provided after the heating zone and preferable for the process as it helped in gradually cooling

the product. Since β is only affected by the geometry and the flow pattern of the reactor, this model can be applied to the system with different wall temperature as long as the dimension of the quartz tube and the purging rate of CO gas are kept the same. This allows us to accurately predict the temperature profile inside the reactor without really measuring it, thus saving us a great deal of time and effort.

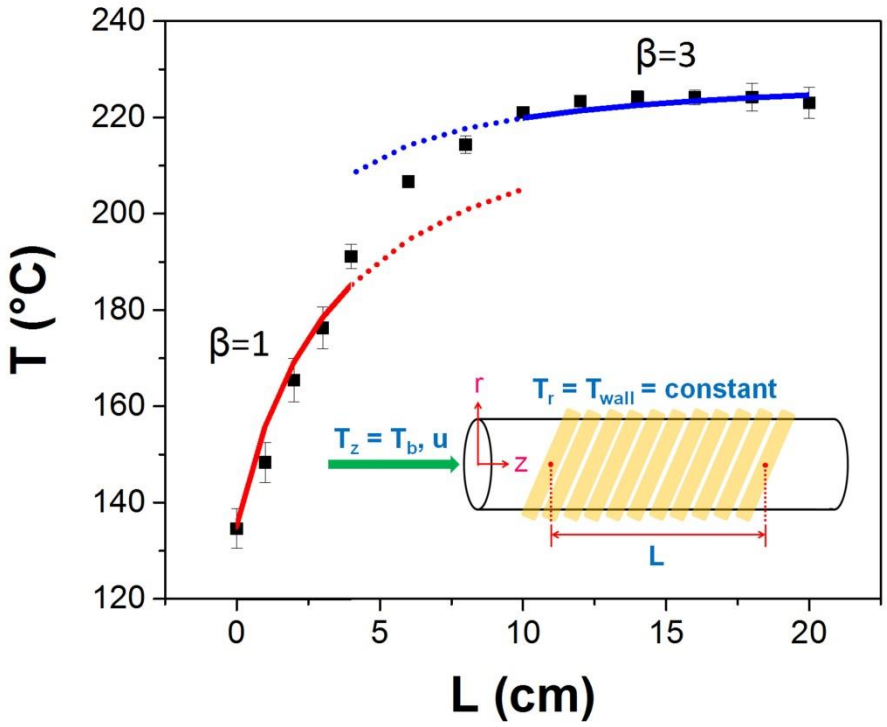

Figure 2.15 Temperature profile along the tubular direction of the reactor with T_w of 230 °C. Black squares refer to the measured values; while solid and dashed lines are based on calculated values based using Eq. (1).

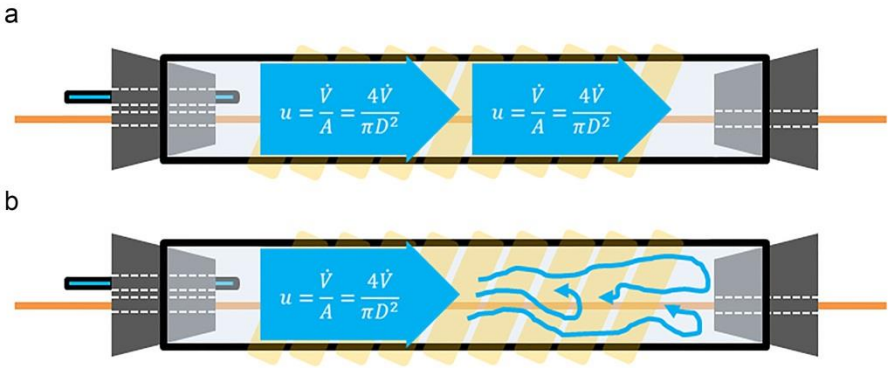

Figure 2.16 The flow pattern inside the tubular reactor when (a) neglect or (b) consider the presence of Teflon stopper at the end.

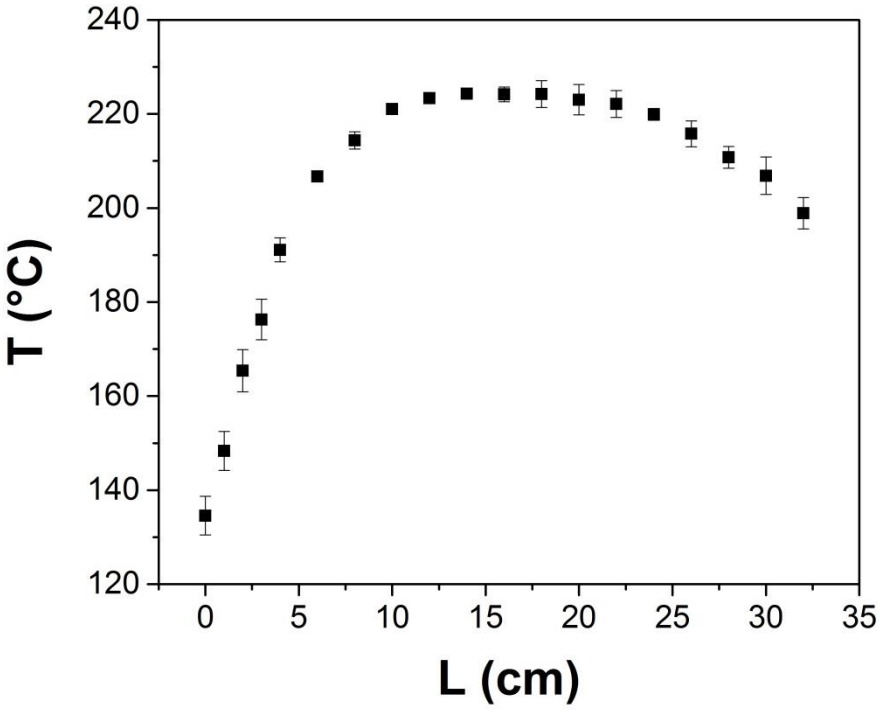

Figure 2.17 Temperature profile for the entire length of the tubular reactor, in which the wall temperature was controlled at 230 °C.

2.4 References

1. Peng, Z. M.; Yang, H. *Nano Today* **2009**, *4*, 143-164.

2. Gu, J.; Zhang, Y. W.; Tao, F. *Chem. Soc. Rev.* **2012**, *41*, 8050-8065.

3. You, H. J.; Yang, S. C.; Ding, B. J.; Yang, H. *Chem. Soc. Rev.* **2013**, *42*, 2880-2904.

4. Welander, P.; Vincent, T. L. *Chem. Eng. Prog.* **2001**, *97*, 75-79.

5. Pagcatipunan, C.; Schick, R. *Chem. Eng. Prog.* **2005**, *101*, 38-44.

6. Lipp, C. W. *Chem. Eng. Prog.* **2014**, *110*, 51-58.

7. Holman, J. P. *Heat Transfer* **1986**, New York: McGraw-Hill.

8. Edwards, D. K.; Denny, V. E.; Mills, A. F. *Transfer Processes* **1973**, New York: Hemisphere Publishing Co.

9. R. B. Bird; W. E. Stewart; E. N. Lightfoot *Transport Phenomena* **2006**, New York: John Wiley & Sons, Inc.

Chapter 3:

Synthesis of Supported and Shaped Monometallic Nanocatalysts Using Conveyor Transport System[2]

3.1 Introduction

In the previous chapter we discussed the optimization of operation parameters including spray distance and hot plate temperature to achieve uniform precursor deposition, high collection efficiency and narrow size distribution. We also applied heat transfer analysis on the reactor to obtain the temperature profile along the quartz tube. Here, we will further demonstrate the capability of this newly developed protocol for continuous production of highly uniform and precision-controlled carbon-supported monometallic nanocrystals.

Among them, Pt and Pd metals are of particular interest due to their wide application in different research fields, and they are also the two elements that can remain stable under highly corrosive conditions in fuel cells.[1-2] Therefore, we will focus on shape-selective Pt/C and Pd/C nanocatalysts in this chapter. A large body of literature has shown that cubic Pt nanocrystals can be formed under hot CO environment via wet chemistry or solid-state chemistry routes,[3-7] which can be attributed to the preferential adsorption of CO molecules on Pt(100) facets.[8] On the other

[2] Modified with permission, from Tsao, K.-C.; Yang, H. *Small* **2016**, *12,* 4808-4814.

hand, the formation of Pd nanosheet/nanoplate, with (111) surfaces as the basal planes, is favored under CO environment due to stronger binding of CO molecules on these faces.[9-11] Therefore, by utilizing CO as both reducing agent and shape-directing agent in the conveyor transport system, supported and shaped Pt and Pd nanocatalysts can be generated in a single step.

For more complex nanostructures, additional capping agents need to be introduced into the precursor solution to regulate particle growth at specific surfaces. For instance, it has been reported that Pt nanooctahedra can be synthesized by utilizing benzoic acid and N,N-dimethylformamide (DMF), where benzoic acid acts as shape-directing agent while DMF acts as both solvent and reducing agent.[12] For Pd nanobars, L-ascorbic acid and potassium bromide (KBr) are introduced to form (100) plane-terminated surfaces.[13] The introduction of additives can also help tailor the nanostructures. Lim et al. demonstrated that by adding $Co(acac)_2$ into the Pt precursor solution, Pt multipods and cemented Pt cubes could be generated;[14] Zhou et al. also showed that $Y(acac)_3$ could serve as co-capping agent for the formation of icosahedral structure.[15] Furthermore, by carefully adjusting the amount of $AgNO_3$ in the polyol process, one was able to transform the Pt nanostructure from cubic into cuboctahedral and octahedral.[16]

Kinetic control is another approach commonly adopted to modify the geometry of nanoparticles, since it greatly affects the diffusion and deposition rates and thus control the facet

development.[17] For example, the Pt nanostructures evolved from spherical particles to branched networks with decreasing reaction temperature in the present of oleylamine;[18] it was also found that lower temperature favors the formation of (111) surfaces and twin planes and thus the development of octahedral and icosahedral shapes.[19] Xia and his co-workers conducted a mechanistic study on Pd nanobars and nanorods and found that these anisotropic growths could be adjusted by tuning the reaction temperature, leading to nanostructures with different aspect ratios.[13] They later demonstrated that stacking fault-lined Pd nanoplates were favored over their single crystal and multiply twinned counterparts at lower reaction temperatures, presenting a rational approach for the synthesis of nanocrystals with desired and controlled twin structures and shapes.[20]

3.2 Experimental

3.2.1 Chemical and materials

Platinum acetylacetonate ($Pt(acac)_2$, Strem Chemicals, 98%); palladium acetylacetonate ($Pd(acac)_2$, Strem Chemicals, 99%); oleylamine (OAm, Sigma-Aldrich, 70%); oleic acid (OAc, Sigma-Aldrich, 90%); SiO_2 bead (SS03N, Bangs Laboratories, Inc.); SiO_2-NH_2 beads (SA03N, Bangs Laboratories, Inc.); acetone (Sigma-Aldrich, >99.5%); chloroform (Fisher Chemical, >99%); carbon black (Vulcan XC-72, Cabot); carbon monoxide (CO, research grade, Airgas); argon (Ar, UHP grade, Airgas). All were used as received.

3.2.2 Synthesis of carbon-supported Pt nanocubes

In order to synthesize Pt/C cubes, 16 mg carbon black was mixed with 8 mg of $Pt(acac)_2$ and 50 μL of OAm in 5 mL of acetone in a glass vial and sonicated for 15 min to form a well-diepersed precurosr solution. The precursor solution then was used to fill the container of an airbrush, followed by spraying onto a silicon wafer support on the conveyor belt, which was preheated to 120 °C. The silicon wafer support deposited with precursors was then transferred into the tubular reactor filled with CO to undergo thermal decomposition reaction. The moving rate of the belt was adjusted so the residence time of the precursor in the heating zone was 30

min, unless mentioned otherwise . Wall temperature of the tubular reactor was maintained at 230 °C by the heating tape. After the reaction, the products on the silicon wafer were easily collected by scratching with a spatula or rinsing with chloroform.

3.2.3 Synthesis of Pt catalysts on SiO_2 or NH_2-functionalized SiO_2 beads

The procedures were similar to the synthesis of cubic Pt/C, except that carbon black was replaced with SiO_2 or SiO_2-NH_2 beads, and no oleylamine or other long-chain ligands was added in the reaction mixtures.

3.2.4 Synthesis of carbon-supported truncated Pd nanooctahedra

In order to synthesize truncated octahedral Pd/C, 16 mg carbon black was mixed with 12 mg of $Pd(acac)_2$ and 50 μL of OAc in 5 mL of chlorofrom in a glass vial and sonicated for 15 min to form a well-diepersed precurosr solution. The precursor solution then was used to fill the container of an airbrush, followed by spraying onto a cover glass slides on the conveyor belt, which was preheated to 120 °C. The cover glass slides deposted with precursors was then transferred into the tubular reactor filled with CO to undergo thermal decomposition reaction, and the moving rate of the belt was adjusted so the residence time of the precursor in the heating

zone is 30 min . Wall temperature of the tubular reactor was maintained at 230 °C by the heating tape. After the reaction, the products on the cover glass slides can be easily collected by scratching with a spatula or rinsing with chloroform.

3.2.5 Synthesis of carbon-supported Pd nanoplates

The synthetic procedure was similar to that for carbon-supported truncated Pd nanooctahedra, except that oleic acid was replaced with oleylamine and the wall temperature was reduced to 210 °C. The residence time of the precursor in the heating zone and the flow rate of CO were still maintained at 30 min and 500 mL min^{-1}, respectively.

3.2.6 Synthesis of carbon-supported Pd nanosheets

The synthetic procedure was similar to that for carbon-supported truncated Pd nanooctahedra, except that oleic acid was replaced with oleylamine and the wall temperature was reduced to 190 °C. The residence time of the precursor in the heating zone was increased to 1 hr. The flow rate of CO was still maintained at 500 mL min^{-1}.

3.2.7 Characterization

Transmission electron microscopy (TEM) and high resolution TEM (HRTEM) images were recorded by JEOL Cryo 2100 microscope at an accelerating voltage of 200 kV. Powder X-ray diffraction (XRD) patterns were acquired on Bruker D8 Venture (DUO) diffractometer. thermogravimetric analysis (TGA) was determined by Q50-TGA with a ramp rate of 10 °C min^{-1} to 750 °C under air. UV-vis absorption spectra were collected in an Agilent Cary 60 UV-vis spectrophotometer.

3.3 Results and Discussion

3.3.1 Synthesis and characterization of carbon-supported Pt nanocubes and nanospheres

Uniform Pt cubes on carbon support (Pt/C) were obtained after the reactants passed through the reaction unit under flow of hot CO gas. TEM images show the Pt cubes were produced uniformly in both size and shape, and dispersed fairly evenly on top of the carbon support (**Figure 3.1**). The conveyor belt was moved at a rate, ranging from 3.20 to 1.06 to 0.53 cm min^{-1}, corresponding to residence time (*t*) of 10 min (**Figure 3.1a**), 30 min (**Figure 3.1b**), and 60 min (**Figure 3.1c**), respectively, inside the heating zone.

The average edge length of the cubes produced was between 3.5 and 3.8 nm based on the analysis of TEM images of Pt cubic nanoparticles (**Figure 3.1d–f**). High resolution TEM (HRTEM) image shows the d-spacing of lattice fringe for as-prepared cubic nanoparticles was 0.193 nm, matching well to the (200) plane of face-centered-cubic (fcc) Pt metal (inset in **Figure 3.1b**). The use of CO gas is critical for the formation of Pt nanocubes. When CO was switched to Ar, irregular Pt nanoparticles formed with the size ranging from 1 to 2 nm (**Figure 3.2**). CO gas in this reaction preferentially adsorbed onto selected Pt surfaces,[8, 21-22] so the deposition was facet dependent, resulting in the formation of {100} facets in the final form.[6-7, 23-24] The formation of sharp edges of as-prepared Pt cubes indicates that the reactor was absent of oxygen

or other unwanted gas species under CO purging. This result shows carbon-supported shaped nanocrystals can be produced in a continuous fashion by controlling the reaction parameters.

Effect of residence time on the particles size of Pt cubes on carbon support was examined. When the residence time was 10 min, both size and shape uniformity decreased slightly (**Figure 3.1a**) in comparison with those formed after 30 min, which had an average edge length of 3.8 ± 0.5 nm (**Figure 3.1 b**). There were more Pt nanoparticles ranging from 2 to 3 nm present in the final product at 10 min, suggesting the reaction time was not long enough for full growth into well-defined cubes. When the reaction time was longer than 30 min, well-defined cubic shape was observed (**Figure 3.1b,c**). All three samples though had a narrow size distribution, indicating the process of burst nucleation could happen in this system,[25-26] where Pt clusters were rapidly formed upon exposure to hot CO gas stream (**Figure 3.1d–f**). The size remained almost constant for reaction time up to 60 min, indicating $Pt(acac)_2$ precursors were consumed rapidly at the early stages.

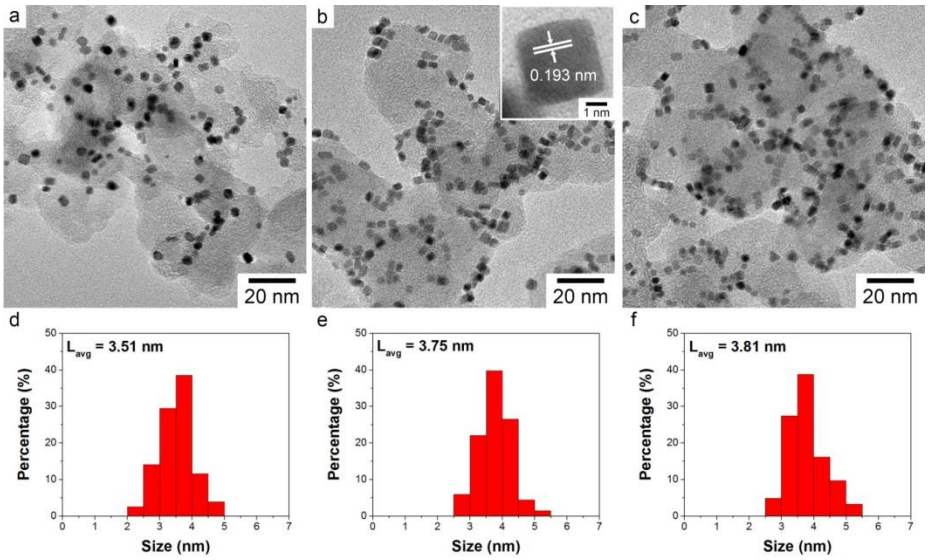

Figure 3.1 (a-c) TEM micrographs and (d-f) size distributions of as-made carbon-supported Pt nanocubes under reaction time of (a,d) 10 min, (b,e) 30min and (c,f) 60 min.

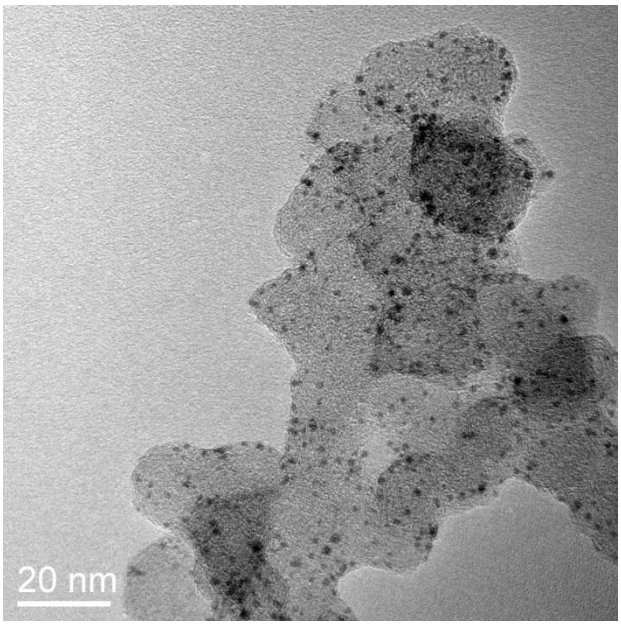

Figure 3.2 TEM micrograph of as-made Pt/C using Ar as the purging gas.

The flow rate of CO gas also affected the formation of particles greatly. When it decreased from 500 mL min^{-1} to 250 mL min^{-1}, the formed Pt nanoparticles became irregular in shape. The percentage of cubic nanostructures decreased to less than 75% (**Figure 3.3a**). One of the possible explanations is that air is capable of entering the system at this low flowrate. Unwanted gas species such as oxygen could compete with existing CO molecules. The preferential adsorptions of these gases on different Pt facets result in nanoparticulates enclosed by both {100) and {111} surfaces.[15, 27-28] If the CO flow rate was raised to 750 mL min^{-1}, the cubic shape was well preserved, while the particle size was slightly bigger than those synthesized under the CO flow rate of 500 mL min^{-1} (**Figure 3.3b**). Based on TEM micrographs, the size distribution became broader with increasing flow rate, whereas both average particle size and shape uniformity decreased with reducing flow rate (**Figure 3.3c, d**).

To gain a better idea of how different CO flow rates affect the particle growth and structure, we again apply overall energy balance on the tubular reactor. As mentioned in Chapter 2, the turbulence factor, β, is introduced to correct any deviation from the ideal internal forced convection case due to geometric factor, especially the Teflon stopper in the end of the reactor.[29] Because the early section of the reactor has the largest of effect on particle size, the temperature profile in this section is of highest interest. The turbulence factor in this section can be ignored, and the temperature at a given position along the quartz tube can be expressed by:

$$\frac{T_b - T_{b,i}}{T_w - T_b} = \frac{\pi \times D \times h \times L}{\rho \times \dot{V} \times C_P} \quad (1)$$

All parameters are the same as those reported in Chapter 2, except the heat transfer coefficient, h, which is a function of flow rate.

Figure 3.4a shows the calculated average temperature along the tube in an ideal internal forced convection case for different purging rate of CO. According to simulated temperature profile, at slower flow rate, the reaction temperature increases more rapidly when compared to that at higher flow rate, indicating the metal precursors will decompose much faster at 250 mL min^{-1} than at 500 mL min^{-1} and 750 mL min^{-1}. The minimum time required for thermal decomposition, $t_{min,req}$, can be related to the position where decomposition takes place by

$$t_{min,req} = \frac{L_{decomp}}{u_{belt}} \quad (2)$$

where the moving speed of the belt, u_{belt}, is 1.06 cm min^{-1}, and the critical distance, L_{decomp}, can be calculated by rearranging Eq. (1):

$$L_{decomp} = \frac{T_{decomp} - T_{b,i}}{T_w - T_{decomp}} \times \frac{\rho \times \dot{V} \times C_P}{\pi \times D \times h} \quad (3)$$

where T_{decomp} is equal to 180 °C, the decomposition temperature of $Pt(acac)_2$.

For the CO flow rate of 250 mL min^{-1}, $Pt(acac)_2$ takes less than 2 min to reduce to Pt metal when entering the heating zone, while it takes almost 5 min to react when the flow rate increase

to 750 mL min^{-1} (**Figure 3.4b**). Since faster ramping rate favors the burst nucleation process, the generation of a large amount of nuclei in a short period is favorable and leads to nanoparticles with monodisperse size distribution. Smaller particle size can also be attributed to fewer metal precursors left during the nucleation stage, shortening the later particle growth process. When the ramping rate is too slow, nucleation tends to occur randomly through the whole crystallization process and all of the particles have different growth histories, and this results in the uncontrollable growth of the particles and a broad size distribution.[25-26, 30-33]

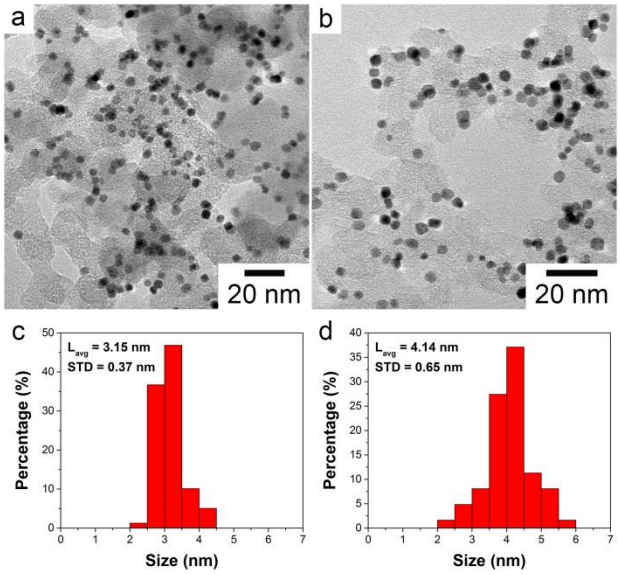

Figure 3.3 (a,b) TEM micrographs and (c,d) size distributions of as-made carbon-supported Pt nanocatalysts under CO flow rate of (a,c) 250 mL min^{-1} and (b,d) 750 mL min^{-1}.

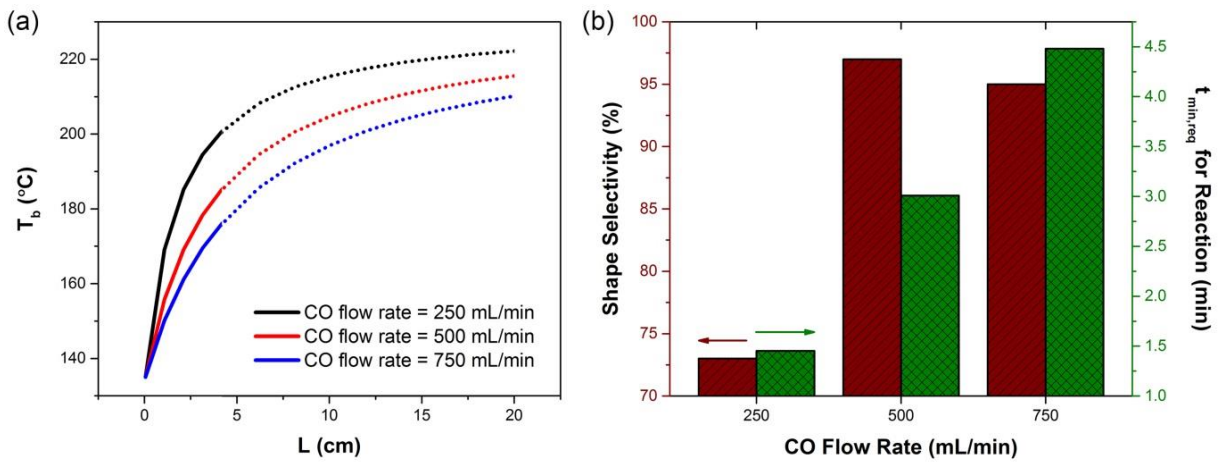

Figure 3.4 (a) Calculated temperature profiles (β=1) inside the tubular reactor and at wall temperature of 230 °C under different CO flow rates. (b) Summary of percentage of cubic structure in the final products and minimum time required for thermal decomposition of $Pt(acac)_2$ under different CO flow rates.

3.3.2 Synthesis and characterization of carbon-supported Pd truncated nanooctahedra, nanoplates and nanosheets

Uniform and well-dispersed truncated octahedral Pd/C was formed when using $Pd(acac)_2$ as the metal precursor (**Figure 3.5a**). The particle size was 3.45 ± 0.57 nm which was smaller than the Pd nanocrystals synthesized via colloidal synthetic approach[2, 34-35]. This result comes from the increased interaction between metal and support as well as faster kinetics in the conveyor transport system.

When the wall temperature of the reactor was decreased to 210 °C, the morphology of Pd nanostructure change from truncated octahedral to nanoplates with the length of around 7 nm (**Figure 3.5b**), and further elongating the reaction time will transform the geometry from plate-like into sheet-like shape with even bigger dimension (**Figure 3.5c**). From HRTEM micrographs, the d-spacing between lattice fringes for all three Pd nanostructures matched well to fcc (111) Pd metal, although the morphologies were different, indicating variations of binding energies of CO molecules on the different metal surfaces (**Figure 3.5d-f**). Although CO adsorbs onto Pt(100) stronger than other facets, it tends to preferentially adsorb onto Pd(111) over others, making Pd nuclei to grow into (111)-terminated nanostructures.[8, 36-37]

During the reaction, metal precursor was first reduced or decomposed to form small clusters via self-nucleation. Once the clusters grew past a certain size, they become seeds with a well-defined structure. According to Wulff's theorem (or Wulff construction) these seeds tend to grow into structures that can minimize the total interfacial free energy with a given volume.[38-39] For an fcc structure, the interfacial free energy, γ, follows the energetic sequence of $\gamma_{\{111\}} < \gamma_{\{100\}} < \gamma_{\{110\}}$. Considering both (111) surface-bound octahedral and tetrahedral shapes have larger surface area than (111) surface-bound cubic shape of the same volume, the single crystal seeds will actually exist as cuboctahedra, or the so-called Wulff polyhedrons, enclosed by a mix of {111} and {100} facets to reach minimal total interfacial free energy. [40, 41-42] Under CO

environment, Pd(111) will be covered by CO molecules, so when Pd^{2+} cations diffuse to cuboctahedral Pd seeds, they can only precipitate onto (100) surfaces. Eventually, the plane with the slowest growth rate becomes the dominating surface bounding the final particles; in this case, either single crystalline octahedron or truncated octahedron.

If the reduction or decomposition is slow, known as kinetically-controlled process, the atoms tend to form nuclei and seeds through random hexagonal close packing (r-hcp) together with the inclusion of stacking faults, leading to the formation of plate-like seeds. These seeds are covered by {111} facets at the top and bottom surfaces, with stacking faults formed along the vertical direction. The strain energy and thus the total free energy can be compensated by increased surface coverage with low-energy {111} facets, making rhcp structure slightly more stable than its fcc counterpart at this stage. Decreased reaction temperature and increased reaction time facilitate the anisotropic growth, and the rhcp Pd nanostructures grow into (111)-terminated nanosheets. Similar nanostructures were also observed in those generated via colloidal synthesis in the presence of CO gas.[9, 43] The decreased shape uniformity of carbon-supported Pd nanosheets as compared to nanoplates and truncated nanooctahedra can be explained by the presence of carbon support during the thermal decomposition reaction, which inhibits the particle growth in 2D direction.

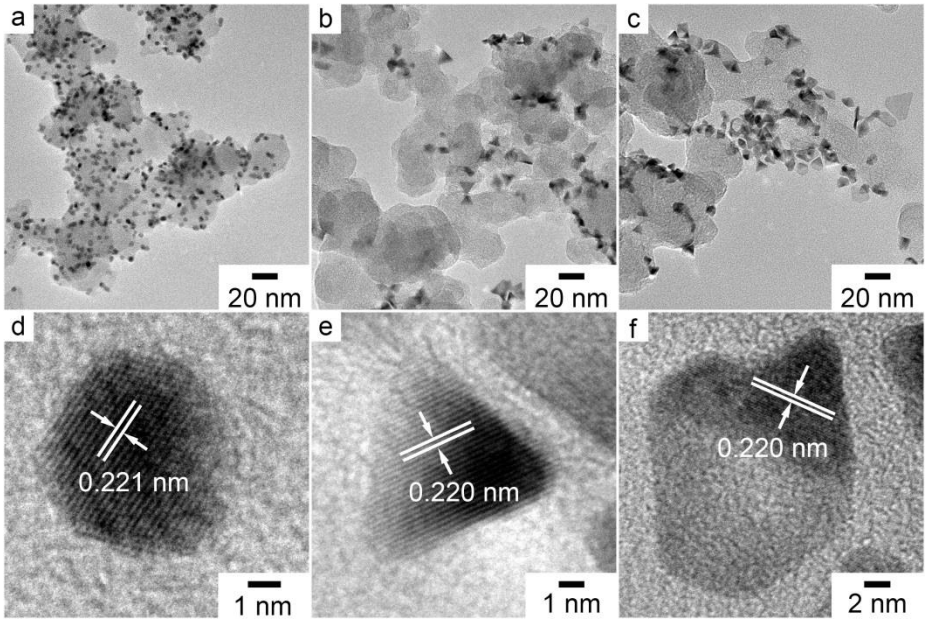

Figure 3.5 (a-c) TEM and (d-f) HRTEM micrographs of as-made carbon-supported (a,d) truncated Pd nanooctahedra, (b,e) Pd nanoplates, and (c,f) Pd nanosheets under hot CO environment.

3.3.3 Interaction between ligands (oleylamine and oleic acid) and metal precursors

Since CO is the shape-directing agent in the system, long-chain ligands such as oleylamine and oleic acid were not required in the synthesis of carbon-supported Pt and Pd nanocatalysts, respectively. The post-treatment process is simplified because these ligands usually need to be removed from the system before conducting heterogeneous catalytic reactions. However, in the absence of oleylamine and oleic acid, both metal loading and metal dispersion significantly decreased. The as-made particles were also much bigger with broader size distributions (**Figure**

3.6). Since both cubic and octahedral structures can still be observed in the system, CO was proven to be the main factor for the formation of {100} and {111} facets, while oleylamine and oleic acid were largely responsible for anchoring the metal precursors on the carbon support to achieve high metal loading and even dispersion. The anchoring effects of these ligands were also supported by the observation that Pt nanoparticles were well dispersed with using oleylamine-containing precursor solutions regardless of the choice of gases (**Figure 3.1** and **Figure 3.2**). A control experiment on the effect of ligand on catalyst immobilization was carried out using silica beads functionalized with amine groups in the absence of oleylamine (**Figure 3.7**). Pt nanoparticles had a higher dispersion on the surface of amine-functionalized silica beads than those beads without the amine group. This result indicates that the amine group did play a critical role in anchoring Pt nanoparticles on the carbon support.

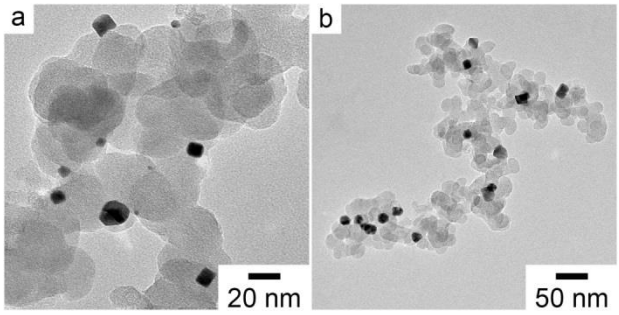

Figure 3.6 TEM micrographs of carbon-supported (a) Pt and (b) Pd nanoparticles under hot CO environment but in the absence of long-chain ligands.

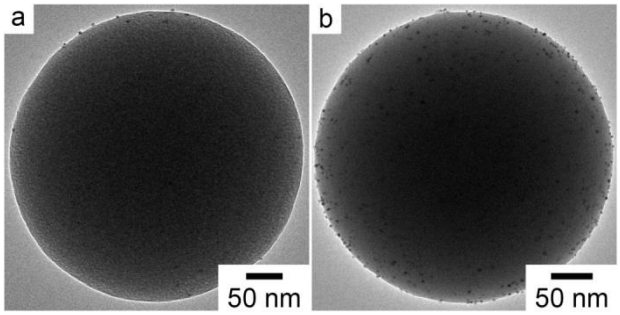

Figure 3.7 TEM micrographs of as-prepared Pt nanoparticles supported on: (a) SiO_2 and (b) SiO_2-NH_2 beads.

To better understand the interaction between ligands and metal reactants, different amounts of oleylamine and oleic acid were used to prepare a series of carbon-supported Pt and Pd nanocrystals, respectively (**Figure 3.8**). Deposition of metal nanocrystals remained high, especially for Pt/C, as long as the molar ratio between ligands and metal acetylacetonates was above four. The metal loading on the carbon support was examined by TGA, as shown in **Figure 3.9**. When the molar ratio between ligand and $M(acac)_2$ was higher than four, the resulting metal loading was very close to 20 wt%, which correlates to complete conversion of $M(acac)_2$ into M^0 metal. When this ratio decreased to less than four, the loading began to drop.

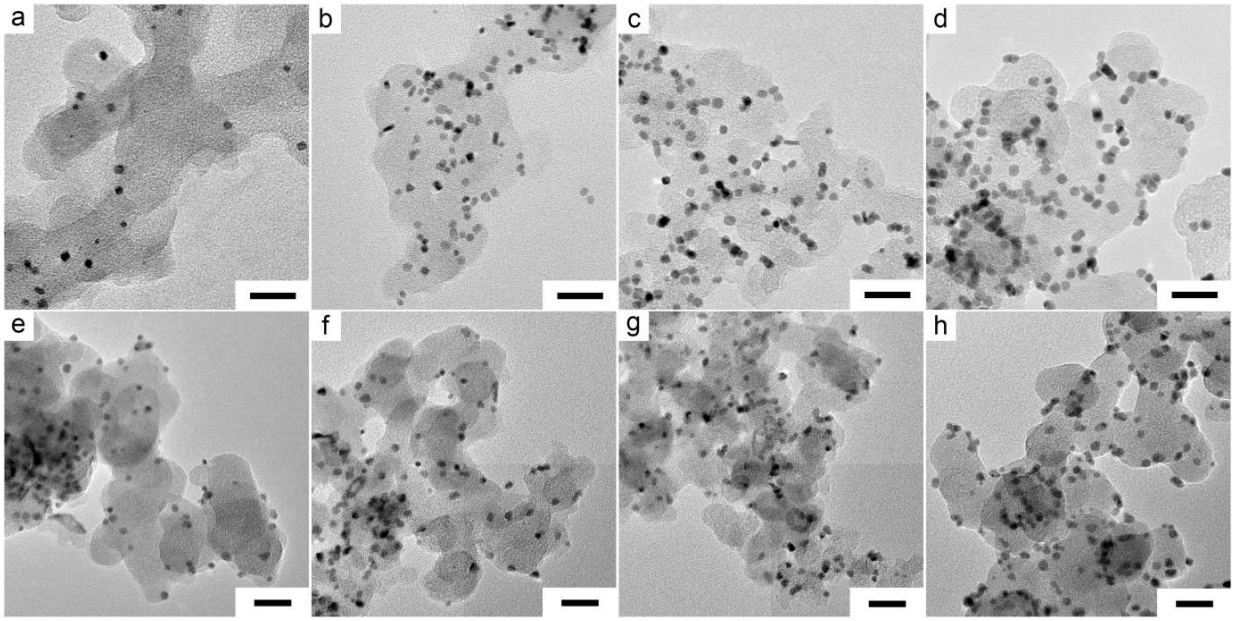

Figure 3.8 TEM micrographs of carbon-supported (a-d) Pt nanocubes and (e-h) truncated Pd nanooctahedra. The reaction conditions and precursor preparations are the same as those for Figure 3.1b and Figure 3.5a, except that the addition of ligands change from 50 μL to (a,e) 10 μL, (b,f) 20 μL, (c,g) 30 μL, and (d,h) 40 μL. Scale bars are 20 nm.

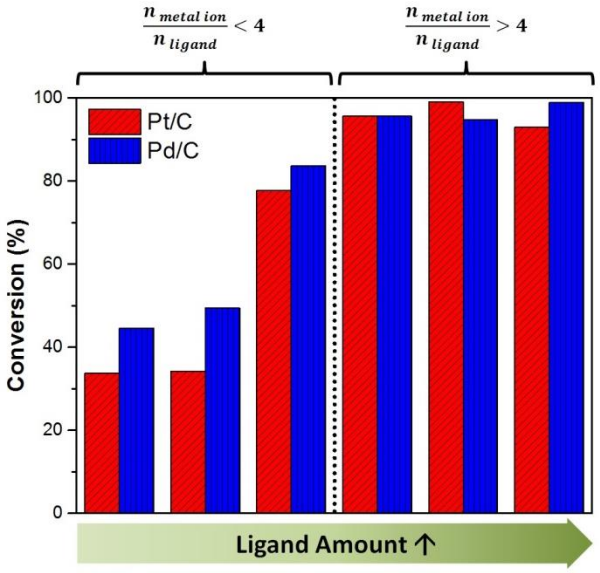

Figure 3.9 TGA results of Pt/C and Pd/C synthesized with different amounts of ligands. The amounts, for the columns from left to right, are 0, 10, 20, 30, 40 and 50 μL, respectively.

These observations suggest oleylamine and oleic acid could react with $Pt(acac)_2$ and $Pd(acac)_2$ to form $[Pt\text{-}((C_{18}H_{35})NH_2)_4]^{2+}$ and $[Pd\text{-}((C_{17}H_{33})COOH)_4]^{2+}$ complexes, respectively, where each M^{2+} coordinates with four ligands via electron lone pairs on either nitrogen atom of amine group or oxygen atom of acid group:

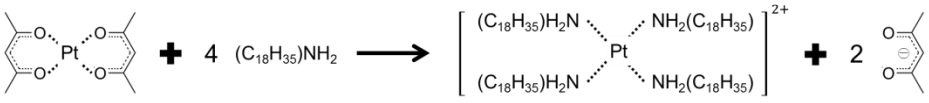

(4)

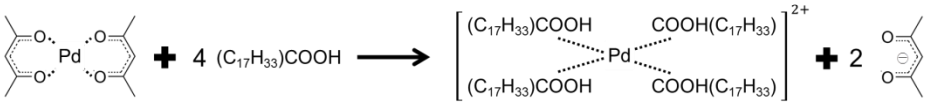

(5)

The complexation was further monitored by UV-Vis spectroscopy (**Figure 3.10**), which is a useful technique for identifying new species because different molecules can absorb radiation with different wavelengths. When metal precursors were mixed with ligands at elevated temperatures, they showed very distinct peaks in comparison to their individual counterparts. Both curves have a characteristic peak at around 272 nm and were different from simply superimposing the spectra obtained from solutions containing pure metal acetylacetonates and pure ligand solution, or the mixture solution formed at room temperature. It can be concluded that when the precursor solution reached the preheated silicon wafer or cover glass slide on the conveyor belt during the deposition stage, ligands would replace the acetylacetonate groups in the metal precursors to form a new complex. The long carbon chain of this complex can thus immobilize onto the carbon support due to similar hydrophobicity (**Figure 3.11**).

The complex formation between Pt and R-NH_2 (R = alkyl) has been proposed for cases when oleylamine was replaced with other capping agents or in the process of morphological transition in Pt-M nanocrystals.[44-45] This kind of complexation also exists in other transition metals, such as Pd,[46-47] Au,[48-49] and Cu.[50] The Pt-NHR complex was also observed by mass spectrum, in which $Pt(acac)_2$ first reacted with octadecylamine and form surfactant-ligated precursor $[Pt(acac)(NHR)]_n$.[51]

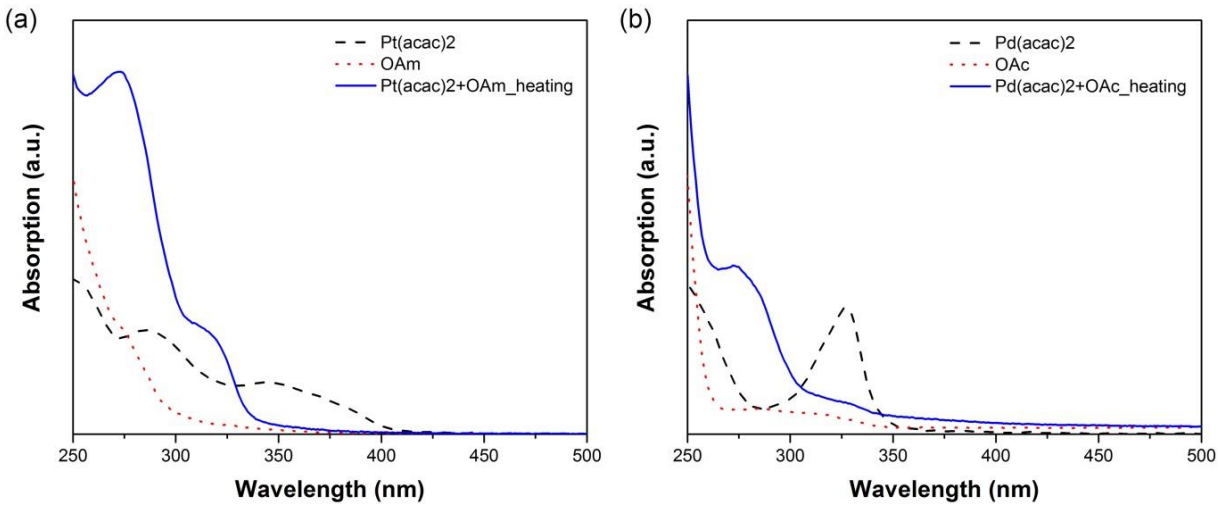

Figure 3.10 UV-Vis spectrum of a chloroform solution dissolved with metal acetylacetonates, ligands or their mixture in (a) Pt-OAm system and (b) Pd-OAc system.

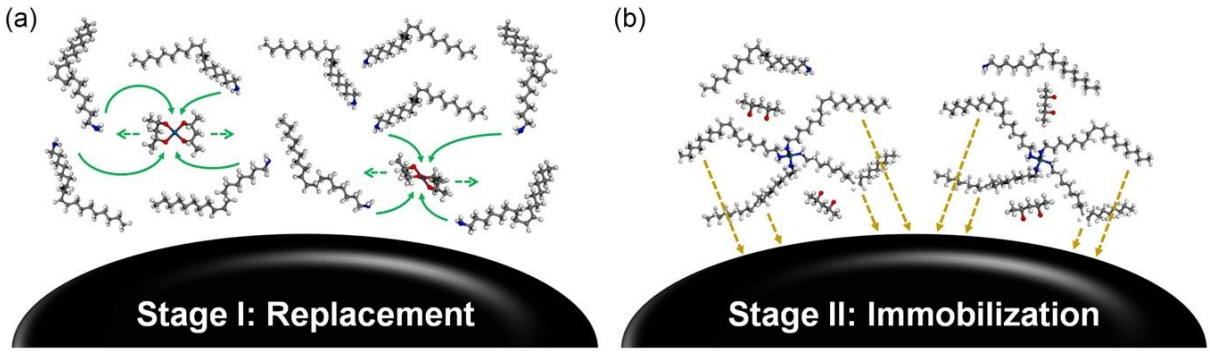

Figure 3.11 Schematic illustration of complex formation between $Pt(acac)_2$ and oleylamine.

3.4 Conclusion

A novel conveyor transport system was developed for synthesizing carbon-supported highly uniform Pt nanocubes and truncated Pd nanooctahedra in a continuous production fashion. Nanostructures can be further manipulated by introduction of additives and adjusting the reaction temperature. CO is important for controlling the shape, while ligands help to increase the loading and even dispersion of metal nanocrystals on carbon support due to the complex formation at deposition stage. This conveyor transport system is an important advancement toward the continuous manufacturing of supported catalysts with uniform size, shape, and composition in a single-reaction system.

3.5 References

1. Leong, G. J.; Schulze, M. C.; Strand, M. B.; Maloney, D.; Frisco, S. L.; Dinh, H. N.; Pivovar, B.; Richards, R. M. *Appl. Organomet. Chem.* **2014**, *28*, 1-17.

2. Chen, A. C.; Ostrom, C. *Chem. Rev.* **2015**, *115*, 11999-12044.

3. Hwang, S. Y.; Zhang, M.; Zhang, C.; Ma, B.; Zheng, J.; Peng, Z. *Chem. Commun.* **2014**, *50*, 14013-14016.

4. Zhang, C.; Hwang, S. Y.; Peng, Z. *J. Mater. Chem A* **2013**, *1*, 14402-14408.

5. Peng, Z.; Kisielowski, C.; Bell, A. T. *Chem. Commun.* **2012**, *48*, 1854-1856.

6. Wu, B.; Zheng, N.; Fu, G. *Chem. Commun.* **2011**, *47*, 1039-1041.

7. Kang, Y.; Ye, X.; Murray, C. B. *Angew. Chem.-Int. Edit.* **2010**, *49*, 6156-6159.

8. Palaikis, L.; Zurawski, D.; Hourani, M.; Wieckowski, A. *Surf. Sci* **1988**, *199*, 183-198.

9. Huang, X.; Tang, S.; Mu, X.; Dai, Y.; Chen, G.; Zhou, Z.; Ruan, F.; Yang, Z.; Zheng, N. *Nat. Nanotechnol.* **2011**, *6*, 28-32.

10. Pan, Y.-T.; Yin, X.; Kwok, K. S.; Yang, H. *Nano Lett.* **2014**, *14*, 5953-5959.

11. Yin, X.; Liu, X.; Pan, Y.-T.; Walsh, K. A.; Yang, H. *Nano Lett.* **2014**, *14*, 7188-7194.

12. Huang, X.; Zhao, Z.; Chen, Y.; Zhu, E.; Li, M.; Duan, X.; Huang, Y. *Energ. Environ. Sci.*

2014, *7*, 2957-2962.

13. Xiong, Y.; Cai, H.; Wiley, B. J.; Wang, J.; Kim, M. J.; Xia, Y. *J. Am. Chem. Soc.* **2007**, *129*, 3665-3675.

14. Lim, S. I.; Ojea-Jimenez, I.; Varon, M.; Casals, E.; Arbiol, J.; Puntes, V. *Nano Lett.* **2010**, *10*, 964-973.

15. Zhou, W.; Wu, J.; Yang, H. *Nano Lett.* **2013**, *13*, 2870-2874.

16. Rioux, R. M.; Song, H.; Grass, M.; Habas, S.; Niesz, K.; Hoefelmeyer, J. D.; Yang, P.; Somorjai, G. A. *Top. Catal.* **2006**, *39*, 167-174.

17. Barth, J. V.; Costantini, G.; Kern, K. *Nature* **2005**, *437*, 671-679.

18. Zhang, H. T.; Ding, J.; Chow, G. M. *Langmuir* **2008**, *24*, 375-378.

19. Kang, Y. J.; Pyo, J. B.; Ye, X. C.; Diaz, R. E.; Gordon, T. R.; Stach, E. A.; Murray, C. B. *ACS Nano* **2013**, *7*, 645-653.

20. Wang, Y.; Peng, H.-C.; Liu, J.; Huang, C. Z.; Xia, Y. *Nano Lett.* **2015**, *15*, 1445-1450.

21. Eichler, A. *Surf. Sci.* **2002**, *498*, 314-320.

22. Herrero, E.; Franaszczuk, K.; Wieckowski, A. *J. Phys. Chem.* **1994**, *98*, 5074-5083.

23. Wu, J.; Gross, A.; Yang, H. *Nano Lett.* **2011**, *11*, 798-802.

24. Chen, G.; Tan, Y.; Wu, B.; Fu, G.; Zheng, N. *Chem. Commun.* **2012**, *48*, 2758-2760.

25. Lamer, V. K. *Ind. Eng. Chem.* **1952**, *44*, 1270-1277.

26. Lamer, V. K.; Dinegar, R. H. *J. Am. Chem. Soc.* **1950**, *72*, 4847-4854.

27. Lim, D. H.; Wilcox, J. *J. Phys. Chem. C* **2011**, *115*, 22742-22747.

28. Qi, L.; Qian, X. F.; Li, J. *Phys. Rev. Lett.* **2008**, *101*, 1-4.

29. Tsao, K. C.; Yang, H. *Small* **2016**, *12*, 4808-4814.

30. Robb, D. T.; Privman, V. *Langmuir* **2008**, *24*, 26-35.

31. Mankin, M. N.; Mazumder, V.; Sun, S. *Chem. Mater.* **2011**, *23*, 132-136.

32. van Embden, J.; Chesman, A. S. R.; Jasieniak, J. J. *Chem. Mater.* **2015**, *27*, 2246-2285.

33. Wang, F. D.; Richards, V. N.; Shields, S. P.; Buhro, W. E. *Chem. Mater.* **2014**, *26*, 5-21.

34. Lim, B.; Jiang, M. J.; Tao, J.; Camargo, P. H. C.; Zhu, Y. M.; Xia, Y. N. *Adv. Func. Mater.* **2009**, *19*, 189-200.

35. Zhang, H.; Jin, M. S.; Xiong, Y. J.; Lim, B.; Xia, Y. N. *Acc. Chem. Res.* **2013**, *46*, 1783-1794.

36. Hammer, B.; Morikawa, Y.; Norskov, J. K. *Phys. Rev. Lett.* **1996**, *76*, 2141-2144.

37. Wong, Y. T.; Hoffmann, R. *J. Phys. Chem.* **1991**, *95*, 859-867.

38. Marks, L. D. *Rep. Prog. Phys.* **1994**, *57*, 603-649.

39. Wulff, G. *Z Krystallogr. Mineral* **1901**, *34*, 449-530.

40. Xia, Y. N.; Xiong, Y. J.; Lim, B.; Skrabalak, S. E. *Angew. Chem.-Int. Edit.* **2009**, *48*, 60-103.

41. Wang, Z. L. *J. Phys. Chem. B* **2000**, *104*, 1153-1175.

42. Zhang, J. M.; Ma, F.; Xu, K. W. *Appl. Surf. Sci.* **2004**, *229*, 34-42.

43. Hwang, S. Y.; Zhang, M. Z.; Zhang, C. L.; Ma, B. Y.; Zheng, J.; Peng, Z. M. *Chem. Commun.* **2014**, *50*, 14013-14016.

44. Tzitzios, V.; Niarchos, D.; Gjoka, M.; Boukos, N.; Petridis, D. *J. Am. Chem. Soc.* **2005**, *127*, 13756-13757.

45. Chen, M.; Kim, J.; Liu, J. P.; Fan, H. Y.; Sun, S. H. *J. Am. Chem. Soc.* **2006**, *128*, 7132-7133.

46. Niu, Z.; Peng, Q.; Gong, M.; Rong, H.; Li, Y. *Angew. Chem. Int. Ed.* **2011**, *50*, 6315-6319.

47. Ortiz, N.; Skrabalak, S. E. *Angew. Chem. Int. Ed.* **2012**, *51*, 11757-11761.

48. Huo, Z.; Tsung, C.-k.; Huang, W.; Zhang, X.; Yang, P. *Nano. Lett.* **2008**, *8*, 2041-2044.

49. Lu, X.; Yavuz, M. S.; Tuan, H.-Y.; Korgel, B. A.; Xia, Y. *J. Am. Chem. Soc.* **2008**, *130*, 8900-8901.

50. Kumar, D. V. R.; Kim, I.; Zhong, Z.; Kim, K.; Lee, D.; Moon, J. **2014**, *16*, 22107-22115.

51. Yoon, J.; Nguyen Tien, K.; Kim, H.; Kim, B.; Baik, H.; Back, S.; Lee, S.; Lee, S.-W.; Kwon, S. J.; Lee, K. *Chem. Commun.* **2013**, *49*, 573-575.

Chapter 4:

Synthesis of Supported and Shaped Bimetallic Alloy Nanocatalysts Using Conveyor Transport System[3]

4.1 Introduction

Bimetallic catalysts can exhibit very different chemical and electronic properties from their parent metals, and the flexibility in the design of the nanostructure also allows greater tune-ability in the reactivity. Since Pt alloys were reported as superior ORR catalysts in the 1980s, tremendous efforts have been made to developed highly active and durable Pt-based ORR electrocatalysts for PEM fuel cells, including catalysts of Pt alloyed with either early or late transition metals (L/ETMs).[1-2] Such attempts have made Pt catalysts the most commonly used cathode materials to catalyze ORR.

Researchers have been focusing on enhancing ORR performance by alloying Pt with several late transition metals, resulting in changes in electronic structure of Pt and enhanced catalytic performance. Among these metals, nickel, cobalt and iron have been widely studied.[3-8] Since ORR activity depends on both composition and structure, developing shape-controlled Pt-LTM alloy catalysts has drawn significant interest over the last several years.[9]

[3] Modified with permission, from Tsao, K.-C.; Yang, H. *Small* **2016**, *12,* 4808-4814.

Inspired by the superior ORR activity, researchers have created nanoparticles with a $Pt_3Ni(111)$ surface structure.[10] Zhang et al. synthesized (111)-terminated Pt_3Ni nanooctahedral via a wet chemical synthesis. When compared to cubic Pt catalyst, the octahedral counterpart showed ~7 and ~4 times enhancement in specific and mass activity, respectively.[11] Yang group demonstrated that the GRAILS method is capable of generating well-defined octahedral and icosahedral Pt_3Ni nanoparticles,[12-13] which exhibit increased activity towards ORR than the truncated octahedral ones.[14] Xia and his co-workers later reported Pt-Ni nanooctahedra with a very high activity of 3.3 A mg_{Pt}^{-1}, by introducing benzyl ether into the reaction system to lower the surface coverage of the surfactant.[15] To further improve the ORR performance, several surfactant-free approaches are adopted for the synthesis of shaped Pt-alloy nanoparticles, using either N,N-dimethylformamide or N-formylpiperidine as both solvent and reductant.[16-18] When benzoic acid is introduced as a shape-directing agent, carbon-supported octahedral Pt-Ni catalysts can be generated in a single step without additional surfactant removal process.[19] Furthermore, when doped with transition metals, such as molybdenum, these catalysts were reported to have 81- and 73-fold enhancements in specific and mass activity for ORR, respectively.[20]

Although those catalysts made of Pt-LTM alloys exhibit high ORR activity, the non-noble transition metals often suffer from dissolution in the acidic operation conditions. Based on

computational screening, Pt-ETM alloys are expected to possess good stability because of their negative heat of formation, which corresponds to large energy barriers for diffusion of these rare transition metals to surface, thus lowering the tendency to leach out.[21-22] Yoo and Chorkendorff have developed various types of alloy catalysts with extended surfaces. Sung's group found that Pt-ETM alloys are more stable than Pt-Ni and Pt-Co catalysts.[23-26] Chorkendorff and his co-workers further synthesized a number of alloys with higher activity and stability towards ORR due to the presence of Pt overlayer and compressive strain effect.[27-31]

Because of the large difference in standard reduction potentials between late and early transition metals, these kinds of alloys are mostly synthesized in bulk and polycrystalline form through the vapor-phase, physical deposition. Chemical routes for supported catalysts of these Pt-ETM alloys, however, have not shown much success. More work needs to be done for the synthesis of Pt-ETM in nanoparticulate form to further enhance its activity.[32-33]

This chapter will focus on the synthesis of carbon-supported Pt alloyed with Ni, Co and Fe. Synthetic approaches, optimization of reaction conditions and material characterizations will also be detailed in the following sections. The conveyor transport system can also be applied to Pt-ETMs by replacing Teflon- or silicone-coated fiberglass tape with other high-temperature heat-resistant fiberglass tapes, but will not be discussed here.

4.2 Experimental

4.2.1 Chemical and materials

Platinum acetylacetonate ($Pt(acac)_2$, Strem Chemicals, 98%); palladium acetylacetonate ($Pd(acac)_2$, Strem Chemicals, 99%); nickel acetylacetonate ($Ni(acac)_2$, Sigma-Aldrich, 95%); cobalt acetylacetonate ($Co(acac)_2$, Sigma-Aldrich, 97%); iron acetylacetonate ($Fe(acac)_3$, Sigma-Aldrich, >99.9%); chloroplatinic acid solution (H_2PtCl_6, 8 wt. % in H_2O); nickel chloride hexahydrate ($NiCl_2 \cdot 6H_2O$, ReagentPlus grade); oleylamine (OAm, Sigma-Aldrich, 70%); oleic acid (OAc, Sigma-Aldrich, 90%); diphenyl ether (DPE, Sigma-Aldrich, 99%); dopamine HCl ($C_8H_{11}NO_2 \cdot HCl$, Alfa Aesar, 99%); tris-HCl buffer ($C_4H_{11}NO_3 \cdot HCl$, bioWORLD, pH=8.5, 10mM); chloroform (Fisher Chemical, >99%); ethanol (Decon Labs, 200 proof); carbon black (Vulcan XC-72, Cabot); carbon monoxide (CO, research grade, Airgas); argon (Ar, UHP grade, Airgas); nitrogen (N_2, UHP grade, Airgas). All were used as received.

4.2.2 Synthesis of carbon-supported cubic Pt-M alloys (M = Ni, Co, Fe)

In order to synthesize cubic Pt_3Ni/C, 16 mg carbon black was mixed with 7 mg of $Pt(acac)_2$, 2 mg of $Ni(acac)_2$, 80 μL of OAm, and 20 μL of OAc in 10 mL of chloroform in a glass vial and sonicated for 15 min to form a well-diepersed precurosr solution. The precursor solution then

was used to fill the container of an airbrush, followed by spraying onto a cover glass slide on the conveyor belt, which was preheated to 120 °C. The cover glass slide deposted with precursors was then transferred into the tubular reactor filled with CO to undergo thermal decomposition reaction, and the moving rate of the belt was adjusted so the residence time of the precursor in the heating zone is 1 hr, corresponding to the moving rate of 0.53 cm min^{-1} for the conveyor belt. Wall temperature of the tubular reactor was maintained at 230 °C by the heating tape. After the reaction, the products on the cover glass slide can be easily collected by scratching with a spatula or rinsing with chloroform. For the synthesis of cubic Pt_3Co/C and Pt_3Fe/C, Ni precursor was replaced with 2 mg of $Co(acac)_2$ and 2 mg of $Fe(acac)_3$, respectively.

4.2.3 Synthesis of carbon-supported octahedral Pt-M alloys (M = Ni, Co, Fe)

The synthetic procedure was similar to that for carbon-supported cubic Pt-M alloys, except that oleic acid was replaced with either diphenyl ether (smaller particle size) or benzyl ether (larger particle size) with total volume remain at 100 μL (80 μL for oleylamine and 20 μL for either diphenyl ether or benzyl ether), unless mentioned otherwise. The residence time of the precursor in the heating zone and the wall temperature of the tubular reactor were still maintained at 1 hr and 230 °C, respectively.

4.2.4 Synthesis of polydopamine-coated carbon (PDA-C)

30 mg of carbon black was dispersed in 30 mL of tris-HCl buffer and sonicated for 15 min, followed by the addition of 60 mg of dopamine HCl. The solution was stirred at room temperature for 24 h. The product was collected by centrifugation, washed with distilled water for two times and ethanol for one time, and then dried in an oven at 60 °C overnight to form polydopamine-coated carbon black (PDA-C).

4.2.5 Synthesis of PDA-C-supported Pt nanocubes

In order to synthesize cubic Pt/PDA-C, 16 mg of PDA-C was mixed with 100 μL of H_2PtCl_6 aqueous solution in 5 mL of ethanol in a glass vial and sonicated for 15 min to form a well-diepersed precurosr solution. The precursor solution then was used to fill the container of an airbrush, followed by spraying onto a cover glass slide on the conveyor belt, which was preheated to 120 °C. The cover glass slide deposted with precursors was then transferred into the tubular reactor filled with CO to undergo thermal decomposition reaction, and the moving rate of the belt was adjusted so the residence time of the precursor in the heating zone is 30 min, corresponding to the moving rate of 1.06 cm min^{-1} for the conveyor belt. Wall temperature of the

tubular reactor was maintained at 230 °C by the heating tape. After the reaction, the products on the cover glass slide can be easily collected by scratching with apathula or rinsing with ethanol.

4.2.6 Synthesis of PDA-C-supported octahedral Pt_3Ni alloys

The procedures were similar to the synthesis of cubic Pt/PDA-C, except that 90 μL H_2PtCl_6 aqueous solution and 1.5 mg of $NiCl_2{\cdot}6H_2O$ were used as metal precursors. For more accurate measurement, $NiCl_2{\cdot}6H_2O$ was dissolved in ethanol in advance to form a stock solution, and stoichiometric amount of $NiCl_2{\cdot}6H_2O$ ethanol solution were extracted and added into the precursor solution with total volume of ethanol equal to 5 mL.

4.2.7 Characterizations

Transmission electron microscopy (TEM) and high resolution TEM (HRTEM) images were recorded by JEOL Cryo 2100 microscope at an accelerating voltage of 200 kV. Overall energy dispersive X-ray (EDX) spectrum was conducted by Hitachi S4700 microscope equipped with Oxford Link Isis as elemental analyzer. Powder X-ray diffraction (XRD) patterns were acquired on Bruker D8 Venture (DUO) diffractometer. TGA was determined by Q50-TGA with a ramp rate of 10 °C min^{-1} to designated temperatures under air or nitrogen atmosphere.

4.3 Results and Discussion

4.3.1 Synthesis and characterization of carbon-supported cubic and octahedral Pt-M alloys with the introduction of capping ligands

Although CO molecules prefer to adsorb onto Pt(100) surfaces over the others, not all transition metals have similar trends.[34-39] Therefore, other capping agents were introduced in the precursor solution to better control the morphology of bimetallic nanostructures. To better understand the effect of capping agent amount on the geometry of as-made nanocrystals, a series of carbon-supported Pt-Ni nanoparticles were synthesized with different addition of oleylamine, oleic acid, and diphenyl ether (**Figure 4.1**). When certain amount of oleic acid and diphenyl ether were introduced in the system, uniform cubic and octahedral Pt-Ni/C were obtained, respectively (**Figure 4.1b and f**). Slightly decrease the amount of capping agents lower the shape uniformity, though nanoparticles were still well dispersed on the carbon support (**Figure 4.1a and e**). However, when the amount of oleylamine was too low, both shape uniformity and metal dispersion all significantly decreased, and size distribution became much broader (**Figure 4.1c-d and e-f**). This again verified the importance of oleylamine as both complexing agent and binding agent for uniform Pt metal dispersion on the support, and these newly formed Pt clusters can serve as and both seed and catalysts for later deposition and growth of Pt and Ni metals.[40]

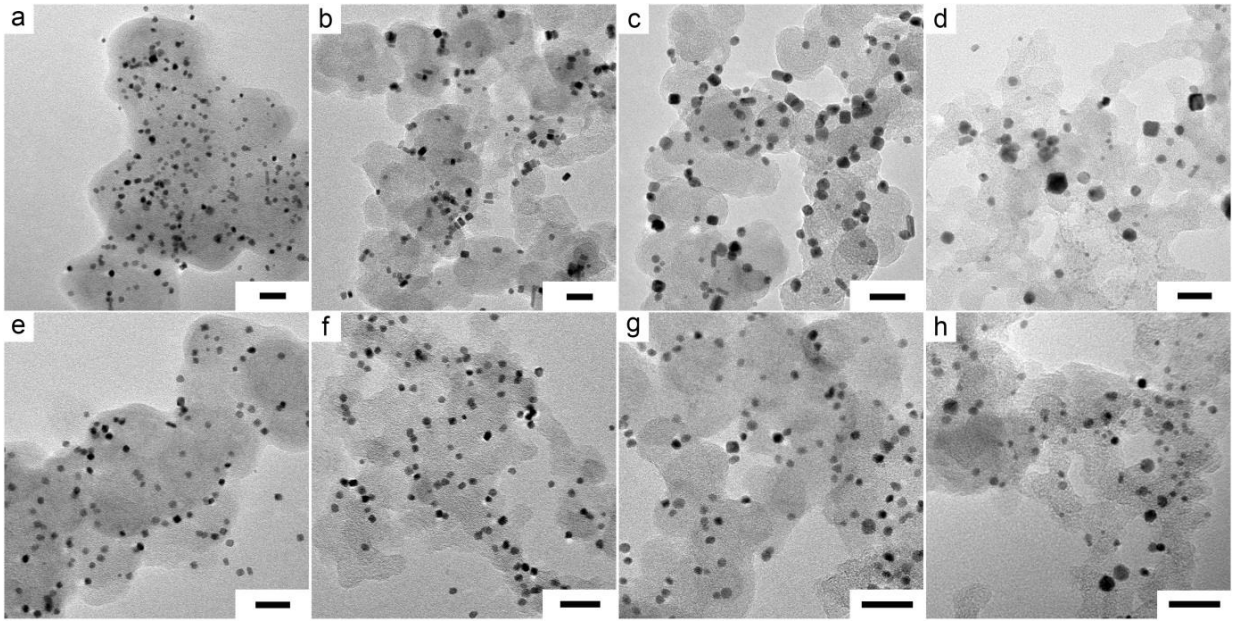

Figure 4.1 (a-h) TEM micrographs of carbon-supported Pt-Ni nanoparticle with introduction of (a-d) oleylamine and oleic acid and (e-h) oleylamine and diphenyl ether. Precursor solution for each sample consists of 16 mg of carbon black, 7 mg of $Pt(acac)_2$, 2 mg of $Ni(acac)_2$, 5 mL of chloroform, and 50 μL of ligand. The volumetric ratio of oleylamine and the other capping agent: (a,e) 45:5. (b,f) 40:10. (c,g) 35:15. (d,h) 30:20. Reaction conditions: T_{wall} = 230 °C; reaction time = 30 min; V_{CO} = 500 mL min^{-1}. Scale bars are 20 nm.

Both size distribution and shape uniformity analysis were summarized in **Figure 4.2**. The narrowest size distribution and the highest shape uniformity could be achieved when volumetric ratio between oleylamine and oleic acid (or diphenyl ether) was 4:1. This optimal value also indicated that any change in ligand addition can has huge impact on the final nanostructures.

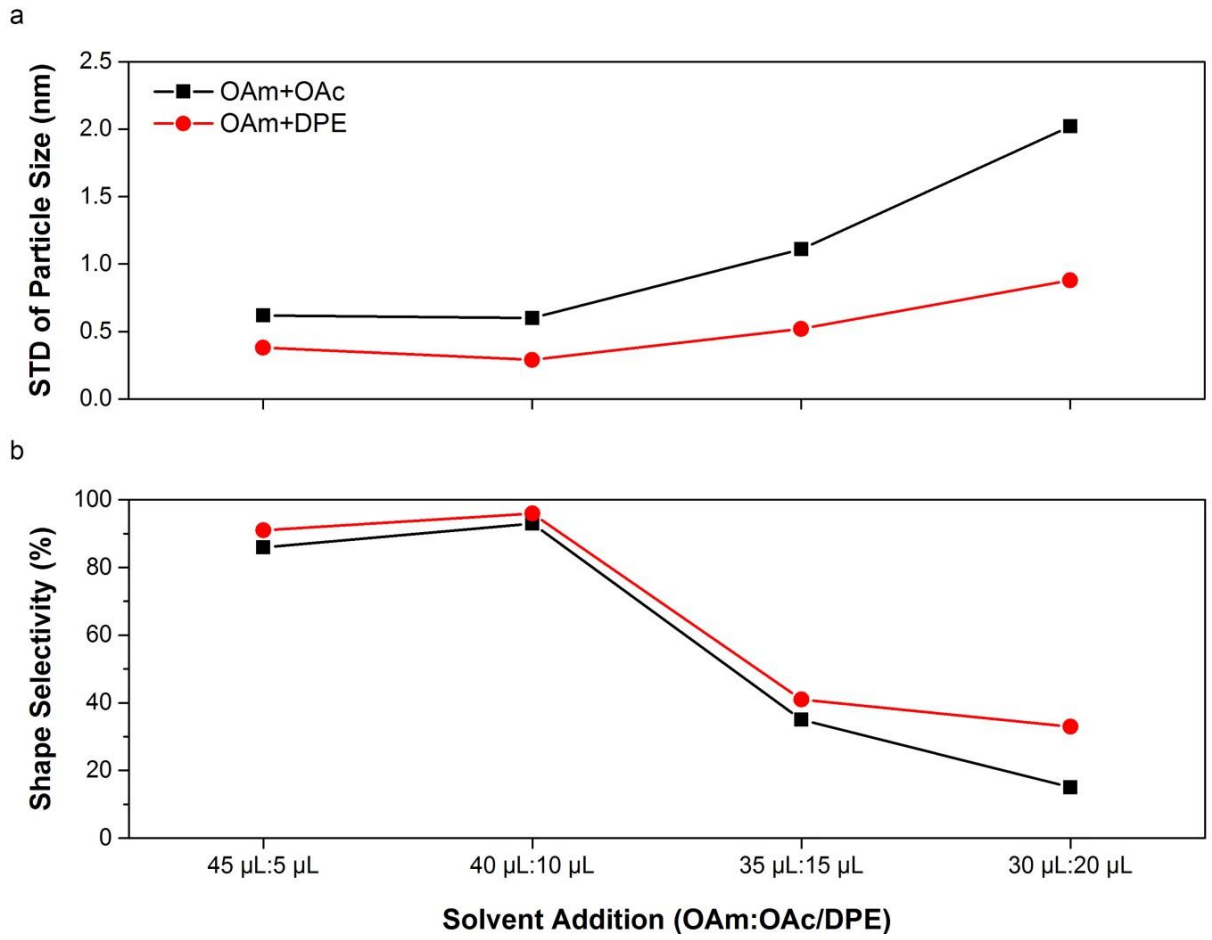

Figure 4.2 Summary of (a) standard deviation (STD) of particle size distribution and (b) percentage of cubic or octahedral structure in Figure 4.1a-h.

The XRD pattern, however, showed that the peaks for these two catalysts only slightly deviate from those of reference fcc Pt structure, indicating both nanostructures mainly consists of Pt metal (**Figure 4.3**). After applying Vegard's law on (111) plane,[41] the molar ratio of Pt to Ni in cubic and octahedral Pt-Ni/C catalysts are about 94.6 to 5.4 and 95.8 to 4.2, respectively.

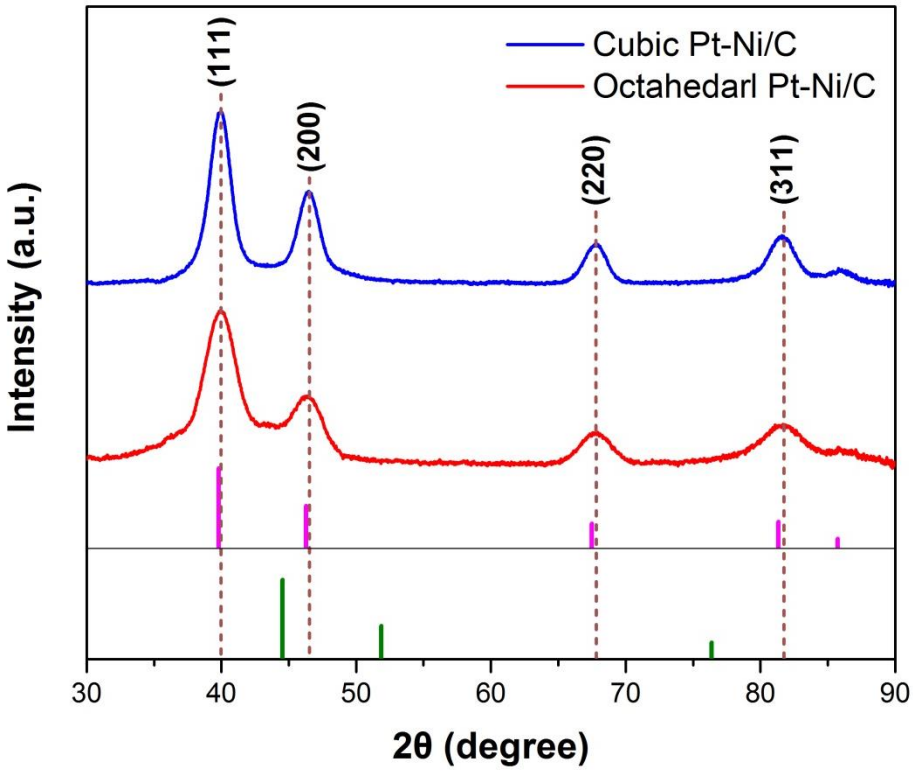

Figure 4.3 PXRD patterns of as-prepared cubic and octahedral Pt-Ni/C catalysts. Color code for the reference X-ray diffraction lines are Pt in pink and Ni in green. Molar ratio in metal precursors: Pt/Ni=3/1. Total ligand amount (OAm + OAc/DPE) is 50 μL. Reaction conditions: T_{wall} = 230 °C; reaction time = 30 min; V_{CO} = 500 mL min^{-1}.

Considering the selection of ligand did not really improve the Ni incorporation, catalyst synthesized from precursor solution with 50 μL of oleylamine as the only ligand were used to as the base material for later comparison. From **Figure 4.4**, increasing the feeding ratio of metal precursors from 3:1 to 1:1 enhanced the Ni percentage by 46%; however, this enhancement

reduced to only 6% when the feeding ratio increased from 1:1 to 1:3. On the contrary, elongating the reaction time (or slowing down the moving rate of the conveyor belt) and introducing more oleylamine into the precursor solution significantly improve Ni incorporation. For the latter, the Ni percentage in the final Pt-Ni/C catalysts increased by as high as 92% in comparison with the base material. We can thus conclude that the effect on the Ni incorporation follows the order of ligand addition > reaction >> feeding ratio. Since Ni has lower standard reduction potential than Pt,[42] it needs longer time for complete thermal decomposition reaction.[43] Although 30 min of residence time is enough for formation of well-defined Pt nanocubes, longer time or higher temperature is required for the generation of Pt-Ni nanocrystals with precise control over morphology and composition. The former is the more commonly adopted approach since higher reaction temperature usually leads to worse shape control and can sometimes results in undesired sintering. The quasi-solid-state chemistry of the conveyor transport system is another reason why Ni is harder to reduce when compared to traditional colloidal synthesis where metal precursors can move freely in the solution and easily diffuse from the bulk to the newly formed metal clusters for further particle growth process.[12, 44-46] To overcome the interaction between metal precursors and support, additional long-chain ligands that can remain liquid under high temperature reaction need to be introduced in the system. These ligands serve as a medium that facilitate the transport of metal precursors to the designated place for reaction.

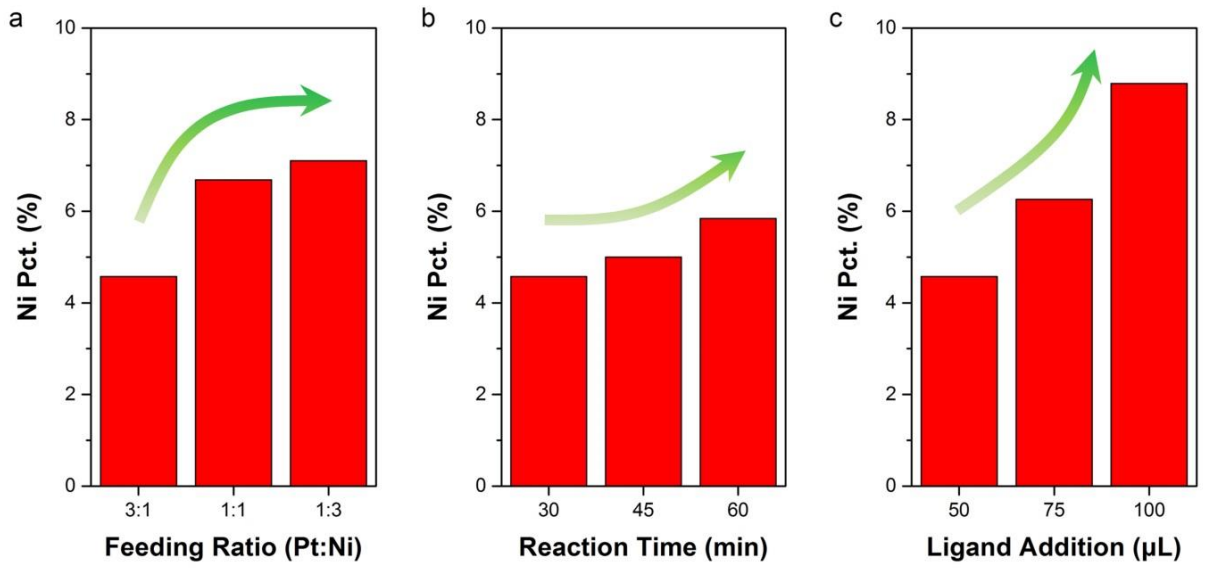

Figure 4.4 Effect of (a) feeding ratio, (b) reaction time and (c) ligand addition on Ni incorporation in Pt-Ni/C catalysts. Precursor preparation and reaction condition: (a) Oleylamine addition = 50 μL; reaction time = 30 min. (b) Feeding ratio (Pt:Ni) = 3:1; oleylamine addition = 50 μL. (c) Feeding ratio (Pt:Ni) = 3:1; reaction time = 30 min.

By increasing the reaction time to 60 min and total ligand amount to 100 μL, highly uniform and well dispersed Pt_3Ni/C with controlled geometries can be obtained under feeding ratio of Pt to Ni at around 1:1 (**Figure 4.5**). HRTEM images show the lattice distance was measured to be 0.19 nm for the cube, which is smaller than the (200) plane for the reference fcc Pt (0.196 nm) (**Figure 4.5b**). The octahedron had a lattice spacing of 0.22 nm, corresponding to the (111) plane of fcc metal alloy since the corresponding lattice for Pt is 0.227 nm (**Figure 4.5d**). The values of

these two lattice spacing were smaller than those for reference, indicating that smaller Ni atoms were incorporated into the Pt lattice. Powder X-ray diffraction (PXRD) patterns of these samples could be indexed to (111), (200), (220), and (311) diffractions of an fcc structure (**Figure 4.6**). The Ni atomic percentage is calculated to be 22.7% for cubic Pt_3Ni/C and 23.5% for octahedral one based on Vegard's Law. Moreover, all peaks are positioned in between those of Pt and Ni metals, further confirming the formation of alloy. Scanning electron microscope-energy dispersive X-ray spectrotroscopy (SEM-EDS) analysis shows that the atomic ratio between Pt and Ni was about 78:22 for the cubic nanostructure and 74:26 for the octahedral ones, close to a composition of Pt_3Ni (**Figure 4.7**).

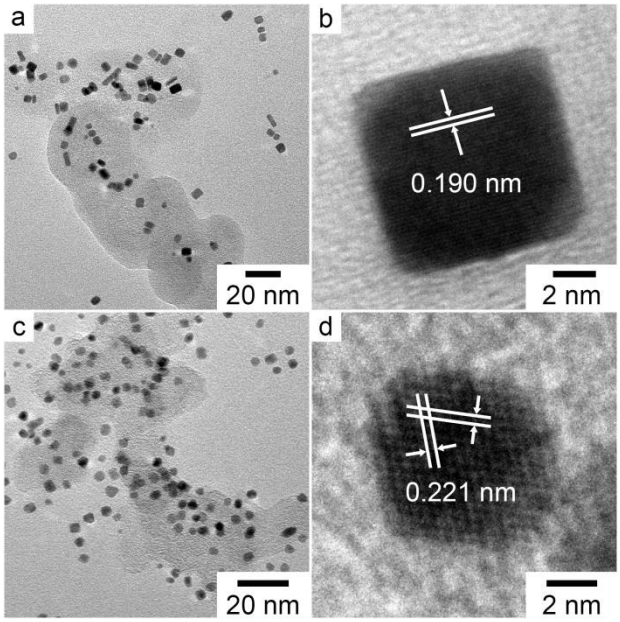

Figure 4.5 (a,c) TEM and (b,d) HRTEM micrographs of as-made (a,b) cubic and (c,d) octahedral Pt_3Ni/C catalysts.

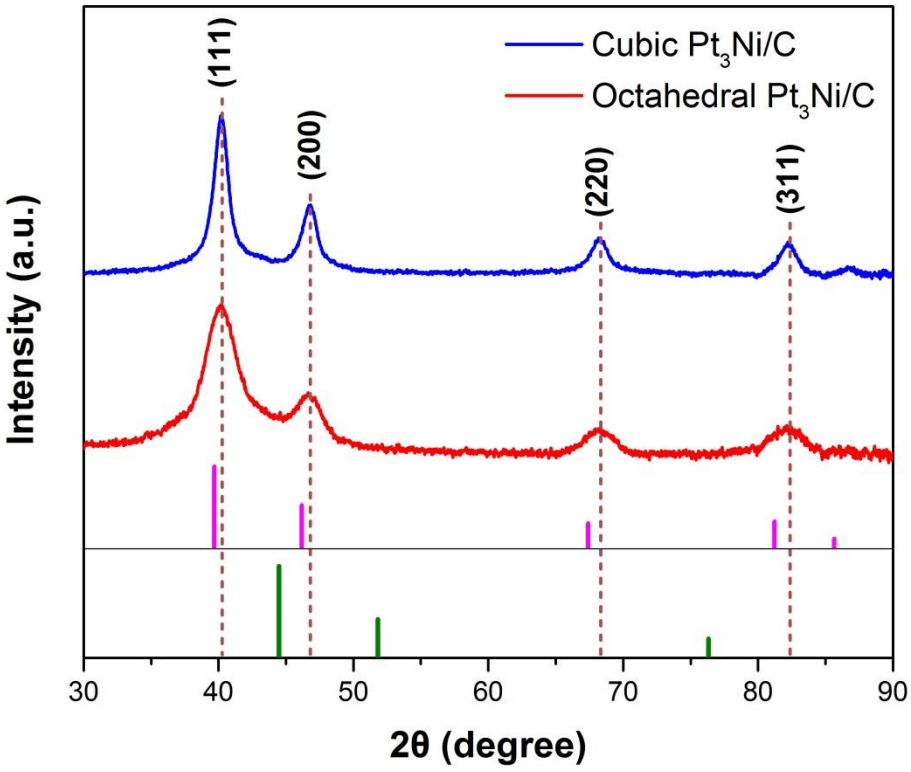

Figure 4.6 PXRD patterns of as-prepared cubic and octahedral Pt_3Ni/C catalysts. Color code for the reference X-ray diffraction lines are Pt in pink and Ni in green. Molar ratio in metal precursors: Pt/Ni=1/1. Total ligand amount (OAm + OAc/DPE) is 100 μL. Reaction conditions: T_{wall} = 230 °C; reaction time = 60 min; V_{CO} = 500 mL min^{-1}.

The similar approach can also be applied to Pt alloyed with other transition metals such as Co and Fe. **Figure 4.8** showed (HR)TEM micrographs of as-synthesized cubic and octahedral Pt_3Co/C and Pt_3Fe/C nanostructures. The composition and its alloy characteristic were further verified by XRD pattern, as provided in **Figure 4.9**.

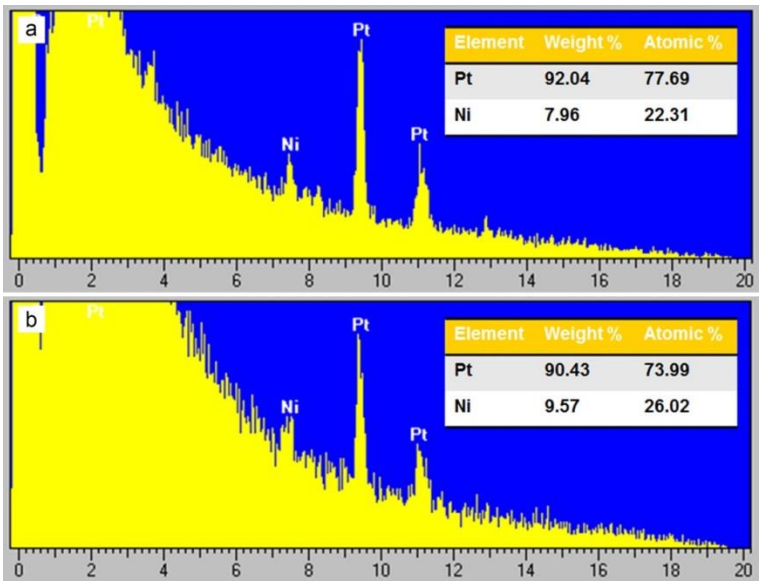

Figure 4.7 SEM-EDS spectra of as-prepared (a) cubic and (b) octahedral Pt_3Ni/C catalysts.

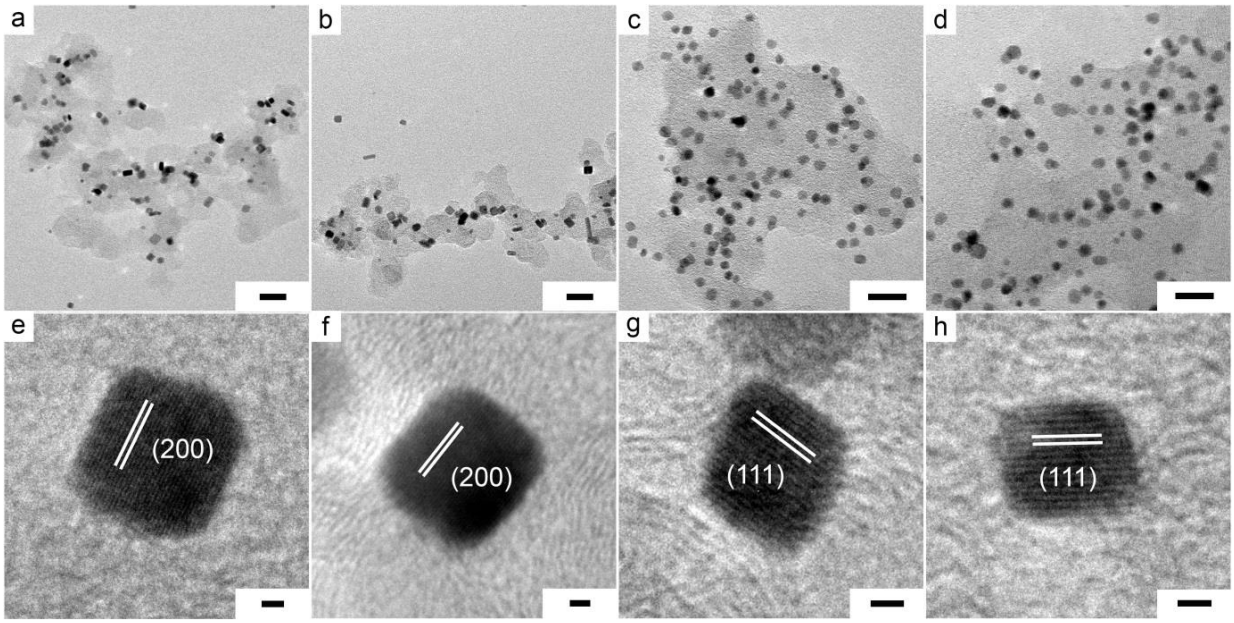

Figure 4.8 (a-d) TEM and (e-h) HRTEM micrographs of as-made (a,e) cubic Pt_3Co/C, (b,f) cubic Pt_3Fe/C, (c,g) octahedral Pt_3Fe/C and (d,h) octahedral Pt_3Fe/C catalysts. Scale bars are (a-d) 20 nm and (e-h) 1 nm.

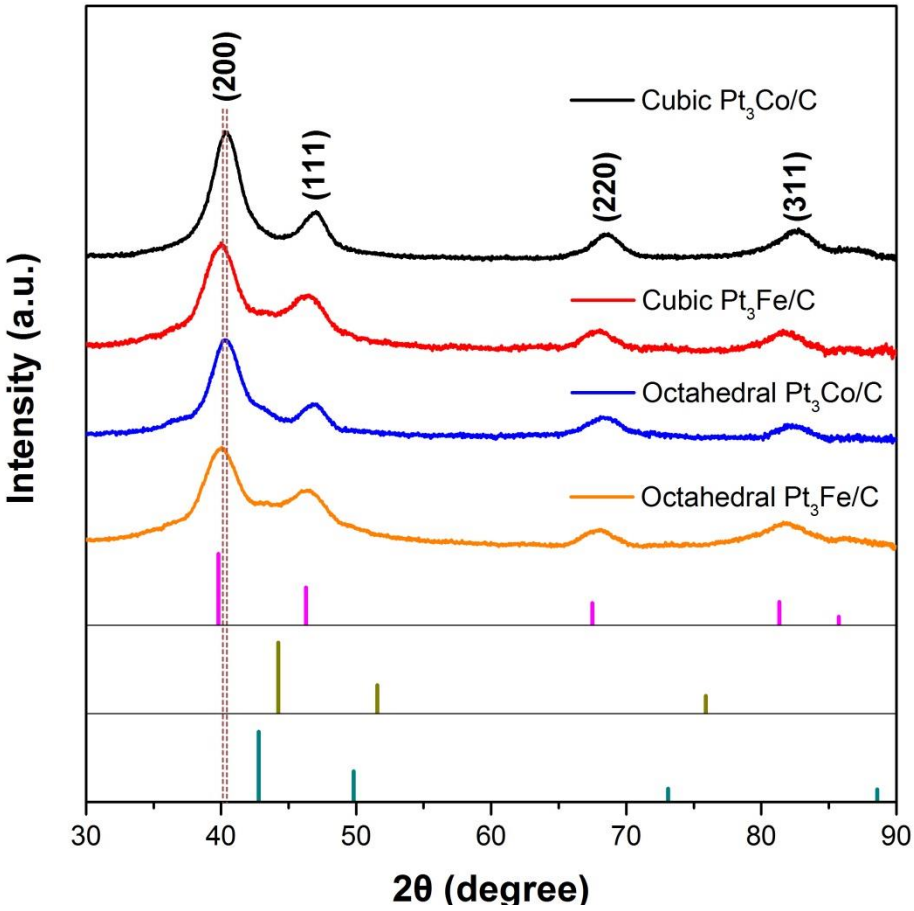

Figure 4.9 PXRD patterns of as-prepared cubic and octahedral Pt_3M/C catalysts (M = Co or Fe). Color code for the reference X-ray diffraction lines are Pt in pink, Co in brown and Fe in cyan. Molar ratio in metal precursors: Pt/M=1/1. Total ligand amount (OAm + OAc/DPE) is 100 μL. Reaction conditions: T_{wall} = 230 °C; reaction time = 60 min; V_{CO} = 500 mL min^{-1}.

4.3.2 Synthesis and characterization of carbon-supported octahedral Pt-Ni alloy using polydopamine coating technique

The previous chapter discussed how oleylamine and oleic acid can react with $Pt(acac)_2$ and $Pd(acac)_2$ to form complexes through their amine group and acid group, respectively. Considering these ligands can act as physical barriers and thus restrict the free access of reactants to active sites on the particle surface,[47-54] it will be more desirable to use surface-modified carbon support as starting material. This change can get rid of the capping ligands and provide additional metal-support interaction for high metal loading and even dispersion.[55-57]

Since scientists identifies dopamine (**Figure 4.10a**) as a new structure that mimics the adhesive protein secreted by mussel in 2007,[58] a large body of literature that utilized dopamine as a binder between metal precursors and supports has been proposed.[59-65] Dopamine can self-polymerize into polydopamine (**Figure 4.10b**) in alkaline solution and then deposit and adhere to either organic or inorganic materials.[66-67] The thickness of polydopamine layer can be controlled by varying the dopamine concentration and reaction time. Abundant amine and catechol groups are helpful for the grafting of charged metal complexes and are beneficial for the anchoring and dispersion of these nanoparticles. Furthermore, the hydrophilicity of polydopamine also makes it suitable for fuel cell application due to high proton conductivity.

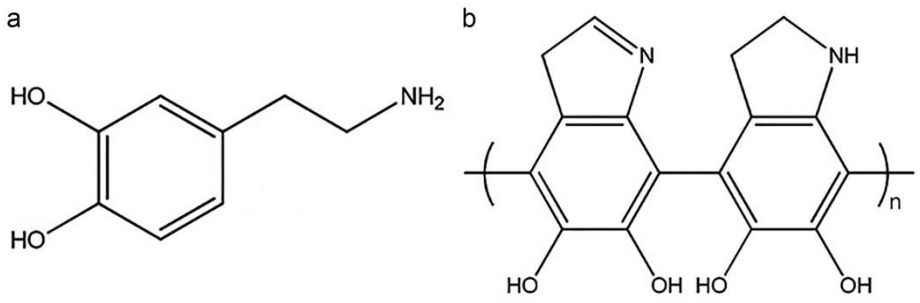

Figure 4.10 Structure of (a) dopamine (DA) and (b) polydopamine (PDA).

The aforementioned reaction all occurred in mild conditions, where the precursor solutions were stirred under air at less than 100 °C for several hours. The generated particles have no specific morphology due to the absence of shape-directing agent, and the reacted solution has to be centrifuged and washed thoroughly afterwards in order to get the final product. To combine the polydopamine coating technique with conveyor transport system, the as-made polydopamine-coated carbon black (PDA-C) was mixed with metal precursors and ethanol and then sprayed onto the preheated belt to evaporate the solvent. The precursor deposit was transferred into reactor for thermal decomposition reaction under hot CO environment. Owing to the hydrophilicity of polydopamine, metal chlorides instead of metal acetylactoneates were used as metal precursors for better dispersion. By using CO gas as growth inhibitor and polydopamine as binding agent, well-dispersed and shape-selective metal nanoaprticles on carbon support can be formed in the absence of any long-chain ligand, as illustrated in **Figure 4.11**.

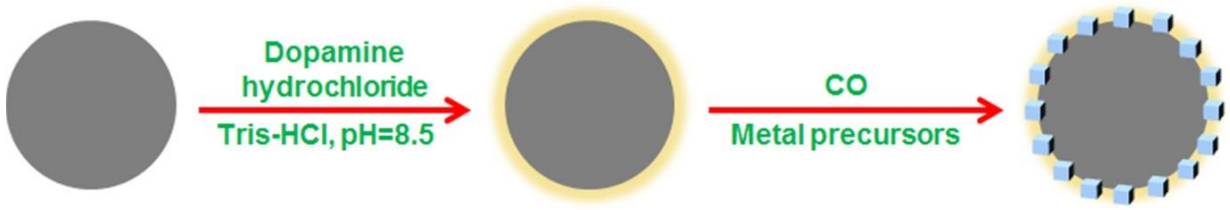

Figure 4.11 Synthesis route for shape-controlled catalyst using PDA coating technique.

Highly uniform carbon-supported Pt nanocubes with narrow size distribution and good metal dispersion can be continuously generated when H_2PtCl_6 was introduced as metal precursor (**Figure 4.12a**). The lattice spacing of as-made Pt nanoparticulates also matched well to reference fcc Pt nanostructure (**Figure 4.12b**). When $NiCl_2 \cdot 6H_2O$ was added into precursor solution along with H_2PtCl_6, octahedral Pt_3Ni/C was obtained, and its alloy characteristic and composition were both confirmed by XRD and EDS analysis (**Figure 4.12c**). The well-defined geometry and sharp edges were observed in HRTEM micrograph, and the interfringe distance of the particle was calculated to be 0.222 nm, slightly smaller than that of reference fcc Pt(111) plane, an indirect evidence of successful Ni incorporation (**Figure 4.12d**). The metal loading drastically decreased when H_2PtCl_6 was replaced with $Pt(acac)_2$, which can be attributed to the intrinsic hydrophilicity of polydopamine, and this explain why the as-synthesized PDA-C disperse well in ethanol but not chloroform. The presence of cubic structure in the product also confirmed that CO does act as the major shape-directing agent during the reaction (**Figure 4.13**).

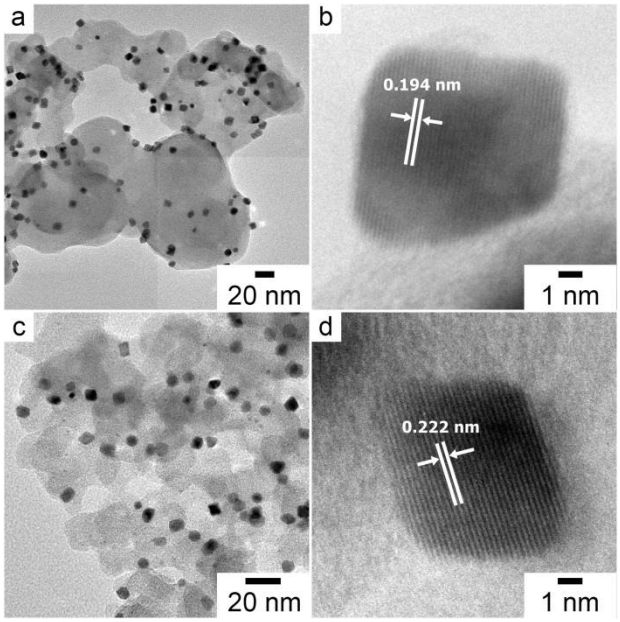

Figure 4.12 (a,c) TEM and (b,d) HRTEM micrographs of as-made (a,b) cubic Pt/PDA-C and (c,d) octahedral Pt_3Ni/PDA-C catalysts.

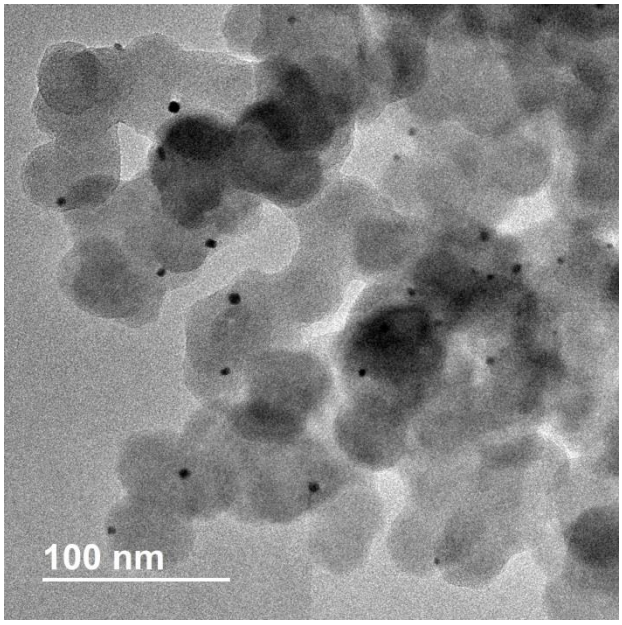

Figure 4.13 TEM micrograph of Pt/PDA-C when $Pt(acac)_2$ was used as metal precursor.

The composition-dependent morphology change could be associated with different CO adsorption to the two metals. Both experimental and theoretical studies suggest that CO molecules adsorb preferentially to (100) planes for Pt but to (111) for Ni, thus altering the growth rate of surface planes and therefore the resultant particle geometry.[37, 68] Therefore, Pt-Ni tends to grow into octahedrons when Ni content is sufficiently high to dominate the CO adsorption, and pure Pt tends to grow into cubes under hot CO environment. In comparison to those synthesized by conventional impregnation-reduction method,[69] the as-made carbon-supported Pt and Pt-Ni catalyst have much higher shape uniformity and narrower size distribution, which can result from strong interaction between polydopamine and metal precursors due to the abundance of amine and catechol groups.

TGA was carried out to have a better understanding of polydopamine removal. Under air atmosphere, the weight of PDA-C started to gradually decrease at around 200 °C due to the decomposition of polydopamine.[65] The rapid weight loss starting at 400 °C is mainly due to carbon burn-out, and the rate of weight loss reached maximum at 474 °C and decrease to zero when PDA-C was decomposed completely (**Figure 4.14a**). If the whole process was switched to a N_2 environment, PDA-C will be converted to N-doped carbon at around 700 °C through carbonization.[70-72] The PDA-derived N-doped carbon material is electrical conductive and permeable to reactant molecules, and the incorporated nitrogen atoms can generate plenty of

defects and withdraw electrons from carbon atoms due to its high electronegativity to form active site for O_2 adsorption and reduction, leading to high electrocatalytic performances in fuel cell applications. N-doped carbon is also a promising material for non-precious metal catalyst.[73-74]

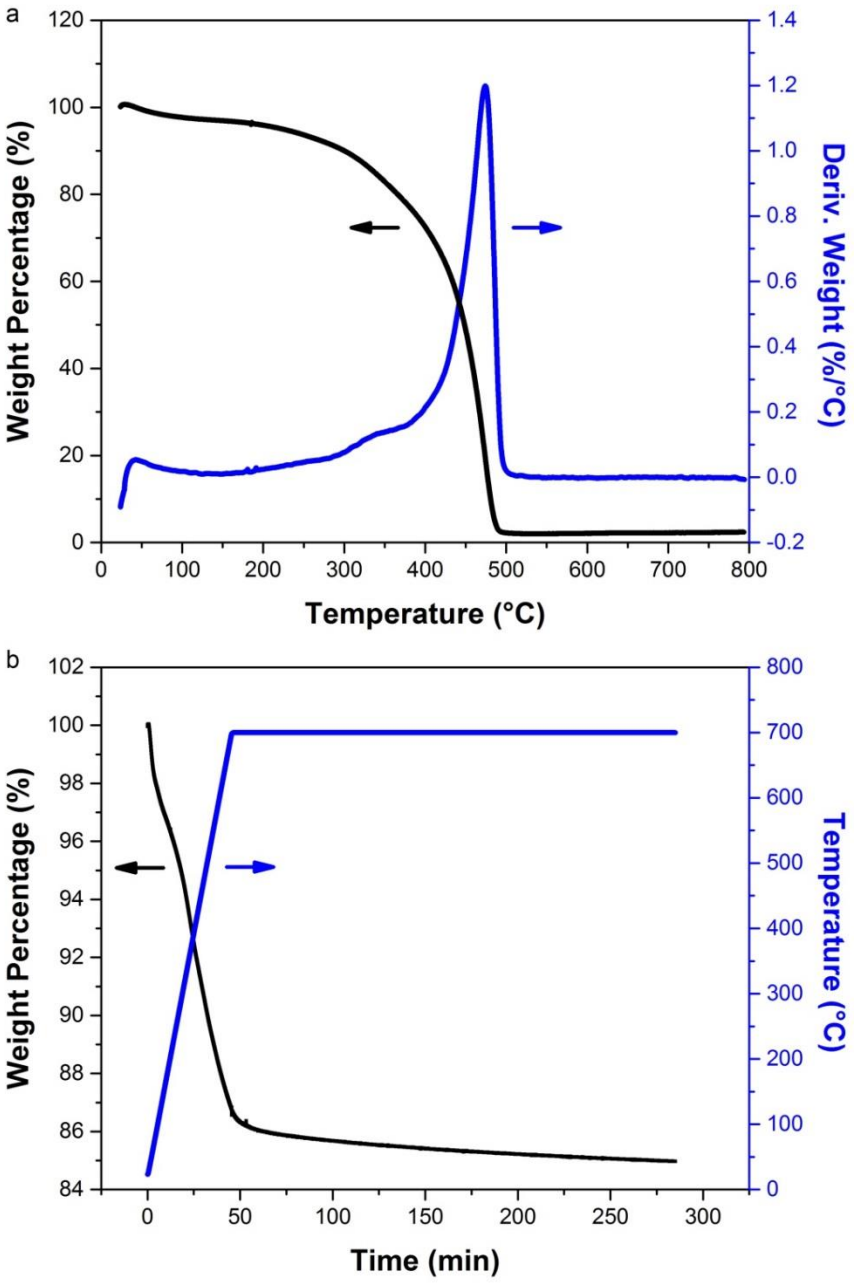

Figure 4.14 TGA curves for PDA-C under (a) air and (b) N_2 atmosphere.

When as-made Pt_3Ni/C was heated under air at 200 °C for 2 hr, the PDA started to decompose and the particles also retained their well-defined octahedral shape, which was expected since the reaction temperature was even higher than the thermal annealing temperature (**Figure 4.15a**). If the temperature increased to 400 °C, carbon support was burned out, and severe aggregation of Pt_3Ni nanoparticles occurred, while they still remain initial octahedral morphology (**Figure 4.15b**). On the contrary, if the catalyst was switched to an N_2 atmosphere and underwent thermal annealing at 700 for 2 h, sintering began to take place and the particles can no longer maintain their original geometry (**Figure 4.15c**), though more stable and active intermetallic form could be formed under this condition and thus enhance their electrocatalytic performances.[71, 75]

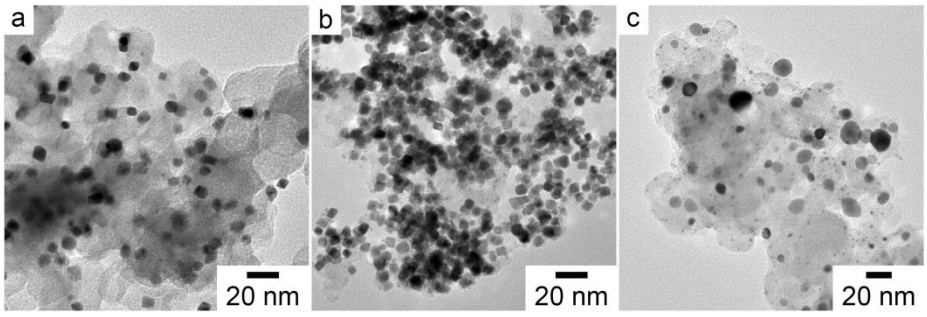

Figure 4.15 TEM micrographs of Pt3Ni/PDA-C after thermally annealed under (a) air at 200 °C for 2 h, (b) air at 400 °C for 2 h and (c) N_2 at 700 °C for 2 h.

4.4 Conclusion

The conveyor transport system has been successfully used to make a range of carbon-supported cubic and octahedral Pt alloy nanocatalysts with controlled shape and composition by carefully adjusting the precursor feeding ratio, capping agent amount and reaction time. CO acts as both gas reductant and growth inhibitor for making precision-controlled metal alloy nanocrystals because of its excellent selectivity in the adsorption on metal surfaces. This approach can also be combined with PDA coating technique to generate monodisperse cubic Pt/C and octahedral Pt_3Ni/C, and PDA can be removed later by applying thermal annealing process of as-made catalysts.

4.5 References

1. Stephens, I. E. L.; Bondarenko, A. S.; Gronbjerg, U.; Rossmeisl, J.; Chorkendorff, I. *Energy Environ. Sci.* **2012**, *5*, 6744-6762.

2. Mistry, H.; Varela, A. S.; Kuhl, S.; Strasser, P.; Cuenya, B. R. *Nat. Rev. Mater.* **2016**, *1*.

3. Chen, A. C.; Holt-Hindle, P. *Chem. Rev.* **2010**, *110*, 3767-3804.

4. Wang, Y. J.; Zhao, N. N.; Fang, B. Z.; Li, H.; Bi, X. T. T.; Wang, H. J. *Chem. Rev.* **2015**, *115*, 3433-3467.

5. Bing, Y. H.; Liu, H. S.; Zhang, L.; Ghosh, D.; Zhang, J. J. *Chem. Soc. Rev.* **2010**, *39*, 2184-2202.

6. Markovic, N. M.; Schmidt, T. J.; Stamenkovic, V.; Ross, P. N. *Fuel Cells* **2001**, *1*, 105-116.

7. Han, B. H.; Carlton, C. E.; Suntivich, J.; Xu, Z. C.; Shao-Horn, Y. *J. Phys. Chem. C* **2015**, *119*, 3971-3978.

8. Stamenkovic, V. R.; Mun, B. S.; Arenz, M.; Mayrhofer, K. J. J.; Lucas, C. A.; Wang, G. F.; Ross, P. N.; Markovic, N. M. *Nat. Mater.* **2007**, *6*, 241-247.

9. Strasser, P. *Science* **2015**, *349*, 379-380.

10. Stamenkovic, V. R.; Fowler, B.; Mun, B. S.; Wang, G. F.; Ross, P. N.; Lucas, C. A.;

Markovic, N. M. *Science* **2007**, *315*, 493-497.

11. Zhang, J.; Yang, H. Z.; Fang, J. Y.; Zou, S. Z. *Nano Lett.* **2010**, *10*, 638-644.

12. Wu, J.; Gross, A.; Yang, H. *Nano Lett.* **2011**, *11*, 798-802.

13. Wu, J.; Qi, L.; You, H.; Gross, A.; Li, J.; Yang, H. **2012**, *134*, 11880-11883.

14. Wu, J. B.; Zhang, J. L.; Peng, Z. M.; Yang, S. C.; Wagner, F. T.; Yang, H. *J. Am. Chem. Soc.* **2010**, *132*, 4984-4985.

15. Choi, S. I.; Xie, S. F.; Shao, M. H.; Odell, J. H.; Lu, N.; Peng, H. C.; Protsailo, L.; Guerrero, S.; Park, J. H.; Xia, X. H.; Wang, J. G.; Kim, M. J.; Xia, Y. N. *Nano Lett.* **2013**, *13*, 3420-3425.

16. Cui, C. H.; Gan, L.; Li, H. H.; Yu, S. H.; Heggen, M.; Strasser, P. *Nano Lett.* **2012**, *12*, 5885-5889.

17. Zhang, N.; Tsao, K. C.; Pan, Y. T.; Yang, H. *Nanoscale* **2016**, *8*, 2548-2553.

18. Zhang, N.; Du, L.; Du, C. Y.; Yin, G. P. *RSC Adv.* **2016**, *6*, 26323-26328.

19. Huang, X. Q.; Zhao, Z. P.; Chen, Y.; Zhu, E. B.; Li, M. F.; Duan, X. F.; Huang, Y. *Energy Environ. Sci.* **2014**, *7*, 2957-2962.

20. Huang, X. Q.; Zhao, Z. P.; Cao, L.; Chen, Y.; Zhu, E. B.; Lin, Z. Y.; Li, M. F.; Yan, A. M.;

Zettl, A.; Wang, Y. M.; Duan, X. F.; Mueller, T.; Huang, Y. *Science* **2015**, *348*, 1230-1234.

21. Greeley, J.; Stephens, I. E. L.; Bondarenko, A. S.; Johansson, T. P.; Hansen, H. A.; Jaramillo, T. F.; Rossmeisl, J.; Chorkendorff, I.; Norskov, J. K. *Nat. Chem.* **2009**, *1*, 552-556.

22. Mayrhofer, K. J. J.; Arenz, M. *Nat. Chem.* **2009**, *1*, 518-519.

23. Yoo, S. J.; Sung, Y. E. *Surf. Sci.* **2015**, *631*, 272-277.

24. Yoo, S. J.; Lee, K. S.; Hwang, S. J.; Cho, Y. H.; Kim, S. K.; Yun, J. W.; Sung, Y. E.; Lim, T. H. *Int. J. Hydrog. Energy* **2012**, *37*, 9758-9765.

25. Yoo, S. J.; Kim, S. K.; Jeon, T. Y.; Hwang, S. J.; Lee, J. G.; Lee, S. C.; Lee, K. S.; Cho, Y. H.; Sung, Y. E.; Lim, T. H. *Chem. Commun.* **2011**, *47*, 11414-11416.

26. Hwang, S. J.; Kim, S. K.; Lee, J. G.; Lee, S. C.; Jang, J. H.; Kim, P.; Lim, T. H.; Sung, Y. E.; Yoo, S. J. *J. Am. Chem. Soc.* **2012**, *134*, 19508-19511.

27. Malacrida, P.; Escudero-Escribano, M.; Verdaguer-Casadevall, A.; Stephens, I. E. L.; Chorkendorff, I. *J. Mater. Chem. A* **2014**, *2*, 4234-4243.

28. Johansson, T. P.; Ulrikkeholm, E. T.; Hernandez-Fernandez, P.; Escudero-Escribano, M.; Malacrida, P.; Stephens, I. E. L.; Chorkendorff, I. *Phys. Chem. Chem. Phys.* **2014**, *16*, 13718-13725.

29. Hernandez-Fernandez, P.; Masini, F.; McCarthy, D. N.; Strebel, C. E.; Friebel, D.; Deiana, D.; Malacrida, P.; Nierhoff, A.; Bodin, A.; Wise, A. M.; Nielsen, J. H.; Hansen, T. W.; Nilsson, A.; Stephens, I. E. L.; Chorkendorff, I. *Nat. Chem.* **2014**, *6*, 732-738.

30. Escudero-Escribano, M.; Verdaguer-Casadevall, A.; Malacrida, P.; Gronbjerg, U.; Knudsen, B. P.; Jepsen, A. K.; Rossmeisl, J.; Stephens, I. E. L.; Chorkendorff, I. *J. Am. Chem. Soc.* **2012**, *134*, 16476-16479.

31. Escudero-Escribano, M.; Malacrida, P.; Hansen, M. H.; Vej-Hansen, U. G.; Velazquez-Palenzuela, A.; Tripkovic, V.; Schiotz, J.; Rossmeisl, J.; Stephens, I. E. L.; Chorkendorff, I. *Science* **2016**, *352*, 73-76.

32. Jeon, M. K.; McGinn, P. J. *J. Power Sources* **2011**, *196*, 1127-1131.

33. Brandiele, R.; Durante, C.; Gradzka, E.; Rizzi, G. A.; Zheng, J.; Badocco, D.; Centomo, P.; Pastore, P.; Granozzi, G.; Gennaro, A. *J. Mater. Chem. A* **2016**, *4*, 12232-12240.

34. Sung, S. S.; Hoffmann, R. *J. Am. Chem. Soc.* **1985**, *107*, 578-584.

35. Wong, Y. T.; Hoffmann, R. *J. Phys. Chem.* **1991**, *95*, 859-867.

36. Hammer, B.; Morikawa, Y.; Norskov, J. K. *Phys. Rev. Lett.* **1996**, *76*, 2141-2144.

37. Morikawa, Y.; Mortensen, J. J.; Hammer, B.; Norskov, J. K. *Surf. Sci.* **1997**, *386*, 67-72.

38. Eichler, A. *Surf. Sci.* **2002**, *498*, 314-320.

39. Hwang, S. Y.; Zhang, M.; Zhang, C.; Ma, B.; Zheng, J.; Peng, Z. *Chem. Commun.* **2014**, *50*, 14013-14016.

40. Tsao, K. C.; Yang, H. *Small* **2016**, *12*, 4808-4814.

41. Denton, A. R.; Ashcroft, N. W. *Phys. Rev. A* **1991**, *43*, 3161-3164.

42. Haynes, W. M.; Lide, D. R.; Bruno, T. J. *CRC handbook of chemistry and physics* **2015**, Boca Raton, Florida: CRC Press.

43. Ahrenstorf, K.; Heller, H.; Kornowski, A.; Broekaert, J. A. C.; Weller, H. *Adv. Funct. Mater.* **2008**, *18*, 3850-3856.

44. You, H.; Yang, S.; Ding, B.; Yang, H. *Chem. Soc. Rev.* **2013**, *42*, 2880-2904.

45. Kwon, S. G.; Hyeon, T. *Acc. Chem. Res.* **2008**, *41*, 1696-1709.

46. Gu, J.; Zhang, Y.-W.; Tao, F. *Chem. Soc. Rev.* **2012**, *41*, 8050-8065.

47. You, H. J.; Wang, W. J.; Yang, S. C. *ACS Appl. Mater. Interfaces* **2014**, *6*, 19035-19040.

48. Yang, H. Z.; Tang, Y. G.; Zou, S. Z. *Electrochem. Commun.* **2014**, *38*, 134-137.

49. Naresh, N.; Wasim, F. G. S.; Ladewig, B. P.; Neergat, M. *J. Mater. Chem. A* **2013**, *1*, 8553-8559.

50. Luo, M. H.; Hong, Y. C.; Yao, W. F.; Huang, C. P.; Xu, Q. J.; Wu, Q. *J. Mater. Chem. A* **2015**, *3*, 2770-2775.

51. Li, D. G.; Wang, C.; Tripkovic, D.; Sun, S. H.; Markovic, N. M.; Stamenkovic, V. R. *ACS Catal.* **2012**, *2*, 1358-1362.

52. Cargnello, M.; Chen, C.; Diroll, B. T.; Doan-Nguyen, V. V. T.; Gorte, R. J.; Murray, C. B. *J. Am. Chem. Soc.* **2015**, *137*, 6906-6911.

53. Aran-Ais, R. M.; Vidal-Iglesias, F. J.; Solla-Gullon, J.; Herrero, E.; Feliu, J. M. *Electroanalysis* **2015**, *27*, 945-956.

54. Niu, Z. Q.; Li, Y. D. *Chem. Mat.* **2014**, *26*, 72-83.

55. Kannan, R.; Pillai, V. K. in *Surface Modification of Nanotube Fillers* **2011**, Boschstrasse, Weinheim: Wiley-VCH Verlag GmbH & Co. KGaA, 135-158.

56. Zhu, J.; Kim, J. D.; Peng, H. Q.; Margrave, J. L.; Khabashesku, V. N.; Barrera, E. V. *Nano Lett.* **2003**, *3*, 1107-1113.

57. Ramanathan, T.; Fisher, F. T.; Ruoff, R. S.; Brinson, L. C. *Chem. Mat.* **2005**, *17*, 1290-1295.

58. Lee, H.; Dellatore, S. M.; Miller, W. M.; Messersmith, P. B. *Science* **2007**, *318*, 426-430.

59. Zhang, L.; Wu, J. J.; Wang, Y. X.; Long, Y. H.; Zhao, N.; Xu, J. *J. Am. Chem. Soc.* **2012**,

134, 9879-9881.

60. Yu, X. Q.; Wang, H.; Guo, L. P.; Wang, L. *Chem.-Asian J.* **2014**, *9*, 3221-3227.

61. Long, H. T.; Del Frari, D.; Martin, A.; Didierjean, J.; Ball, V.; Michel, M.; El Ahrach, H. I. *J. Power Sources* **2016**, *307*, 569-577.

62. Liu, X. C.; Wang, G. C.; Liang, R. P.; Shi, L.; Qiu, J. D. *J. Mater. Chem. A* **2013**, *1*, 3945-3953.

63. Liu, R.; Guo, Y. L.; Odusote, G.; Qu, F. L.; Priestley, R. D. *ACS Appl. Mater. Interfaces* **2013**, *5*, 9167-9171.

64. Huang, H. L.; He, Z. Y.; Lin, X. M.; Ruan, W. S.; Liu, Y. J.; Yang, Z. H. *Appl. Catal. A-Gen.* **2015**, *490*, 65-70.

65. Fei, B.; Qian, B. T.; Yang, Z. Y.; Wang, R. H.; Liu, W. C.; Mak, C. L.; Xin, J. H. *Carbon* **2008**, *46*, 1795-1797.

66. Liu, Y. L.; Ai, K. L.; Lu, L. H. *Chem. Rev.* **2014**, *114*, 5057-5115.

67. Liebscher, J.; Mrowczynski, R.; Scheidt, H. A.; Filip, C.; Hadade, N. D.; Turcu, R.; Bende, A.; Beck, S. *Langmuir* **2013**, *29*, 10539-10548.

68. Palaikis, L.; Zurawski, D.; Hourani, M.; Wieckowski, A. *Surf. Sci* **1988**, *199*, 183-198.

69. Zhang, C.; Hwang, S. Y.; Trout, A.; Peng, Z. *J. Am. Chem. Soc.* **2014**, *136*, 7805-7808.

70. Zhang, C. L.; Li, H. S.; Ping, N.; Pang, G.; Xu, G. Y.; Zhang, X. G. *RSC Adv.* **2014**, *4*, 38791-38796.

71. Chung, D. Y.; Jun, S. W.; Yoon, G.; Kwon, S. G.; Shin, D. Y.; Seo, P.; Yoo, J. M.; Shin, H.; Chung, Y. H.; Kim, H.; Mun, B. S.; Lee, K. S.; Lee, N. S.; Yoo, S. J.; Lim, D. H.; Kang, K.; Sung, Y. E.; Hyeon, T. *J. Am. Chem. Soc.* **2015**, *137*, 15478-15485.

72. Liang, J.; Xiao, C. H.; Chen, X.; Gao, R. X.; Ding, S. J. *Nanotechnology* **2016**, *27*.

73. Chen, Z. W.; Higgins, D.; Yu, A. P.; Zhang, L.; Zhang, J. J. *Energy Environ. Sci.* **2011**, *4*, 3167-3192.

74. Dai, L. M.; Xue, Y. H.; Qu, L. T.; Choi, H. J.; Baek, J. B. *Chem. Rev.* **2015**, *115*, 4823-4892.

75. Wang, D. L.; Xin, H. L. L.; Hovden, R.; Wang, H. S.; Yu, Y. C.; Muller, D. A.; DiSalvo, F. J.; Abruna, H. D. *Nat. Mater.* **2013**, *12*, 81-87.

Chapter 5:

Synthesis of Supported and Shaped Bimetallic Core-Sell Nanocatalysts Using Conveyor Transport System

5.1 Introduction

For heterogeneous catalysis, only surface atoms participate in the reaction. As mentioned in previous chapters, Pt-based catalysts are important for a wide variety of reactions. In addition to alloying Pt with other transition metals, efficient utilization of Pt can also be achieved by designing core-shell nanostructure with Pt as the shell layer. A great deal of attention has been paid to the catalysts with either Pt skin or skeleton surface.[1-2] In principle, surface segregation happens in order to reduce the surface free energy, and can be affected by several parameters including particle size, temperature, adsorbate and substrate.[3] Core-shell nanostructured catalysts are mainly synthesized through three methods: colloidal synthetic approach,[4] electrochemical approach,[5-7] and reaction-driven approach.[8-10]

In colloidal synthetic approach, different core materials are synthesized first, followed by dissolving Pt precursors that are subsequently reduced and deposited onto the cores. Peng et al. synthesized a series of M@Pt (M=Ag, Au, Cu, Pd) core-shell nanostructures, though most of them are in island or island-on-layer form.[11-12] Xia's group reported that well-defined octahedral

Pd@Pt-Ni and icosahedral Pd@Pt could enhance the specific area activity by 14- and 7.8-fold relative to commercial Pt catalyst, respectively.[13-14] Wu et al. showed Pt_3Ni@Pt_3Pd core-shell nanostructures were more active and stable towards ORR than the single bimetallic system.[15]

De-alloying and UPD are two effective electrochemical methods for producing high-performance ORR catalysts. Adzic group developed the Cu-mediated deposition approach, demonstrating that the core-shell nanostructures with Pt monolayers are more cost-effective and active than the conventional Pt-based catalysts.[6, 16-23] Strasser group extensively studied the de-alloying of Pt-Co and Pt-Ni nanoparticles under acidic conditions, and the ORR activity was enhanced due to the compressive strain in the surface Pt atoms.[7, 24-32] Shao et al. combined UPD and the de-alloying processes to create a core-shell nanostructure with porous Pd-Cu or Pd-Ni as the core and Pt layer as the shell.[33-34]

Furthermore, alloy nanostructures can be tuned by reacting gases in the environment since different gas molecules and surface metals can have different binding energies, resulting in the enrichment of selected metal on the particle surface, a process known as adsorbate-induced segregation. Mayrhofer et al. found that CO-annealed Pt_3Co/C catalysts exhibit improved ORR activity in both acidic and alkaline media in comparison to untreated, chemically-leached ones. Chung et al. showed that by exposing the as-made PtNi/C catalyst to H_2/Ar at elevated

temperatures, the newly formed Pt(111) shell significantly improved the ORR performance.[35] Abruna and his co-workers adopted this approach to synthesize Pt-Co nanocatalysts consisting of highly ordered intermetallic cores with thin Pt shells after H_2 treatment. The electrocatalyst exhibited 3- and 2-fold enhancements in specific and mass activity, respectively, relative to disordered Pt_3Co alloy nanostructures.[10]

By thermally annealing the as-prepared catalysts under inert Ar atmonsphere, Huang's group showed that the Pt_3Ni nanoframes/C with Pt-skin-terminated (111) surface structure have improved ORR activity than its solid octahedral counterparts,[36] and the same approach can also be applied to Pt-Cu system.[37] Pan et al. combined the thermal annealing with electrochemical de-alloying processes to induce the formation of a Pt shell, and the treated Pt-Ni/C electrocatalyst showed enhanced ORR activity when compared to the original carbon-supported sandwich-like Pt-Ni/C nanostructure.[38]

This chapter discusses the complexation reaction, together with the newly developed conveyor transport system, to continuously generate a range of uniform carbon-supported core-shell nanostructures. This technique is the first one-step process that can synthesize supported core-shell catalysts without applying subsequent hot injections, electrochemical de-alloying or thermal annealing approaches.

5.2 Experimental

5.2.1 Chemical and materials

Platinum acetylacetonate ($Pt(acac)_2$, Strem Chemicals, 98%); palladium acetylacetonate ($Pd(acac)_2$, Strem Chemicals, 99%); gold(III) chloride trihydrate ($AuCl{\cdot}3H_2O$, Sigma-Aldrich, >99.9%); oleylamine (OAm, Sigma-Aldrich, 70%); oleic acid (OAc, Sigma-Aldrich, 90%); chloroform (Fisher Chemical, >99%); ethanol (Decon Labs, 200 proof); carbon black (Vulcan XC-72, Cabot); commercial Pt/C (BASF, 20%); commercial Pd/C (Sigma-Aldrich, 10%); carbon monoxide (CO, research grade, Airgas); argon (Ar, UHP grade, Airgas); nitrogen (N_2, UHP grade, Airgas). All were used as received.

5.2.2 Synthesis of carbon-supported truncated octahedral Pd@Pt core-shell nanostructures

After synthesizing Pd/C (refer to Chapter 2 for synthesis procedures), instead of collecting the products, the conveyor belt kept moving in the same speed for the second deposition and thermal decomposition processes. 2.6 mg, 3.9 mg, and 7.8 mg of $Pt(acac)_2$ were used to synthesize $Pd_{86}@Pt_{14}/C$, $Pd_{80}@Pt_{20}/C$, and $Pd_{67}@Pt_{33}/C$ catalysts, respectively. Certain amount of $Pt(acac)_2$ and 50 μL of OAm were mixed with 5 mL of chloroform in a glass vial and sonicated for 30 sec to form a well-diepersed Pt precurosr solution. The precursor solution then

was used to fill the container of an airbrush, followed by spraying onto a cover glass slide deposited with as-made Pd/C on the conveyor belt, which was preheated to 120 °C. The cover glass slide deposted with precursors was then transferred into the tubular reactor filled with CO/N_2 (mixture of 350 mL of CO and 150 mL of N_2) to undergo thermal decomposition reaction, and the moving rate of the belt was adjusted so the residence time of the precursor in the heating zone is 30 min, corresponding to the moving rate of 1.06 cm min^{-1} for the conveyor belt. Wall temperature of the tubular reactor was maintained at 210 °C by the heating tape. After the reaction, the products on the cover glass slide can be easily collected by scratching with a spatula or rinsing with chloroform.

5.2.3 Synthesis of carbon-supported cubic Pt@Au core-shell nanostructures

After synthesizing Pt/C (refer to Chapter 2 for synthesis procedures), instead of collecting the products, the conveyor belt kept moving in the same speed for the second deposition and thermal decomposition processes. 2 mg of $AuCl_3 \cdot 3H_2O$ was mixed with 5 mL of ethanol in a glass vial and sonicated for 30 sec to form a well-diepersed Au precurosr solution. The remaining procedures were the same as those for the synthesis of truncated octahedral Pd@Pt/C core-shell nanostructures, except that the hot plate temperature was reduce to 80 °C.

5.2.4 Electrochemical measurements

A three-electrode cell system was used to conduct CO stripping voltammetry. The working electrode was a glassy-carbon rotating disk electrode (RDE) with an area of 0.196 cm^2. A platinum foil of 1 cm^2 was used as the counter electrode with a HydroFlex hydrogen electrode in a separate compartment as reference eletrode. The as-prepared core-shell catalyst was mixed with 10 mL of AA and then stirred for 2 h at 70 °C. To make a catalyst ink, 3 mg of as-prepared Pd@Pt/C, commercial BASF Pt/C, or commercial Sigma-Aldrich Pd/C catalysts was added in a mixture of 4 mL of deionized water, 1 mL of isopropanol, and 25 μL of 5% Nafion. A small volume of this catalyst ink (40 μL) was drop cast on top of the RDE to make the working electrode. First, the RDE was immersed in an CO-saturated, aqueous solution of perchloric acid ($HClO_4$, 0.1 M , prepared with Millipore water, 18.2 MΩ at 25 °C) for 15 min. After that, the RDE was quickly transferred to another flask filled with Ar-saturated, aqueous solution of perchloric acid ($HClO_4$, 0.1 M , prepared with Millipore water, 18.2 MΩ at 25 °C) to conduct CO stripping voltammetry for two cycles. The scan was between 0.2 and 1.1 V at a rate of 50 mV s^{-1}. The peak potential, where CO was being stripped off, could be read from the first cycle of voltammogram.

5.2.5 Characterizations

Transmission electron microscopy (TEM) and high resolution TEM (HRTEM) images were recorded by JEOL Cryo 2100 microscope at an accelerating voltage of 200 kV. Overall energy dispersive X-ray (EDX) spectrum was conducted by Hitachi S4700 microscope equipped with Oxford Link Isis as elemental analyzer. Scanning transmission electron microscopy (STEM) micrographs and energy dispersive X-ray (EDX) elemental spot analysis and line scans were performed using the high-angle annular dark field mode on JEOL 2010F STEM with Schottky field emitter at an accelerating voltage of 200 kV. Powder X-ray diffraction (XRD) patterns were acquired on Bruker D8 Venture (DUO) diffractometer. TGA was determined by Q50-TGA with a ramp rate of 10 °C min^{-1} to designated temperature under air or nitrogen atmosphere. UV-vis absorption spectra were collected in an Agilent Cary 60 UV-vis spectrophotometer.

5.3 Results and Discussion

5.3.1 Synthesis and characterization of carbon-supported truncated octahedral Pd@Pt core-shell nanostructures

After spraying Pt precursor solution onto as-made truncated Pd/C on the conveyor belt, core-shell $Pd_{86}@Pt_{14}/C$ with high uniformity in terms of size and shape were generated (**Figure 5.1a**), and the overall composition was verified by SEM-EDS. The HRTEM micrograph of $Pd_{86}@Pt_{14}$ nanoparticle showed an apparent contrast in color as indicated by the short, black dash lines. The darker color on the perimeter of the particle referred to the heavier element, further confirming that Pt metal did successfully deposit onto the Pd nanocrystal. The d-spacing between fcc Pt matched well to (200) plane, which is also the dominant Pt surface under hot CO environment due to preferential adsorption (**Figure 5.1b**). The size distribution based on low-magnification TEM micrographs of as-made Pd/C and Pd were calculated to be 3.45 ± 0.51 nm and 3.69 ± 0.41 nm, respectively. The high monodispersity also demonstrated the capability of conveyor transport system for maintaining the tight control over particle size (**Figure 5.1c**). The spot analysis based on STEM micrograph indicated that the outer region of as-made $Pd_{86}@Pt_{14}/C$ was more Pt-rich than the inner region, providing another proof of its core-shell structure. The detailed EDS results were provided in **Figure 5.2**.

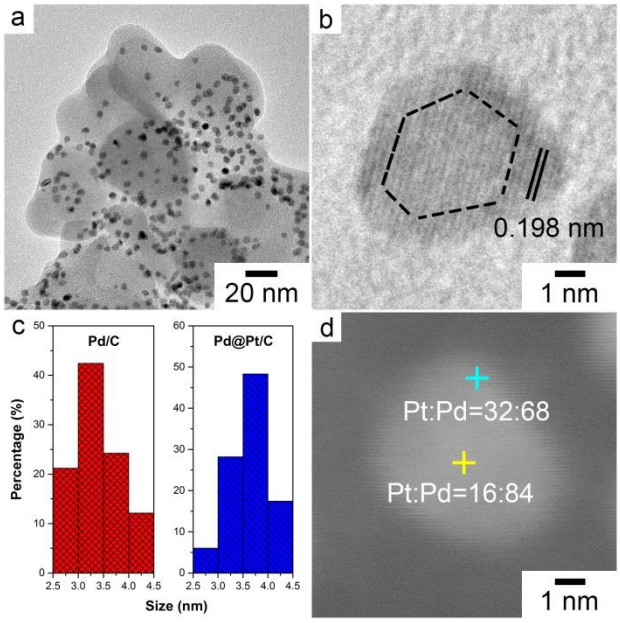

Figure 5.1 (a) TEM and (b) HRTEM micrographs of as-made $Pd_{86}@Pt_{14}/C$ catalysts. (c) Size distributions for Pd/C (left) and $Pd_{86}@Pt_{14}/C$ (right). (d) STEM micrographs of $Pd_{86}@Pt_{14}/C$, and the molar ratios are based on EDS results.

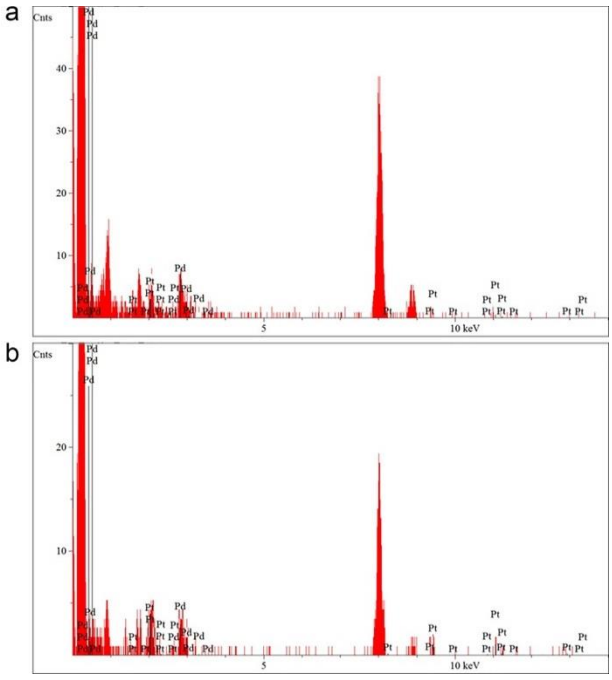

Figure 5.2 EDS results for $Pd_{86}@Pt_{14}/C$ at (a) inner and (b) outer regions in Figure 5.1d.

When the concentration of Pt precursor solution was enhanced by 1.5 times higher, the core-shell structure was well-retained (**Figure 5.3a**). The average size of $Pd_{80}@Pt_{20}/C$ was estimated to be 3.81 ± 0.63 nm, slightly larger than that of $Pd_{86}@Pt_{14}/C$, indicating more Pt metals had grown onto the existing Pt nanoparticles (**Figure 5.3b**). However, when the Pt precursor concentration was increased by 3 times higher, non-uniformity in both size and shape occurred, and Pt could no longer form a uniform shell, indicating the epitaxial growth had slowly changed to self-nucleation (**Figure 5.3c**). The size distribution was also broader than those with less Pt deposition, and the particle size increase to 4.11 ± 0.87 nm (**Figure 5.3d**).

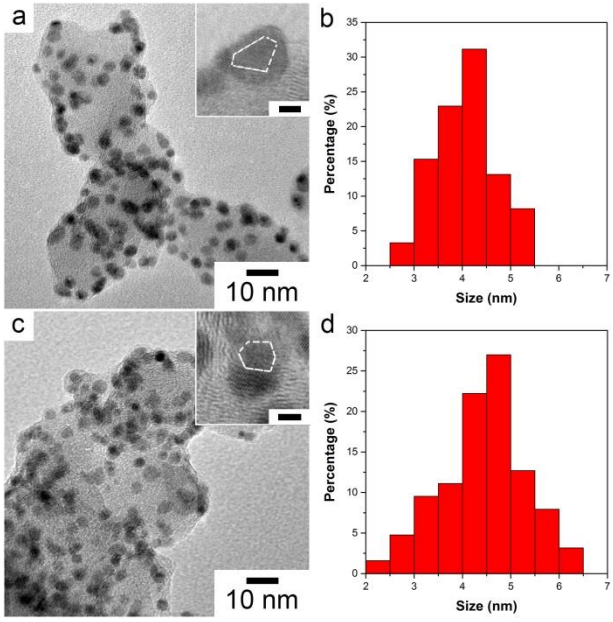

Figure 5.3 (a,c) TEM and HRTEM (inset) micrographs of as-made (a) $Pd_{80}@Pt_{20}/C$ and (b) $Pd_{67}@Pt_{33}/C$ catalysts. The scale bars for inset images correspond to 2 nm. (b,d) size distributions for (a) and (b).

Figure 5.4 summarizes the particle sizes of as-made core-shell structures (blue squares in the figure). The gradual increase in particle size is an evidence of the core-shell formation, where more Pt precursor introduced corresponds to a thicker Pt overlayer. To better understand the Pt deposition, we used a Pd sphere with diameter with the same average size of as-made truncated Pd octahedron as the starting particle, and then calculated the diameter of the spherical Pd@Pt based on different composition. The molar ratio between Pt and Pd can be related by

$$\frac{n_{Pt}}{n_{Pd}} = \frac{m_{Pt}/Mw_{Pt}}{m_{Pd}/Mw_{Pd}} = \frac{\rho_{Pt}V_{Pt}/Mw_{Pt}}{\rho_{Pd}V_{Pd}/Mw_{Pd}} \quad (1)$$

where n is the number of moles, m is the mass, Mw is the molecular weight, ρ is the density and V_i is the volume of individual metal.

The volume of Pt shell can be further calculated by the following equation:

$$V_{Pt} = V - V_{Pd} \quad (2)$$

where V refers to the total volume of the core-shell nanostructure.

For spheres, the volume can be further expressed in terms of its diameter, D, by

$$V = \frac{\pi D^3}{6} \quad (3)$$

$$V_{Pd} = \frac{\pi {D_{Pd}}^3}{6} \quad (4)$$

Plug Eq. (2)-(4) into Eq. (1), we can obtain

$$\frac{n_{Pt}}{n_{Pd}} = \left[\left(\frac{D}{D_{Pd}}\right)^3 - 1\right] \times \frac{\rho_{Pt} Mw_{Pd}}{\rho_{Pd} Mw_{Pt}} \quad (5)$$

After an arrangement, we get

$$D = D_{Pd} \times \left[1 + \frac{n_{Pt}\rho_{Pd} Mw_{Pt}}{n_{Pd}\rho_{Pt} Mw_{Pd}}\right]^{1/3} \quad (6)$$

The relationship between the diameters of spherical $Pd_x@Pt_y$ nanoparticle based on different compositions was plotted in **Figure 5.4** as well (red spheres in the figure). Both experimental and simulated data exhibited a similar trend, which indicate that the Pd-Pt system did follow the mechanism of core-shell formation. The greater particle size change in the truncated octahedral $Pd_x@Pt_y$ particle than its spherical counterpart could be attributed to less Pd surface exposed for polyhedron than the sphere with the same particle size. Therefore, same amount of Pt metal will form a thicker shell on the structure with smaller sphericity. In other words, the structure deviates more from a mathematically-perfect sphere. For instance, Pt shell will be thicker when deposited onto Pd tetrahedron than onto Pd icosahedron.

For Pd@Pt spheres, the radius, r, is equal to the radius of the Pd core, r_{Pd}, plus the thickness of the Pt(200) shell, and can be expressed by

$$r = r_{Pd} + n \times d(200) \quad (7)$$

Since diameter of the sphere is equal to two times of its radius, we get

$$D = D_{Pd} + 2 \times n \times d(200) \quad (8)$$

By combining Eq. (6) and Eq. (8), the number of Pt layers can be related to the composition of synthesized $Pd_x@Pt_y$ nanostructures. The n-value for as-made $Pd_{86}@Pt_{14}/C$, $Pd_{80}@Pt_{20}/C$ and $Pd_{67}@Pt_{33}/C$ were calculated to be 1.12 nm, 1.43 nm and 2.19 nm, respectively. All n-values were larger than 1, indicating the full Pt metal coverage on Pd core, avoiding any exposed Pd surfaces and thus enhance the catalytic activity towards ORR in the fuel cell.

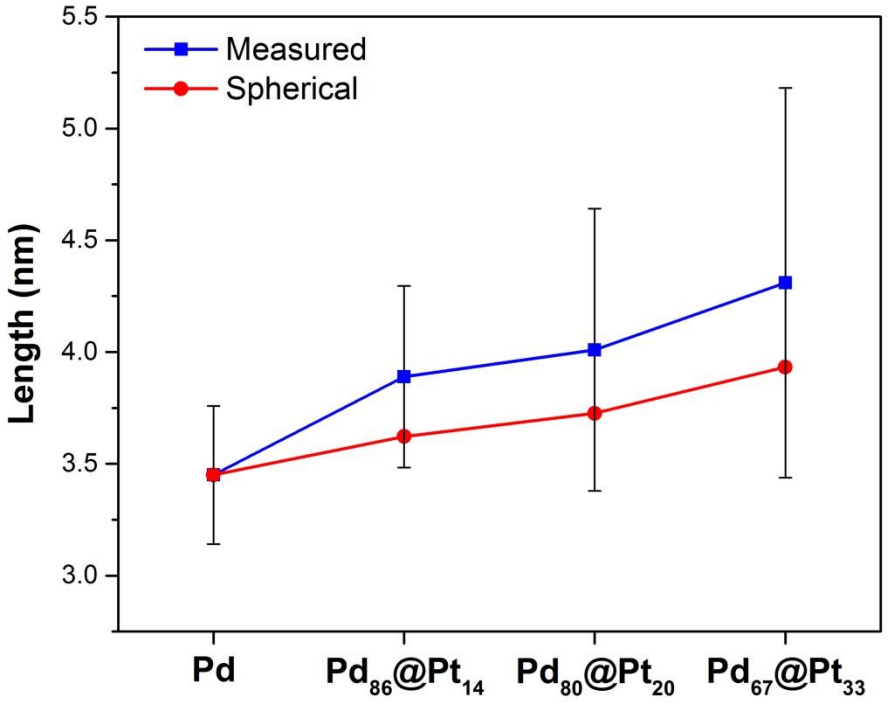

Figure 5.4 Size distributions of as-made Pd/C and $Pd_x@Pt_y/C$ catalysts in comparison with their spherical counterparts.

CO stripping voltammetry, a highly surface-sensitive measurement commonly used for the study of the electro-oxidation characteristics of adsorbed CO, was employed to further confirm the core-shell structure. CO is one of the most common intermediates generated during methanol oxidation reaction, and tends to strongly adsorb onto electrocatalyst surfaces.[39-41] According to theoretical studies, CO molecules bind to Pd surfaces stronger than to Pt surfaces; in other words, it takes more energy for CO to desorb from the Pd surfaces.[42-44] Therefore, in CO stripping voltammogram, Pd electrocatalysts will exhibit a more positive CO stripping peak potential than the Pt electrocatalyst. It was reported that Pt-Pd bimetallic alloy electrocatalysts showed more positive CO stripping peak potential and reduced CO coverage in Pd-rich system, whereas the peak potential shifted in the negative direction as the Pt content increased.[45-46]

After saturating the as-made core-shell electrocatalyst surface with CO, cyclic voltammetry was performed and the peak potential was recorded. **Figure 5.5** showed the CO stripping voltammogram of three different $Pd_x@Pt_y/C$ core-shell nanocatalsyts between 0.8 V and 0.9 V, which are close to the peak potentials of reference Pt/C and Pd/C, respectively.[45] The peak potential followed the order of E_{peak} ($Pd_{67}@Pt_{33}/C$) < E_{peak} ($Pd_{80}@Pt_{20}/C$) < E_{peak} ($Pd_{86}@Pt_{14}/C$), and moves to more negative values as the Pt deposition increased, which is indicative of the weaker CO bonding on Pt surface. It approached to that of reference Pt/C when Pt shell is thick enough to offset any lattice strain induced by the underlying Pd core.

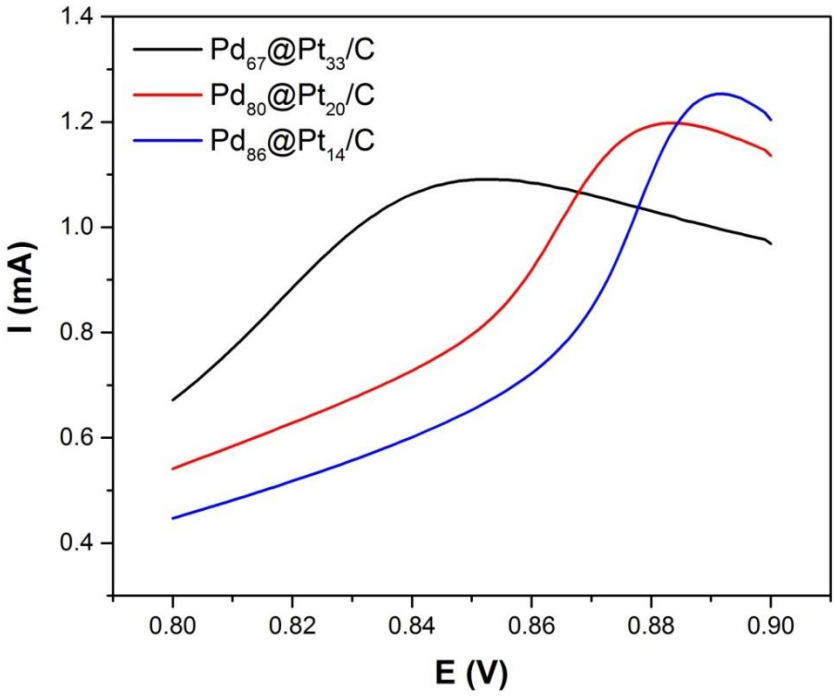

Figure 5.5 CO stripping voltammograms of as-made $Pd_x@Pt_y/C$ catalysts in Ar-saturated 0.1 M $HClO_4$. Scan rate = 50 mA/s.

As mentioned in our previous work and in Chapter 3, $Pt(acac)_2$ and $Pd(acac)_2$ will undergo complexation reaction with oleylamine and oleic acid to form $[Pt\text{-}((C_{18}H_{35})NH_2)_4]^{2+}$ and $[Pd\text{-}((C_{17}H_{33})COOH)_4]^{2+}$ complexes, respectively.[47] After mixing a solution of $Pt(acac)_2$ and oleylamine with another solution of $Pd(acac)_2$ and oleic acid, a new complex formed when the mixture was heated at elevated temperature, as shown in the UV-Vis spectrum (**Figure 5.6**). Both pre-mixed solutions had characteristic peaks at around 275 nm, which can be associated with the binding between metal cations and long-chain ligands (**1** and **2** in the figure). This peak

disappears completely when two solutions were mixed together, instead, a new peak located at about 312 nm appeared (**3** in the figure). The new curve was totally different from that obtained by superimposing the spectrum of individual unmixed solutions, and could not be obtained when either oleylamine or oleic acid was absent in the system. Therefore, it can be concluded that the peak is most likely attributed to the interaction between the two ligands. When Pt precursor solution was sprayed onto the as-made Pd/C on the preheated belt, the high temperature induced the reaction between oleylamine in the Pt precursor solution and oleic acid capped on the Pd surface, facilitating the Pt shell formation on the originally existed Pd particles.

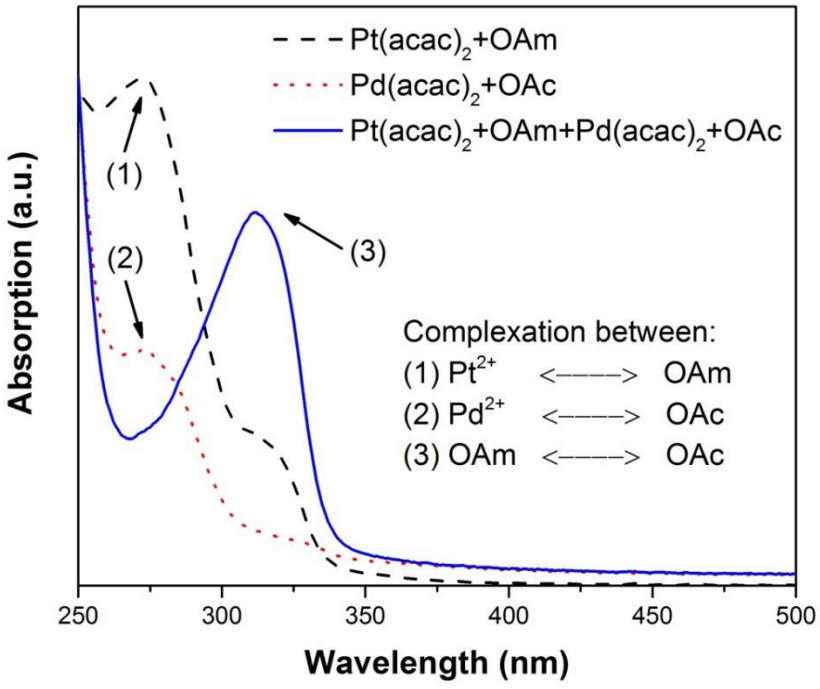

Figure 5.6 UV-Vis spectrum of a mixture of metal acetylacetonates and ligands (oleylamine and/or oleic acid) dissolved in chloroform.

When keeping all conditions the same but replacing as-made Pd/C with commercial Pd/C as starting core material, severe self-nucleation of Pt particles happened, where much larger Pt particles were mixed with smaller Pd particles. Due to the lack of oleic acid in the system, $[Pt-((C_{18}H_{35})NH_2)_4]^{2+}$ has less tendency to deposit onto the Pd surface and will simply undergo thermal decomposition and form Pt nanoparticles by itself, which resulted in polydispersity and further confirmed the proposed hypothesis (**Figure 5.7**).

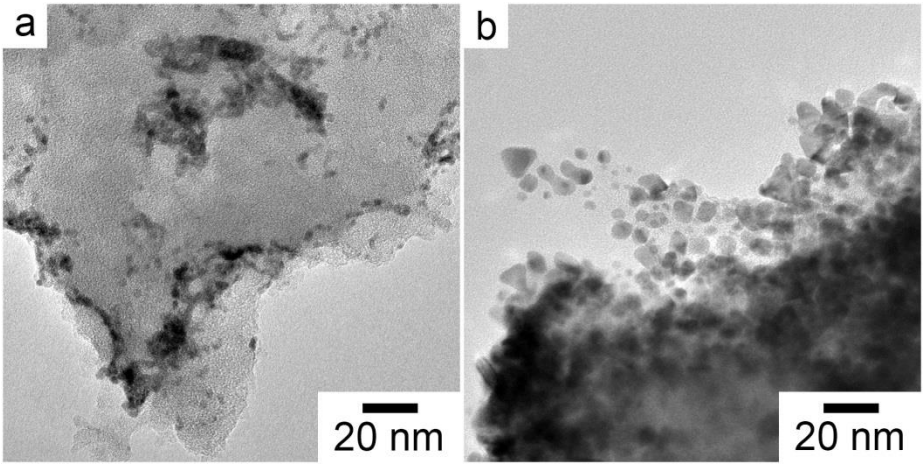

Figure 5.7 TEM micrographs of (a) commercial Pd/C catalyst and (b) $Pd_{86}@Pt_{14}/C$ catalyst using commercial Pd/C as starting core material.

Furthermore, according to the classical nucleation theory, the critical energy barrier is generally smaller for heterogeneous nucleation than that for homogeneous one. If sufficient sites are available for heterogeneous nucleation, both number of critical clusters and nucleation rate

would be larger for heterogeneous nucleation than those for homogenous one. Thus, the solute atoms nucleate and grow heterogeneously. Therefore, Pt atoms prefer to grow onto existing Pd nanocrystals over self-nucleate into separate Pt particles.[48-51] During heterogeneous nucleation, the growth mode and final nanostructure can be determined by lattice mismatch, *F*. If Metal A nucleates on the surface of Metal B, the lattice mismatch can thus be defined as[52]

$$F = \frac{a_A - a_B}{a_B} \tag{9}$$

where a_A and a_B are lattice parameters for metals A and B, respectively. In our system, A refers to Pt and B refers to Pd.

If the mismatch between two metals is small, metal A will preferably deposit onto metal B epitaxially in a layer-by-layer fashion (Frank-van der Merwe mode). On the contrary, if the mismatch is relatively large, metal A will grow onto substrate metal B in an island form (Volmer-Weber mode).[53] In the Pt-Pd system, both metals have very similar lattice parameters (3.92 Å for Pt and 3.89 Å for Pd), leading to Pd@Pt core-shell nanostructure instead of undesirable Pt-on-Pd island-on-particle geometry.

Kinetic control was also applied to passivate the self-nucleation of Pt nanoparticles during the reaction. For instance, a mixture of CO and N_2 was used as the purging gas rather than pure CO gas to lower its reducing ability. The wall temperature of quartz tube was decreased from

230 °C to 210 °C to slightly slow down the growth kinetics and thus made layer-by-layer formation preferably.

5.3.2 Synthesis and characterization of carbon-supported cubic Pt@Au core-shell nanostructures

A similar approach was also applied to the one-step synthesis of carbon-supported cubic Pt@Au nanoparticles. After spraying Au precursor solution onto as-made cubic Pt/C, size- and shape-controlled cubic Pt@Au/C could be continuously generated (**Figure 5.8a**). From the HRTEM micrograph, the crystallographic planes were very different from those in Pt nanocubes, whose dominant planes are lying either parallel or perpendicular to edges. The lattice fringe is measured to be 0.230 nm and can be indexed to fcc Au(111) plane (**Figure 5.8b**). The average size of as-made nanostructures (3.34 ± 0.20 nm) is slightly smaller than the uncoated Pt/C (3.54 ± 0.25 nm), while both showed relatively narrow size distributions (**Figure 5.8c**). The STEM-EDS results showed that molar ratio of Au/Pt was higher on the outside region than that in the center, and the larger particle size and Au-rich surface indicated that Au metal successfully deposit onto the Pt core (**Figure 5.8d**). The detailed EDS data was provided here for reference as well (**Figure 5.9**). Although EDS is one of the most common analytical techniques used for the

elemental analysis of a sample, it is actually not the suitable approach to characterize Pt-Au system, because the energy of certain X-rays emitted from Pt atom is quite similar to those from Au atom, making their overlap indistinguishable. Therefore, TEM and XRD appear to be more persuasive in differentiating two metals in the system.

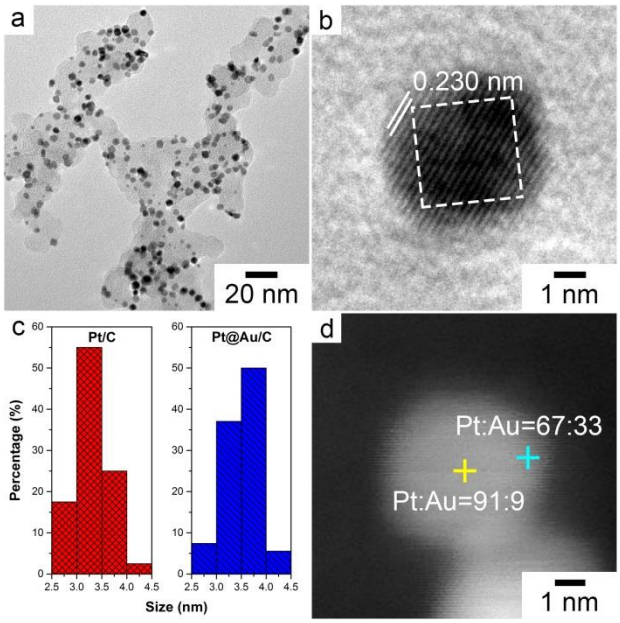

Figure 5.8 (a) TEM and (b) HRTEM micrographs of as-made $Pt_{80}@Au_{20}/C$ catalysts. (c) Size distributions for Pt/C (left) and $P_{80}@Au_{20}/C$ (right). (d) STEM micrographs of $Pt_{80}@Au_{20}/C$, and the molar ratios are based on EDS results.

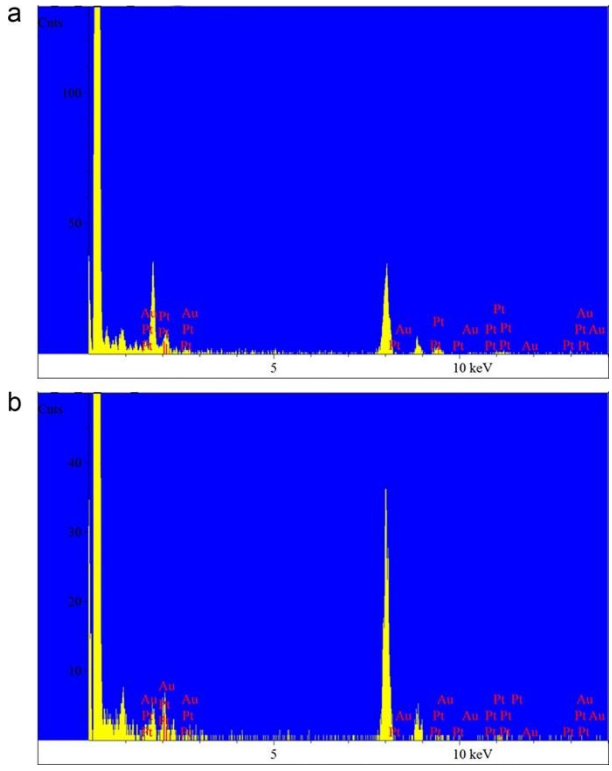

Figure 5.9 EDS results for $Pt_{86}@Au_{14}/C$ at (a) inner and (b) outer regions in Figure 5.8d.

Figure 5.10 showed the XRD pattern for as-made $Pt_{80}@Au_{20}/C$ core-shell catalyst. The peak positions were almost identical to those of reference fcc Au nanostructure, which indicated the full coverage of Au shell and no Pt nanocubes were exposed. A slight positive shift in the XRD pattern implied that the lattice of surface Au atom was suppressed, which could be explained by the difference in their lattice constants. Owing to the smaller lattice constant, Pt can induce compressive strain on the Au overlayer, and make the peak position move in a high-angle direction.

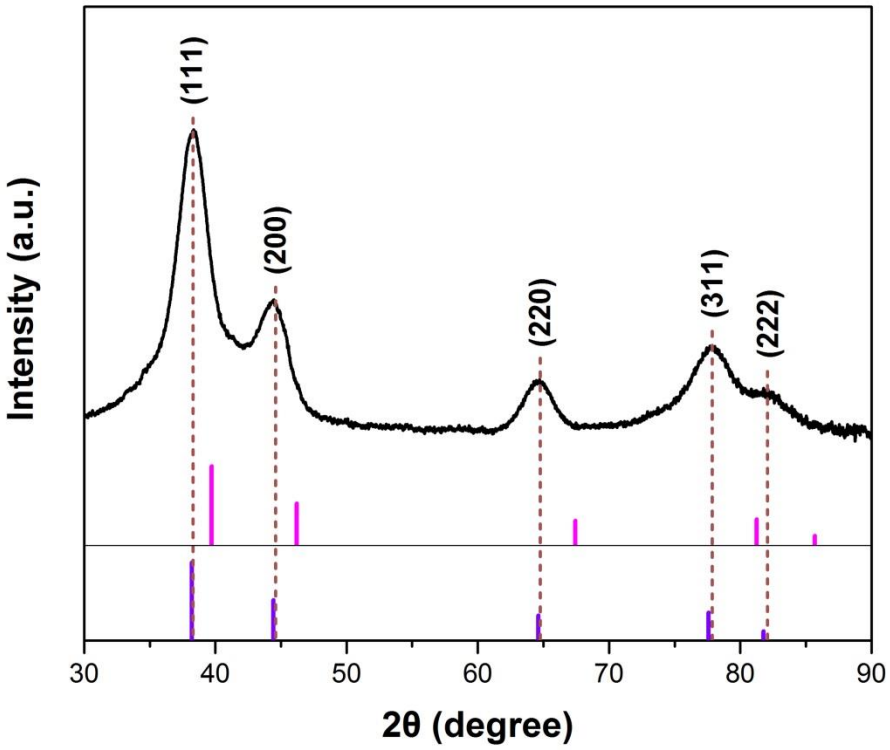

Figure 5.10 PXRD patterns of as-prepared cubic $Pt_{80}@Au_{20}/C$ catalyst. Color code for the reference X-ray diffraction lines are Pt in pink and Au in violet.

It has been reported that gold halide, including AuCl and AuBr, can coordinate with oleylamine to form [AuX-oleylamine] complexes through the amine groups. Oleylamine acts as both complexing agent and stabilizing agent to slow down the decomposition of Au precursor by forming a complex.[54-58] In the conveyor transport system, when Au precursor solution was sprayed onto the oleylamine-capped Pt nanocubes, new binding was formed between gold chloride and oleylamine, facilitating the Au shell formation on the existing Pt particles. Together

with kinetic control, uniform layer-by-layer growth mode can thus be achieved, similar to that of Pd@Pt core-shell structure. However, if the concentration of Au precursor solution was too high, severe self-nucleation occurred and much larger Au nanoparticles were observed, generated form the excess $AuCl_3$ precursor that could not undergo complexation with oleylamine (**Figure 5.11**).

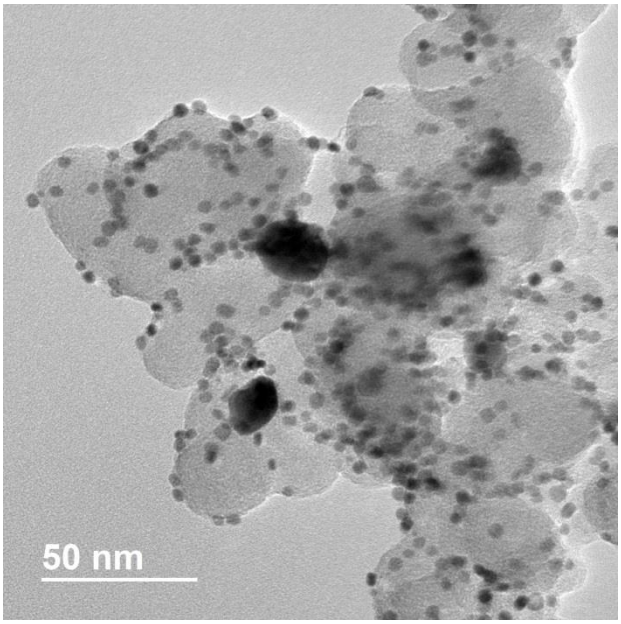

Figure 5.11 TEM micrograph of as-made $Pt_{50}@Au_{50}/C$ catalyst.

5.4 Conclusion

A new approach was developed to produce truncated octahedral Pd@Pt/C and cubic Pt@Au/C catalysts in a continuous fashion. Size distribution analysis and CO stripping voltammetry were also conducted to confirm its core-shell structure. The complexation between ligands (oleylamine and oleic acid) as well as that between metal precursor and ligand ($AuCl_3$ and oleylamine) helped facilitate the layer-by-layer (VW) growth mode. This significantly simplified the traditional tedious synthesis route for core-shell particle, and holds the potential for large-scale production of supported catalysts with more complex nanostructures in the future.

5.5 References

1. Stamenkovic, V. R.; Mun, B. S.; Mayrhofer, K. J. J.; Ross, P. N.; Markovic, N. M. *J. Am. Chem. Soc.* **2006**, *128*, 8813-8819.

2. Durst, J.; Lopez-Haro, M.; Dubau, L.; Chatenet, M.; Soldo-Olivier, Y.; Guetaz, L.; Bayle-Guillemaud, P.; Maillard, F. *J. Phys. Chem. Lett.* **2014**, *5*, 434-439.

3. Liao, H. B.; Fisher, A.; Xu, Z. C. J. *Small* **2015**, *11*, 3221-3246.

4. Habas, S. E.; Lee, H.; Radmilovic, V.; Somorjai, G. A.; Yang, P. *Nat. Mater.* **2007**, *6*, 692-697.

5. Peng, Z. M.; You, H. J.; Yang, H. *Adv. Funct. Mater.* **2010**, *20*, 3734-3741.

6. Adzic, R. R.; Zhang, J.; Sasaki, K.; Vukmirovic, M. B.; Shao, M.; Wang, J. X.; Nilekar, A. U.; Mavrikakis, M.; Valerio, J. A.; Uribe, F. *Top. Catal.* **2007**, *46*, 249-262.

7. Strasser, P.; Koh, S.; Anniyev, T.; Greeley, J.; More, K.; Yu, C. F.; Liu, Z. C.; Kaya, S.; Nordlund, D.; Ogasawara, H.; Toney, M. F.; Nilsson, A. *Nat. Chem.* **2010**, *2*, 454-460.

8. Tao, F.; Grass, M. E.; Zhang, Y. W.; Butcher, D. R.; Renzas, J. R.; Liu, Z.; Chung, J. Y.; Mun, B. S.; Salmeron, M.; Somorjai, G. A. *Science* **2008**, *322*, 932-934.

9. Tao, F.; Grass, M. E.; Zhang, Y. W.; Butcher, D. R.; Aksoy, F.; Aloni, S.; Altoe, V.; Alayoglu,

S.; Renzas, J. R.; Tsung, C. K.; Zhu, Z. W.; Liu, Z.; Salmeron, M.; Somorjai, G. A. *J. Am. Chem. Soc.* **2010**, *132*, 8697-8703.

10. Wang, D. L.; Xin, H. L. L.; Hovden, R.; Wang, H. S.; Yu, Y. C.; Muller, D. A.; DiSalvo, F. J.; Abruna, H. D. *Nat. Mater.* **2013**, *12*, 81-87.

11. Peng, Z. M.; Yang, H. *J. Am. Chem. Soc.* **2009**, *131*, 7542-7545.

12. Peng, Z. M.; Wu, J. B.; Yang, H. *Chem. Mat.* **2010**, *22*, 1098-1106.

13. Choi, S. I.; Shao, M. H.; Lu, N.; Ruditskiy, A.; Peng, H. C.; Park, J.; Guerrero, S.; Wang, J. G.; Kim, M. J.; Xia, Y. N. *ACS Nano* **2014**, *8*, 10363-10371.

14. Wang, X.; Choi, S. I.; Roling, L. T.; Luo, M.; Ma, C.; Zhang, L.; Chi, M. F.; Liu, J. Y.; Xie, Z. X.; Herron, J. A.; Mavrikakis, M.; Xia, Y. N. *Nat. Commun.* **2015**, *6*.

15. Wu, J.; Shi, M.; Yin, X.; Yang, H. **2013**, *6*, 1888-1892.

16. Zhou, W. P.; Sasaki, K.; Su, D.; Zhu, Y. M.; Wang, J. X.; Adzic, R. R. *J. Phys. Chem. C* **2010**, *114*, 8950-8957.

17. Zhang, J. L.; Vukmirovic, M. B.; Xu, Y.; Mavrikakis, M.; Adzic, R. R. *Angew. Chem.-Int. Edit.* **2005**, *44*, 2132-2135.

18. Zhang, J.; Sasaki, K.; Sutter, E.; Adzic, R. R. *Science* **2007**, *315*, 220-222.

19. Sasaki, K.; Naohara, H.; Cai, Y.; Choi, Y. M.; Liu, P.; Vukmirovic, M. B.; Wang, J. X.; Adzic, R. R. *Angew. Chem.-Int. Edit.* **2010**, *49*, 8602-8607.

20. Kuttiyiel, K. A.; Sasaki, K.; Choi, Y. M.; Su, D.; Liu, P.; Adzic, R. R. *Nano Lett.* **2012**, *12*, 6266-6271.

21. Adzic, R. *Electrocatalysis* **2012**, *3*, 163-169.

22. Kuttiyiel, K. A.; Sasaki, K.; Su, D.; Vukmirovic, M. B.; Marinkovic, N. S.; Adzic, R. R. *Electrochim. Acta* **2013**, *110*, 267-272.

23. Zhang, J.; Lima, F. H. B.; Shao, M. H.; Sasaki, K.; Wang, J. X.; Hanson, J.; Adzic, R. R. *J. Phys. Chem. B* **2005**, *109*, 22701-22704.

24. Strasser, P.; Koha, S.; Greeley, J. *Phys. Chem. Chem. Phys.* **2008**, *10*, 3670-3683.

25. Oezaslan, M.; Strasser, P. *J. Power Sources* **2011**, *196*, 5240-5249.

26. Neyerlin, K. C.; Srivastava, R.; Yu, C. F.; Strasser, P. *J. Power Sources* **2009**, *186*, 261-267.

27. Mani, P.; Srivastava, R.; Strasser, P. *J. Power Sources* **2011**, *196*, 666-673.

28. Hasche, F.; Oezaslan, M.; Strasser, P. *ChemCatChem* **2011**, *3*, 1805-1813.

29. Gan, L.; Heggen, M.; Rudi, S.; Strasser, P. *Nano Lett.* **2012**, *12*, 5423-5430.

30. Gan, L.; Heggen, M.; O'Malley, R.; Theobald, B.; Strasser, P. *Nano Lett.* **2013**, *13*, 1131-

1138.

31. Gan, L.; Cui, C. H.; Heggen, M.; Dionigi, F.; Rudi, S.; Strasser, P. *Science* **2014**, *346*, 1502-1506.

32. Cui, C. H.; Gan, L.; Heggen, M.; Rudi, S.; Strasser, P. *Nat. Mater.* **2013**, *12*, 765-771.

33. Shao, M. H.; Smith, B. H.; Guerrero, S.; Protsailo, L.; Su, D.; Kaneko, K.; Odell, J. H.; Humbert, M. P.; Sasaki, K.; Marzullo, J.; Darling, R. M. *Phys. Chem. Chem. Phys.* **2013**, *15*, 15078-15090.

34. Shao, M. H.; Shoemaker, K.; Peles, A.; Kaneko, K.; Protsailo, L. *J. Am. Chem. Soc.* **2010**, *132*, 9253-9255.

35. Chung, Y. H.; Chung, D. Y.; Jung, N.; Park, H. Y.; Yoo, S. J.; Jang, J. H.; Sung, Y. E. *J. Phys. Chem. C* **2014**, *118*, 9939-9945.

36. Chen, C.; Kang, Y. J.; Huo, Z. Y.; Zhu, Z. W.; Huang, W. Y.; Xin, H. L. L.; Snyder, J. D.; Li, D. G.; Herron, J. A.; Mavrikakis, M.; Chi, M. F.; More, K. L.; Li, Y. D.; Markovic, N. M.; Somorjai, G. A.; Yang, P. D.; Stamenkovic, V. R. *Science* **2014**, *343*, 1339-1343.

37. Han, L.; Liu, H.; Cui, P. L.; Peng, Z. J.; Zhang, S. J.; Yang, J. *Sci Rep* **2014**, *4*.

38. Pan, Y. T.; Wu, J. B.; Yin, X.; Yang, H. *Aiche J.* **2016**, *62*, 399-407.

39. Markovic, N. M.; Ross, P. N. *Surf. Sci. Rep.* **2002**, *45*, 121-229.

40. Iwasita, T. *Electrochim. Acta* **2002**, *47*, 3663-3674.

41. Herrero, E.; Chrzanowski, W.; Wieckowski, A. *J. Phys. Chem.* **1995**, *99*, 10423-10424.

42. Wong, Y. T.; Hoffmann, R. *J. Phys. Chem.* **1991**, *95*, 859-867.

43. Hammer, B.; Morikawa, Y.; Norskov, J. K. *Phys. Rev. Lett.* **1996**, *76*, 2141-2144.

44. Eichler, A. *Surf. Sci.* **2002**, *498*, 314-320.

45. Choi, B.; Nam, W. H.; Chung, D. Y.; Park, I. S.; Yoo, S. J.; Song, J. C.; Sung, Y. E. *Electrochim. Acta* **2015**, *164*, 235-242.

46. Papageorgopoulos, D. C.; Keijzer, M.; Veldhuis, J. B. J.; de Bruijn, F. A. *J. Electrochem. Soc.* **2002**, *149*, A1400-A1404.

47. Tsao, K. C.; Yang, H. *Small* **2016**, *12*, 4808-4814.

48. Porter, D. A.; Easterling, K. E. *Phase Transformations in Metals and Alloys* (2nd ed.) **1992**, London: Chapman & Hall.

49. Mullin, J. W. *Crystallization* (3rd ed.) **1997**, Oxford: Oxford University Press.

50. Khamskii, E. *Crystallization from Solutions* (1st ed.) **1969**, New York: Consultants Bureau.

51. Kashchiev, D. *Nucleation: Basic Theory with Applications* (1st ed.) **2000**, Oxford: Butterworth Heinemann.

52. Chambers, S. A. *Surf. Sci. Rep.* **2000**, *39*, 105-180.

53. Liu, A. W. K.; Santos, M. B. *Thin Films: Heteroepitaxial Systems* (1st ed.) **1999**, Singapore: World Scientific.

54. Ma, Y. Y.; Zeng, J.; Xia, Y. N. *Acta Phys.-Chim. Sin.* **2009**, *25*, 1026-1032.

55. Ma, Y. Y.; Zeng, J.; Li, W. Y.; McKiernan, M.; Xie, Z. X.; Xia, Y. N. *Adv. Mater.* **2010**, *22*, 1930-1934.

56. Lu, X. M.; Yavuz, M. S.; Tuan, H. Y.; Korgel, B. A.; Xia, Y. N. *J. Am. Chem. Soc.* **2008**, *130*, 8900-8901.

57. Lu, X. M.; Tnan, H. Y.; Korgel, B. A.; Xia, Y. N. *Chem.-Eur. J.* **2008**, *14*, 1584-1591.

58. Li, Z. Q.; Tao, J.; Lu, X. M.; Zhu, Y. M.; Xia, Y. N. *Nano Lett.* **2008**, *8*, 3052-3055.

Chapter 6:

Supported and Shaped Nanocatalysts as Electrode Material for Enhanced Electrocatalytic Performance

6.1 Introduction

Developing new technologies that utilize renewable energy sources has gained tremendous research interest recently. One example is proton exchange membrane fuel cells (PEMFCs), which convert the chemical energy stored in fuel molecules into electric energy. During operations, different fuels are fed to the anode to carry out the hydrogen oxidation reaction (HOR), methanol oxidation reaction (MOR) or formic acid oxidation reaction (FAOR), while oxygen gas is fed to the cathode and undergoes reduction (ORR). Since the reactivity strongly depends on the structure of the nanocatalysts, catalysts with controlled geometries are commonly used as the electrode materials to improve the performance of these electrochemical reactions.[1-4] More effort has been put on the improvement of the electrocatalytic activity and stability of these catalysts towards the ORR due to its relatively sluggish kinetics, with carbon-supported Pt-based materials being the most common. Complete, one-step, reduction of oxygen to water is necessary to maximize the amount of energy which is stored in the chemical bond of the hydrogen molecule and thus enhance the performance in both automotive and locomotive applications.

In PEMFC, the direct hydrogen fuel cell (DHFC) received the highest interest due to its clean products and zero CO_2 emission. However, most of the world's hydrogen supply is currently obtained through hydrocarbon reforming and always contains significant amounts of CO that can poison the electrocatalysts within the DMFC thereby reducing the power output. Consequently, some approaches are required to selectively reduce the CO content in the feed with minimal loss of H_2. Preferential CO oxidation (PROX) is the most promising and low-cost reaction to produce high-purity H_2 for DHFC, and the catalysts used are mainly Pt-Ru nanocrystals supported on either Al_2O_3 or CeO_2.[5]

Considering recent research efforts,[6-7] the emphasis of this chapter is placed on the electrocatalytic performance of MOR over as-made carbon-supported Pt nanocubes as well as the activity and stability of ORR over Pt-based alloys and core-shell nanostructures in acidic media.

6.2 Experimental

6.2.1 Chemical and materials

2-propanol (J.T.Baker, >99.7%); Nafion 117 solution (Sigma-Aldrich, 5%); perchloric acid ($HClO_4$, GFS Chemicals, 70%); carbon black (Vulcan XC-72, Cabot); commercial Pt/C (BASF, 20%); commercial Pd/C (Sigma-Aldrich, 10%); hydrogen (H_2, UHP, Airgas); argon (Ar, UHP, Airgas); oxygen (O_2, Research Grade, Airgas). All were used as received.

6.2.2 Electrochemical measurement for methanol oxidation reaction (MOR)

A three-electrode cell system was used. The working electrode was a glassy-carbon rotating disk electrode (RDE) with an area of 0.196 cm^2. A platinum foil of 1 cm^2 was used as the counter electrode with a HydroFlex hydrogen electrode in a separate compartment as the reference. The as-prepared catalyst was mixed with 10 mL of AA and then stirred for 2 h at 70 °C.[8] The sample was washed with 10 mL of ethanol and subsequently underwent centrifugation at 6800 rpm three times, followed by drying under ambient air. To make a catalyst ink, 3 mg of as-prepared cubic Pt/C or commercial BASF Pt/C catalysts was added in a mixture of 4 mL of deionized water, 1 mL of isopropanol, and 25 μL of 5% Nafion. A small volume of this catalyst ink (40 μL) was drop cast on top of the RDE to make the working electrode. The electrochemical surface area

(ECSA) was calculated from the adsorption of hydrogen species in the range between 0.05 and 0.4 V in the CV curves. The CV test was conducted in an Ar-saturated, aqueous solution of 0.1 M $HClO_4$. The test was performed at room temperature with a scan rate of 50 mV s^{-1}. MOR activity was measured in Ar-saturated aqueous solution of 0.1 M $HClO_4$ and 0.5 M methanol. The scan was between 0 and 1.2 V at a rate of 50 mV s^{-1}. The current density was calculated based on the geometric area of the electrode.

6.2.3 Electrochemical measurement for oxygen reduction reaction (ORR)

The set-up of cell, ink preparation and CV test are the same as that for MOR. ORR activity was measured in O_2-saturated aqueous solution of 0.1 M $HClO_4$. The scan was between 0 and 1.1 V at a rate of 10 mV s^{-1}. The current density was calculated based on the ECSA values.

6.2.4 Accelerated durability test (ADT) for oxygen reduction reaction (ORR)

The set-up of cell and the ink preparation are the same as that for the methanol oxidation reaction. ADT was carried out by applying cyclic voltammetry on the catalysts in O_2-saturated aqueous solution of 0.1 M $HClO_4$ between 0.6 V and 1.1 V with a scan rate of 100 mV s^{-1} for 2500, 5000, 7500 and 10000 cycles.

6.3 Results and Discussion

6.3.1 Electrocatalytic performance towards methanol oxidation reaction (MOR)

Figure 6.1 shows the MOR performance for the cubic and commercial Pt/C catalysts using the typical three-electrode setup. The peak at around 0.25 V in the CV curve could be attributed to the hydrogen adsorption on the Pt(100) surfaces.[1, 9]

Although the on-set potentials in the forward scan of the MOR test for both catalysts were quite similar, the cubic Pt/C catalyst had much lower peak current potentials, shifted by 0.068 V for the forward scan and 0.044 V for the backward scan, suggesting an improved electrocatalytic activity toward methanol oxidation. The peak in the reverse scan can be attributed to the reduction of incompletely oxidized species such as CO_{ad} and $HCOO_{ad}$. The ratio of the forward anodic peak current density (I_f) to the reverse anodic peak current density (I_b) has been used to describe the tolerance of the catalyst to the accumulation of carbonaceous species; therefore, the high I_f/I_b ratio indicates a more efficient removal of adsorbed intermediates than the commercial Pt/C electrocatalyst (1.27 for cubic Pt/C and 0.59 for commercial Pt/C).[10-11] Furthermore, Pt nanocubes had a higher forward peak current density and a lower backward peak current density than the reference Pt/C, indicating methanol was oxidized more effectively with less unwanted intermediates for the cubic Pt/C catalyst.

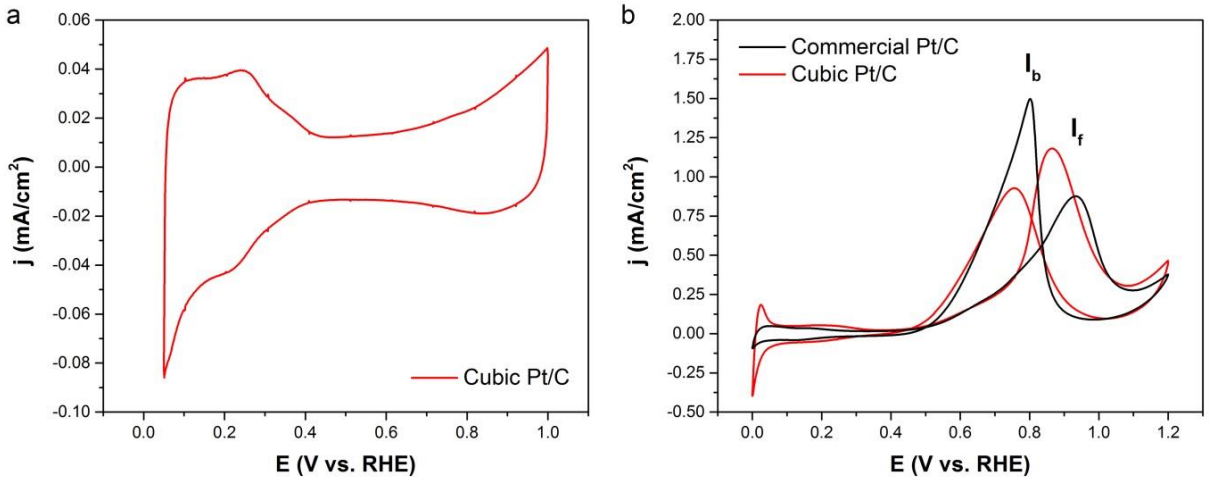

Figure 6.1 (a) CV and (b) MOR curves for the cubic Pt/C and reference Pt/C catalysts.

6.3.2 Electrocatalytic performance towards oxygen reduction reaction (ORR)

As-made Pt_3Ni/C catalysts were used to catalyze the electro-reduction of oxygen molecules. In CV curves, Pt_3Ni/C synthesized using oleylamine and oleic acid as capping ligands showed a characteristic peak at a position similar to that for cubic Pt/C, which was due to the hydrogen adsorption on the (100) facets of Pt, evidence of its cubic morphology. The octahedral Pt_3Ni/C has a broad hydrogen adsorption peak between 0.1 and 0.3 V, similar to that observed for icosahedral Pt/C, and was associated with the (111)-dominated surfaces (**Figure 6.2a**).[9, 12]

For ORR measurement, oxide will form at a higher potential, resulting in decreased catalytic activity. Therefore, the forward scan cannot overlap with the backward scan and thus form the

hysteresis in the O_2 polarization curve. Because of this, people usually focus on the forward scan to better reflect the intrinsic ORR activity of the as-made catalysts. The synthesized cubic and octahedral Pt_3Ni/C catalysts both exhibited higher ORR activities, as the polarization curve was shifted to a positive direction when compared to the reference Pt/C catalyst. The on-set potentials for the ORR polarization curves follow the order of octahedral Pt_3Ni/C> cubic Pt_3Ni/C > commercial Pt/C, indicating that the shape-controlled catalysts were capable of catalyzing ORR at a relatively lower overpotential. The specific area activity was calculated to be 0.71 mA cm^2 and 0.50 mA cm^2 for octahedral and cubic Pt_3Ni/C, respectively, showing more than two and four times higher activities when compared to Pt/C catalyst (**Figure 6.2b**).

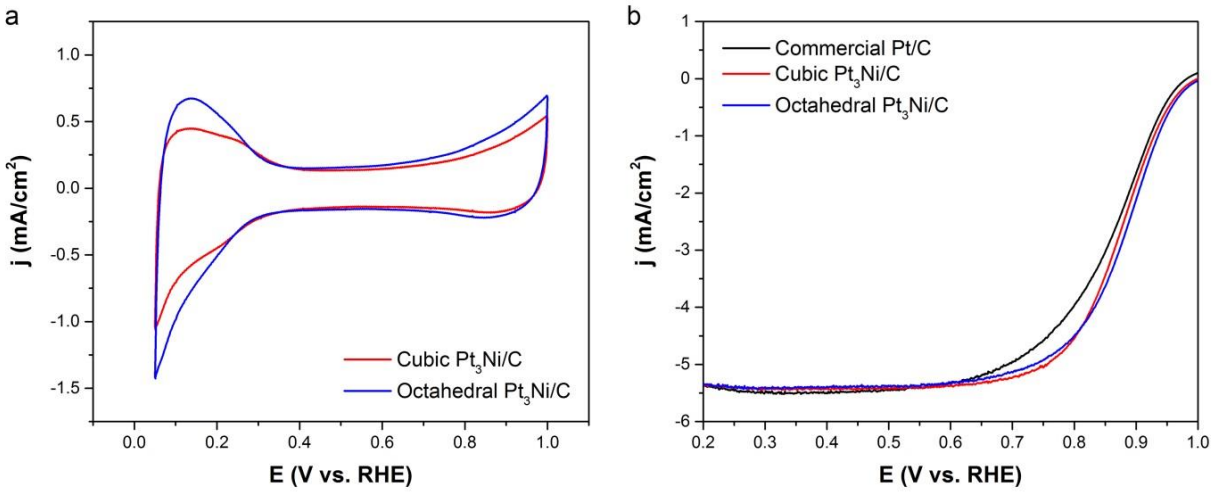

Figure 6.2 (a) CV and (b) ORR curves for the cubic and octahedral Pt_3Ni/C and reference Pt/C catalysts.

As-made Pd-Pt core-shell catalysts with different composition were also used to catalyze the ORR (**Figure 6.3a**). Among them, $Pd_{86}@Pt_{14}/C$ showed the highest activity as it needed the lowest overpotential to achieve the same output of current density. Since Pd metal has a smaller lattice than Pt metal, it will induce a compressive strain on the Pt overlayer. According to theoretical studies, this compressive strain can slightly weaken the binding of oxygenated species on the surface Pt atoms and thus enhance its electrocatalytic performance. When the Pt shell becomes larger, this strain effect induced by the sublayer is negligible, and the ORR activity decreases and approaches to that of a pure Pt catalyst.

ADT was conducted for both $Pd_{86}@Pt_{14}/C$ and reference Pt/C catalysts to test their durability, which is an extremely important factor for PEMFCs commercialization (**Figure 6.3b**). After 5000 accelerated cycles, commercial Pt/C lost about 47% of its ECSA, while $Pd_{86}@Pt_{14}/C$ showed a much lower degradation of only 11%. A much larger initial ECSA and I_s also demonstrated that a small amount of Pt was required to achieve the same level of electrocatalytic activity, thus bringing down the overall cost and making the whole process more economically efficient. Core-shell nanostructures with a thin Pt skin generally exhibit higher ORR activity and stability owing to the favorable electronic properties and optimal d-band centers;[13-16] on the contrary, pure Pt/C usually suffers from Ostwald ripening and aggregation of Pt nanoparticles during continuous fuel cell operation (**Figure 6.4**), thus reducing its long-term stability.[17-18]

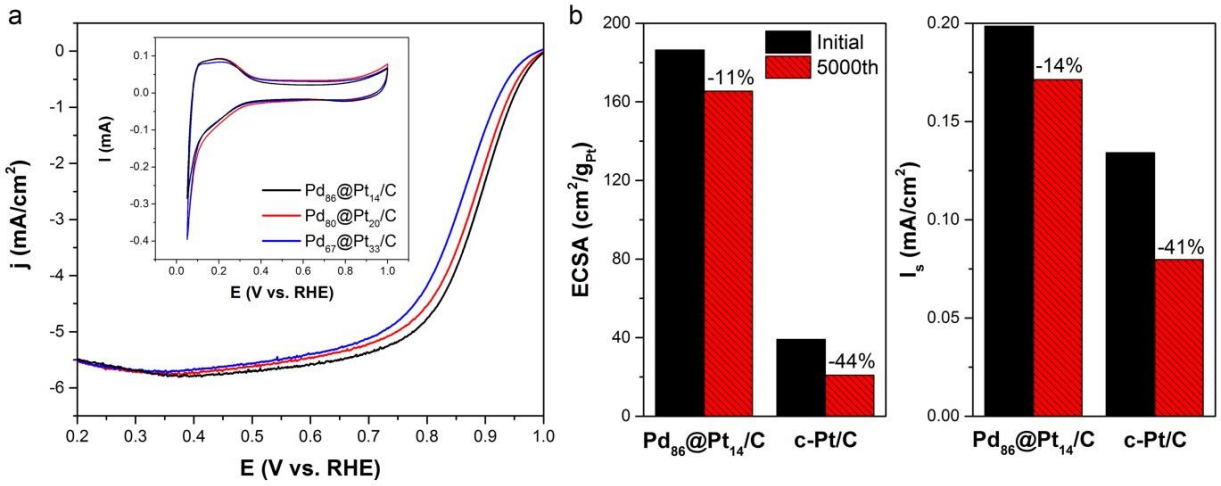

Figure 6.3 (a) ORR and the corresponding CV curves (inset) for the $Pd_x@Pt_y/C$ core-shell catalyst. (b) Comparison of electrochemical surface area and specific area activity for $Pd_{86}@Pt_{14}/C$ and commercial Pt/C catalysts at 0.9 V.

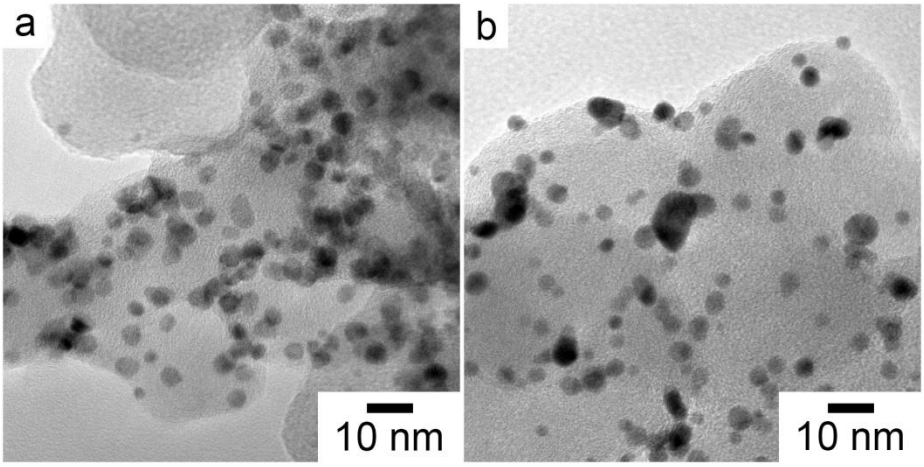

Figure 6.4 TEM micrographs of (a) $Pd_{86}@Pt_{14}/C$ and (b) commercial Pt/C after ADT.

6.4 Conclusion

A three-electrode system was adopted to conduct electrochemical measurements. Cubic Pt/C exhibited higher MOR activity and better tolerance to CO poisoning in comparison to its spherical counterpart, and characteristic peaks in the CV curve further confirmed its dominant (111) facet. Both cubic and octahedral Pt_3Ni/C catalysts had much more enhanced ORR activities than commercial Pt/C catalyst, with the octahedral one displaying more than 4 times the specific area activity at 0.9 V. $Pd_{86}@Pt_{14}$/C core-shell structure also displayed an impressive electrocatalytic performance in the ORR. The improved activity could be attributed to the strain effect induced by the underlying Pd core, while enhanced durability was due to the suppressed Oswald ripening and particle agglomeration.

6.5 References

1. Solla-Gullon, J.; Vidal-Iglesias, F. J.; Lopez-Cudero, A.; Garnier, E.; Feliu, J. M.; Aldaza, A. *Phys. Chem. Chem. Phys.* **2008**, *10*, 3689-3698.

2. Jin, M. S.; Zhang, H.; Xie, Z. X.; Xia, Y. N. *Energy Environ. Sci.* **2012**, *5*, 6352-6357.

3. Cheong, S. S.; Watt, J. D.; Tilley, R. D. *Nanoscale* **2010**, *2*, 2045-2053.

4. Wu, J.; Yang, H. *Acc. Chem. Res.* **2013**, *46*, 1848-1857.

5. Alayoglu, S.; Nilekar, A. U.; Mavrikakis, M.; Eichhorn, B. *Nat. Mater.* **2008**, *7*, 333-338.

6. Wang, Y. J.; Zhao, N. N.; Fang, B. Z.; Li, H.; Bi, X. T. T.; Wang, H. J. *Chem. Rev.* **2015**, *115*, 3433-3467.

7. Seh, Z. W.; Kibsgaard, J.; Dickens, C. F.; Chorkendorff, I. B.; Norskov, J. K.; Jaramillo, T. F. *Science* **2017**, *355*, 146-159.

8. Mazumder, V.; Sun, S. H. *J. Am. Chem. Soc.* **2009**, *131*, 4588-4590.

9. Stamenkovic, V. R.; Fowler, B.; Mun, B. S.; Wang, G. F.; Ross, P. N.; Lucas, C. A.; Markovic, N. M. *Science* **2007**, *315*, 493-497.

10. Chen, Y. X.; Miki, A.; Ye, S.; Sakai, H.; Osawa, M. *J. Am. Chem. Soc.* **2003**, *125*, 3680-3681.

11. Xia, X. H.; Iwasita, T.; Ge, F.; Vielstich, W. *Electrochim. Acta.* **1996**, *41*, 711-718.

12. Zhou, W.; Wu, J.; Yang, H. *Nano Lett.* **2013**, *13*, 2870-2874.

13. Zhao, R. P.; Liu, Y.; Liu, C.; Xu, G. R.; Chen, Y.; Tang, Y. W.; Lu, T. H. *J. Mater. Chem. A* **2014**, *2*, 20855-20860.

14. Choi, R.; Choi, S. I.; Choi, C. H.; Nam, K. M.; Woo, S. I.; Park, J. T.; Han, S. W. *Chem.-Eur. J.* **2013**, *19*, 8190-8198.

15. Wang, X.; Choi, S. I.; Roling, L. T.; Luo, M.; Ma, C.; Zhang, L.; Chi, M. F.; Liu, J. Y.; Xie, Z. X.; Herron, J. A.; Mavrikakis, M.; Xia, Y. N. *Nat. Commun.* **2015**, *6*.

16. Wang, X.; Vara, M.; Luo, M.; Huang, H. W.; Ruditskiy, A.; Park, J.; Bao, S. X.; Liu, J. Y.; Howe, J.; Chi, M. F.; Xie, Z. X.; Xia, Y. N. *J. Am. Chem. Soc.* **2015**, *137*, 15036-15042.

17. Xia, B. Y.; Ng, W. T.; Wu, H. B.; Wang, X.; Lou, X. W. *Angew. Chem.-Int. Edit.* **2012**, *51*, 7213-7216.

18. Sun, S. H.; Zhang, G. X.; Geng, D. S.; Chen, Y. G.; Li, R. Y.; Cai, M.; Sun, X. L. *Angew. Chem.-Int. Edit.* **2011**, *50*, 422-426.

Chapter 7:

Conclusion and Future Work

7.1 Thermal Treatment

Although ligands are important in the nanoparticle synthesis to achieve high shape uniformity, they are often detrimental for catalysis as they block the access of reactant molecules to the surface atoms. Therefore, the catalysts so-generated need to undergo a surfactant removal process before being used as catalysts. Currently we adopt an acetic acid washing treatment to remove these ligands; however, this process cannot be incorporated into the conveyor transport system easily. A more practical approach is thermal annealing. By heating the as-made catalysts under air at 185 °C for 5 h or 700 °C for 30 s, the surfactant can be removed completely without changing the size and shape of the supported nanocrystals.[1-2] Most importantly, this process can be easily combined with a conveyor transport system by adding another tubular reactor.

Thermal annealing can also be applied to transform Pt-based bimetallic alloy catalysts into nanostructures with intermetallic core and a Pt shell under H_2 or H_2/Ar environments.[3-4] Therefore, by introducing two more tubular reactors to the existing process, one focusing on surfactant removal and the other on phase transformation, we are able to continuously generate surfactant-free, highly active and stable catalysts in a single step.

7.2 MEA Manufacturing

In a fuel cell, membrane electrode assembly (MEA) is where the actual chemical reactions occur and its fabrication directly influences the overall cost of the system and its performance. There are three major types of MEA: catalyst coated membranes (CCM), catalyst coated substrate (CCS) and decal transfer method (DTM).[5] The basic concept of DTM is that the electrode layer is first cast on a temporary substrate such as Teflon, which is then hot pressed on to a membrane. The Teflon is peeled off afterward to form a MEA. Recently, a roll-press machine rather than a commonly used flat one has also been adopted to transfer the catalyst layer from the substrate onto the membrane.[6-7] This appears to be a processing unit that can be incorporated into the conveyor transport system since we already use Teflon-coated fiberglass fabric as the conveyor belt material, which serves as a perfect starting point for DTM-type MEA manufacturing (**Figure 7.1**). Though more work needs to be done, we believe the conveyor transport system can be a huge leap towards mass manufacturing.

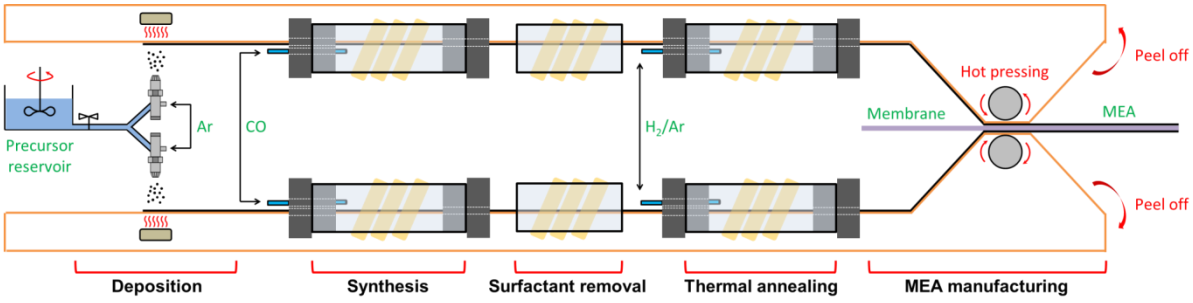

Figure 7.1 Schematic illustration of MEA manufacturing using conveyor transport system.

7.3 References

1. Li, D. G.; Wang, C.; Tripkovic, D.; Sun, S. H.; Markovic, N. M.; Stamenkovic, V. R. *ACS Catal.* **2012**, *2*, 1358-1362.

2. Cargnello, M.; Chen, C.; Diroll, B. T.; Doan-Nguyen, V. V. T.; Gorte, R. J.; Murray, C. B. *J. Am. Chem. Soc.* **2015**, *137*, 6906-6911.

3. Wang, D. L.; Xin, H. L. L.; Hovden, R.; Wang, H. S.; Yu, Y. C.; Muller, D. A.; DiSalvo, F. J.; Abruna, H. D. *Nat. Mater.* **2013**, *12*, 81-87.

4. Chung, Y. H.; Chung, D. Y.; Jung, N.; Park, H. Y.; Yoo, S. J.; Jang, J. H.; Sung, Y. E. *J. Phys. Chem. C* **2014**, *118*, 9939-9945.

5. Chun, Y. G.; Kim, C. S.; Peck, D. H.; Shin, D. R. *J. Power Sources* **1998**, *71*, 174-178.

6. Mehmood, A.; Ha, H. Y. *Int. J. Hydrog. Energy* **2013**, *38*, 12427-12437.

7. Mehmood, A.; Ha, H. Y. *Int. J. Hydrog. Energy* **2012**, *37*, 18463-18470.

Appendix:

Measurement of Particle Size

The definition of the particle size in this dissertation varies based on the geometry of the particle. For both cubic and octahedral shape, the particle size is defined as the 'average edge length'. Take Pt_3Fe nanoparticles as examples (Figure A.1):

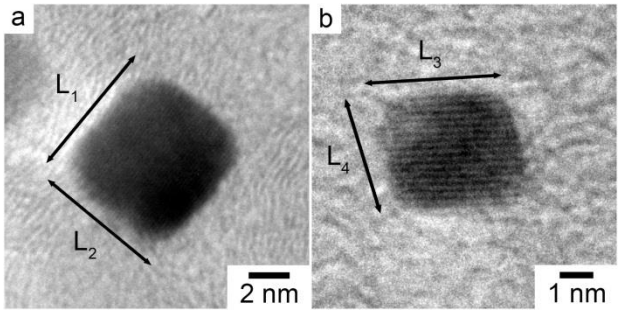

Figure A.1 HRTEM micrograph of (a) cubic and (b) octahedral Pt_3Fe nanoparticles.

$$\text{Particle size(Figure A. 1a)} = \frac{L_1 + L_2}{2} = \frac{6.57\ nm + 6.85\ nm}{2} = 6.71\ nm$$

$$\text{Particle size(Figure A. 1b)} = \frac{L_3 + L_4}{2} = \frac{4.12\ nm + 3.60\ nm}{2} = 3.86\ nm$$

For other geometry, the projected area observed on (HR)TEM micrograph is normalized to a circle first, and the particle size is defined as the 'diameter of the normalized circle' for comparison. Take a truncated octahedral Pd particle as an example (Figure A.2):

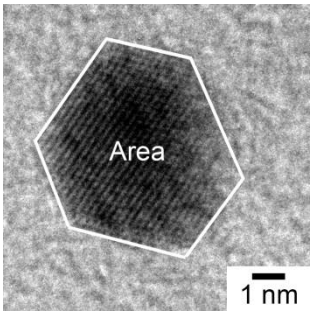

Figure A.2 HRTEM micrograph of truncated octahedral Pd nanoparticle.

$$\text{Particle size(Figure A. 2)} = \sqrt{\frac{4 \times Area}{\pi}} = \sqrt{\frac{4 \times 26.54\ nm^2}{\pi}} = 5.81\ nm$$

The area is calculated using ImageJ software.